ΕΘΝΙΚΟ ΜΕΤΣΟΒΙΟ ΠΟΛΥΤΕΧΝΕΙΟ
ΣΧΟΛΗ ΕΦΑΡΜΟΣΜΕΝΩΝ ΜΑΘΗΜΑΤΙΚΩΝ
ΚΑΙ ΦΥΣΙΚΩΝ ΕΠΙΣΤΗΜΩΝ

Μελέτη φαινομένων διαμήκους αστάθειας δέσμης σωματιδίων σε σύστημα δύο ραδιοσυχνοτήτων

ΔΙΔΑΚΤΟΡΙΚΗ ΔΙΑΤΡΙΒΗ

ΘΕΟΔΩΡΟΥ ΑΡΓΥΡΟΠΟΥΛΟΥ

Διπλωματούχου Φυσικού Εφαρμογών Ε.Μ.Π.

ΕΠΙΒΛΕΠΩΝ:
Ε. Γαζής
Καθηγητής Ε.Μ.Π.

Ιανουάριος 2015

ΕΘΝΙΚΟ ΜΕΤΣΟΒΙΟ ΠΟΛΥΤΕΧΝΕΙΟ
ΣΧΟΛΗ ΕΦΑΡΜΟΣΜΕΝΩΝ ΜΑΘΗΜΑΤΙΚΩΝ
ΚΑΙ ΦΥΣΙΚΩΝ ΕΠΙΣΤΗΜΩΝ

Μελέτη φαινομένων διαμήκους αστάθειας δέσμης σωματιδίων σε σύστημα δύο ραδιοσυχνοτήτων

ΔΙΔΑΚΤΟΡΙΚΗ ΔΙΑΤΡΙΒΗ

ΘΕΟΔΩΡΟΥ ΑΡΓΥΡΟΠΟΥΛΟΥ

Διπλωματούχου Φυσικού Εφαρμογών Ε.Μ.Π.

ΤΡΙΜΕΛΗΣ ΣΥΜΒΟΥΛΕΥΤΙΚΗ ΕΠΙΤΡΟΠΗ:

1. Ε. Γαζής, Καθ. Ε.Μ.Π.
2. Θ. Αλεξόπουλος, Καθ. Ε.Μ.Π.
3. Γ. Παπαφιλίππου, Ερευνητής CERN .

ΕΠΤΑΜΕΛΗΣ ΕΞΕΤΑΣΤΙΚΗ ΕΠΙΤΡΟΠΗ:

1. Ε. Γαζής, Καθ. Ε.Μ.Π.
2. Θ. Αλεξόπουλος, Καθ. Ε.Μ.Π.
3. Γ. Παπαφιλίππου, Ερευνητής CERN
4. Ε. Shaposhnikova, Ερευνητής CERN
5. Γ. Τσιπολίτης, Καθ. Ε.Μ.Π.
6. Δ. Φραντζεσκάκης, Καθ. Ε.Κ.Π.Α.
7. Κ. Χιτζανίδης, Καθ. Ε.Μ.Π.

Ιανουάριος 2015

To Fanouria, Panagiotis and Eirini

Στους πολυαγαπημένους μου Φανουρία, Παναγιώτη και Ειρήνη

Abstract

Operation with a double RF system is essential for many accelerators in order to increase beam stability, to change the bunch shape or to perform various RF manipulations. This is also the case for the operation of the CERN SPS as the LHC proton injector, where in addition to the main RF system, a fourth harmonic RF system is used in bunch shortening mode in order to increase the synchrotron frequency spread inside the bunch and thus to enhance Landau damping of the collective instabilities. In fact the double RF system operation in the SPS is one of the essential means, together with the controlled longitudinal emittance blow-up to significantly increase the longitudinal instability thresholds (single and multi-bunch) and deliver a good quality beam for the LHC. However, for the HiLumi-LHC (HL-LHC) and LHC injector upgrade (LIU) projects higher beam intensities are required. After all upgrades are in place, the main performance limitations of the LHC injector complex are beam instabilities and high intensity effects in the SPS. This thesis elaborates the benefits and the limitations of the operation in a double RF system. The study is primarily based on the beam and machine parameters of the SPS but most of the results can be generalized and used for other accelerators as well. In particular, the single-bunch longitudinal instability threshold is found from measurements, simulations and analytical calculations for the case of a purely reactive impedance and for the realistic case of the SPS impedance model. The effect of the relative phase and the voltage ratio between the two RF systems on beam stability is studied as well. Finally, the measured variation of the longitudinal emittance along the batch is explained by the modification of the synchrotron frequency distribution due to the residual effect of beam loading in the SPS double RF system.

Acknowledgments

This PhD wouldn't be possible without the help and contribution of many people.

Foremost, I would like to express my sincere gratitude to my CERN supervisor Dr. Elena Shaposhnikova for the continuous support, her patience, motivation, enthusiasm, and for sharing her immense knowledge. This thesis would not have been possible without her excellent guidance. Working under her supervision has been a valuable school. Her advice on research as well as on my career have been priceless. Thank you for encouraging my research and for allowing me to grow as a research scientist. You have been a tremendous mentor to me!

I would like to thank my university advisor Prof. Evangelos Gazis for giving me the great opportunity of being at CERN and his support whenever needed.

I am very grateful to Dr. Yannis Papaphilippou for showing me the path to the field of accelerator Physics, for his continues help and support, his guidance and his sincere interest for my personal and scientific progress.

I would also like to express my gratitude to Prof. Theodoros Alexopoulos, Prof. Dimitris Frantzeskakis, Prof. Kyriakos Hitzanidis and Prof. Yorgos Tsipolitis for accepting to be members of my examining committee.

I considered myself very lucky for having the opportunity to be part of the RF/BR section. In particular, I would like to thank Thomas Bohl for sharing his scientific knowledge and for his help during all the years of my thesis research. My office-mate and friend Juan Esteban Müller for all the discussions and thought exchange, for all his help and the very nice office atmosphere all these years. My colleague and friend Helga Timko for all the fruitful discussions and the constructive collaboration. I cannot forget the endless but enjoyable, hours (during day and night) I spent together with the three of them and Elena in the SPS faraday cage trying to measure and understand the longitudinal instabilities (not always easy especially very early in the morning!).

I couldn't neglect the important contribution of Heiko Damerau, Trevor Linecar, Joachim Tückmantel and Giulia Papotti. Each of them helped me build my knowledge in accelerators.

My colleagues from Fermilab Alexey Burov and Chandra Bhat. It was a great honor for me to work together with Alexey Burov and profit from his deep knowledge in physics and philosophy. Chandra was there in my first steps in accelerator physics giving me very helpful advices, especially for beam dynamics simulations.

It has been a pleasure to work together with my friends Hannes Bartosik and Benoit Salvant at the CCC and I would like to thank them for all the discussions and help whenever needed. They have always been reliable allies of the transverse plane. I would also like to thank Giovanni Rumolo for being a very helpful MD coordinator and of course all the SPS operators satisfying any needs we had.

All the hard work during my PhD wouldn't be as pleasant without the regular coffee breaks. For that I would like to thank all the people that passed through the years from the second floor of bld 864-C: Joachim, Elena, Thomas, Heiko, Fritz, Petri, Khris, Juan, Mathias, George, Michael, Michael, Silke, Luca, Helga, Jose, Maria, Mathiew, Alex, Danilo, Toon etc.

Nothing of this would be possible without the support of my family. My parents Sophia and

Panagiotis for their support during all these years and for being very helpful traveling whenever needed to provide the precious grandparent help. My two brothers Yannis and Alexis for their silent love and support. My parents in law Eirini and Christos for their precious grandparent help and love.

All my university years in physics were spent together with a group of 5 people who played a very important role in my personal developement. Yorgos, Yannis, Asteris, Fanouria and Christiana were always next to me for all the good and bad moments, being a family far from home. Thank you for being true friends until today!

Even further away from home, in Geneva, I was lucky to meet three very good friends: Christos, Kostas and Eleni. Starting at the same time at CERN, we shared very exciting and special moments. Thank you guys for being next to me all these years, supporting me and my family!

Finally, I would like to express my gratitude to my precious family, Fanourouki, Panagiotakos and Eirinoula for giving purpose to my life. Thank you very much for reminding me what is really important in life!

Contents

Περίληψη

Οι επιταχυντές σωματιδίων χρησιμοποιούνται ευρέως στις μέρες μας σε διάφορους επιστημονικούς τομείς, τόσο σε βασική όσο και σε εφαρμοσμένη έρευνα καθώς επίσης και σε πολλά τεχνικά και βιομηχανικά πεδία. Παρότι αρχικά προτάθηκαν στους τομείς της πυρηνικής φυσικής και της φυσικής υψηλών ενεργειών, είναι πλέον πολύ σημαντικοί σε βιομηχανικές εφαρμογές, στην επιστήμη των υλικών, στη βιολογία, στην ιατρική και στην ακτινοθεραπεία. Τα τελευταία 80 χρόνια η τεχνολογική ανάπτυξη οδήγησε σε μια αξιοσημείωτη αύξηση στην ενέργεια και στην ένταση των δεσμών σωματιδίων, που είχε σαν αποτέλεσμα σημαντικά επιτεύγματα σε όλους τους τομείς. Ωστόσο, η συνεχής αύξηση της έντασης και φωτεινότητας των δεσμών, έχει ως αποτέλεσμα την δημιουργία ισχυρών ιδιοπεδίων (ηλεκτρομαγνητικών πεδίων που δημιουργούνται από την ίδια τη δέσμη) τα οποία δρουν πίσω στη δέσμη και οδηγούν σε αστάθεια και κατά συνέπεια σε απώλεια σωματιδίων.

Η παρούσα διατριβή πραγματεύεται τα όρια σταθερότητας της δέσμης για συγκεκριμένες παραμέτρους της δέσμης και συνθήκες της επιταχυντικής διάταξης, οι οποίες σχετίζονται κυρίως με τον επιταχυντή πρωτονίων SPS του $CERN$. Η ανάλυση περιορίζεται στην διαμήκη κίνηση των σωματιδίων, υποθέτοντας ότι είναι εντελώς αποσυνδεδεμένη από την εγκάρσια. Στην πραγματικότητα, αυτή η υπόθεση ισχύει για όλες τις εξεταζόμενες περιπτώσεις.

Στην πλειονότητα των κυκλικών επιταχυντών, η επιτάχυνση των σωματιδίων σε υψηλές ενέργειες πραγματοποιείται με την εφαρμογή ενός διαμήκους εναλλασσόμενου (ημιτονοειδούς) ηλεκτρικού πεδίου σε μια ραδιοσυχνότητα η οποία, ανάλογα με το συγκεκριμένο μηχάνημα και το είδος των σωματιδίων, κυμαίνεται από μερικές εκατοντάδες kHz έως 10-30 GHz. Στην περίπτωση των σύγχροτρων , οι συχνότητες αυτές πρέπει να συγχρονιστούν με τη συχνότητα περιστροφής των σωματιδίων έτσι ώστε $f_{RF} = hf_0$, όπου h είναι ένας ακέραιος αριθμός που ονομάζεται αρμονικός αριθμός. Το ηλεκτρικό αυτό πεδίο αναγκάζει τα σωματίδια να εκτελούν ταλαντώσεις γύρω από μια σταθερή φάση ϕ_s, με συχνότητες γνωστές ως συχνότητες σύγχροτρον. Λόγω της περιοδικότητας του πεδίου RF υπάρχουν h περιοχές ευστάθειας κατά μήκος του επιταχυντή ($buckets$). Για το λόγο αυτό τα σωματίδια συνήθως ομαδοποιούνται σε πακέτα ($bunches$).

Εκτός από τα εξωτερικά ηλεκτρομαγνητικά πεδία που εφαρμόζονται στα φορτισμένα σωματίδια της δέσμης, τα οποία τα επιταχύνουν και τα εστιάζουν, υπάρχουν επίσης πεδία που παράγονται από την ίδια τη δέσμη, είτε άμεσα (δυνάμεις χωρικού φορτίου, ενδοδεσμικές σκεδάσεις σωματιδίων) ή με την αλληλεπίδραση με τα περιβάλλοντα υλικά, λόγω της πολυπλοκότητας και της ποικιλομορφίας (σε σχήμα και υλικά) των διαφόρων στοιχείων της μηχανής (σωλήνες δέσμη, φλάντζες σύνδεσης, κοιλότητες επιτάχυνσης RF, όργανα μέτρησης, μαγνήτες κλπ), τα οποία δημιουργούν μια αναπόφευκτη ανομοιομορφία στο περιβάλλον της δέσμης. Όταν ένα φορτισμένο σωματίδιο περνά μέσω οποιασδήποτε διατομής με ασυνέχεια, διεγείρει ένα ηλεκτρομαγνητικό πεδίο γνωστό ως επαγόμενο πεδίο ή πεδίο αφύπνισης ($wakefield$), δεδομένου ότι παραμένει συνήθως πίσω από το (υπερ-σχετικιστικό) σωματίδιο που προκάλεσε τη διαταραχή. Αυτό το επαγόμενο πεδίο θα δράσει πίσω στη δέσμη, διαταράσσοντας την κίνηση των σωματιδίων που θα ακολουθήσουν. Ολοκληρώνοντας σε μια πεπερασμένη κατανομή φορτισμένων σωματιδίων παίρνουμε το επαγόμενο δυναμικό ($wake\ potential$), το οποίο καθορίζεται από τη συνέλιξη της συνάρτησης αφύπνισης με την κατανομή φορτίου σε ένα πακέτο ($bunch$) σωματιδίων. Είναι σύνηθες στη φυσική επιταχυντών να χρησιμοποιείται ο χώρος των συχνοτήτων, όπου οι αναλυτικοί υπολογισμοί είναι πιο εύκολοι. Σε αυτήν

την περίπτωση, χρησιμοποιείται η έννοια της εμπέδησης σύζευξης ($beam-coupling\ impedance$) η οποία ορίζεται ως ο μετασχηματισμός $Fourier$ της συναρτήσεως αφύπνισης [1].

Γενικά, τα πεδία που επάγονται από τη δέσμη περιέχουν τρεις χωρικές συνιστώσες, που ταξινομούνται ως διαμήκης, οριζόντια και κάθετη (οι δύο τελευταίες αποτελούν το εγκάρσιο επίπεδο). Η διαμήκης συνιστώσα του ηλεκτρικού πεδίου, στο οποίο θα επικεντρωθούμε σε αυτή την εργασία, μπορεί να αλλάξει το πλάτος και τη φάση του εφαρμοζόμενου πεδίου επιτάχυνσης καθώς και την κατανομή ενέργειας και το μήκος του πακέτου σωματιδίων. Επιπλέον, η δράση της μπορεί να διαχωρίζεται σε ένα ή πολλά πακέτα, ανάλογα με τα χαρακτηριστικά της αντίστοιχης δύναμης. Επίδραση σε ένα μόνο πακέτο έχουμε όταν τα πεδία αφύπνισης είναι ισχυρά μόνο εντός των ορίων του μεγέθους ενός πακέτου σωματιδίων και φθίνουν πολύ γρήγορα ώστε να αφήνουν ανεπηρέαστα τα επόμενα πακέτα. Στην περίπτωση που τα πεδία παραμένουν αρκετά ισχυρά ώστε να επηρεάσουν τα επόμενα πακέτα σωματιδίων ή ακόμα και το ίδιο πακέτο στην επόμενη στροφή, τότε αναφερόμαστε στα φαινόμενα πολλών πακέτων ή φαινόμενα σύζευξης.

Τα πεδία αφύπνισης γίνονται ισχυρότερα σε υψηλότερα ρεύματα δέσμης. Μέχρι κάποια ένταση η δέσμη, παρότι διαταράσσεται, παραμένει σταθερή. Ωστόσο, πάνω από κάποιο κατώφλι ρεύματος, παρατηρείται διαμήκης αστάθεια της δέσμης, γνωστή ως συλλογική αστάθεια [2]. Ο τύπος της αστάθειας, η οποία περιορίζει την λειτουργία και την απόδοση του επιταχυντή, εξαρτάται σε μεγάλο βαθμό από τα χαρακτηριστικά του μηχανήματος (στοιχεία μηχανής, τύπος των σωματιδίων), καθώς και από τις παραμέτρους της δέσμης (μήκος, ένταση) [2–4]. Για παράδειγμα, η γρήγορη αύξηση του μήκους του πακέτου σωματιδίων που παρατηρήθηκε στο SPS στο παρελθόν [5], προκλήθηκε από μια μικρού μήκους κύματος (σε σύγκριση με το μήκος του πακέτου) αντίσταση συντονισμού η οποία διορθώθηκε μετά την θωράκιση των πηγών της αντίστασης αυτής [6]. Συγκεκριμένα, υπό την επίδραση του πεδίου αφύπνισης, ολόκληρη η δέσμη ή μέρος των σωματιδίων της δέσμης εκτελούν συγχρόνως ταλαντώσεις με συχνότητες (τρόπους ταλάντωσης) οι οποίες μπορούν να ταξινομηθούν σε διπολικές, τετραπολικές, εξαπολικές, κλπ [7]. Πάνω από κάποιο κατώφλι έντασης, παρατηρείται μια εκθετική αύξηση στο πλάτος της ταλάντωσης η οποία οδηγεί σε υποβάθμιση της ποιότητας της δέσμης και τελικά σε απώλειες σωματιδίων.

Ένας φυσικός μηχανισμός για την πρόληψη ή την απόσβεση της αστάθειες δέσμης προκύπτει από τη διαφορά των συχνοτήτων σύγχροτρον των σωματιδίων στο εσωτερικό του πακέτου. Συγκεκριμένα, αν η συχνότητα ενός τρόπου ταλάντωσης που διεγείρεται σε μια δέσμη, είναι εντός του εύρους των συχνοτήτων των σωματιδίων της δέσμης, τότε αυτός ο τρόπος θα αποσβέσει. Ο μηχανισμός αυτός είναι γνωστός ως απόσβεση $Landau$ και εισήχθη για πρώτη φορά στην φυσική πλάσματος [8]. Στο πλαίσιο των δεσμών φορτισμένων σωματιδίων, μια διεξοδική μελέτη του βασικού μηχανισμού έχει γίνει στο [9]. Για χαμηλές εντάσεις δέσμης, η διαφορά στις συχνότητες των σωματιδίων ορίζεται από το εξωτερικό RF πεδίο. Για ένα ημιτονοειδές εξωτερικό πεδίο RF το εύρος αυξάνεται με το μήκος της δέσμης (ανάλογο του $\phi_b^2/16$, όπου ϕ_b είναι το μισό του μήκους πακέτου σε ακτίνια) και ως εκ τούτου η απόσβεση $Landau$ είναι πιο αποδοτική.

Εκτός από την αύξηση του μεγέθους του πακέτου σωματιδίων, μια άλλη κοινή προσέγγιση για την ενίσχυση της απόσβεσης $Landau$ είναι να χρησιμοποιηθεί σύστημα ραδιοσυχνοτήτων σε κάποια ανώτερη αρμονική, σε συνδυασμό με το κυρίως σύστημα. Στην περίπτωση αυτή, η συνολική εξωτερική τάση που βλέπουν τα σωματίδια είναι:

$$V_{\text{ext}}(\phi) = V_1 \sin\phi + V_2 \sin(n\phi + \Phi_2), \tag{1}$$

όπου $V1$ και $V2$ τα πλάτη τάσης του κυρίως και του αρμονικού RF συστήματος, $n = h2/h1$ ο λόγος

των συχνοτήτων τους, Φ_2 η σχετική φάση και ϕ η συντεταγμένη φάσης των σωματιδίων στο κυρίως RF σύστημα. Για ένα μη επιταχυνόμενο πακέτο, το μέγιστο εύρος των συχνοτήτων σύνχροτρον του πακέτου επιτυγχάνεται όταν $\Phi_2 = 0, \pi$ [10] που αντιστοιχεί, στην περίπτωση που βρισκόμαστε πάνω από την ενέργεια μετάβασης (στα πλαίσια της παρούσας εργασίας θεωρούμε $\phi_s = \pi$), στους τρόπου λειτουργίας αύξησης -μήκους (BL: Bunch-Lengthening) και μείωσης -μήκους (BS: Bunch-Shortening) του πακέτου σωματιδίων, αντίστοιχα.

Σε πολλούς επιταχυντές χρησιμοποιείται ένα RF σύστημα υψηλής αρμονικής [11] σε συνδυασμό με το κυρίως σύστημα για διάφορους λόγους:

- Για να αυξήσει το εύρος των συχνοτήτων σύνχροτρον
- Για να αλλάξει το σχήμα του πακέτου σωματιδίων: επίπεδα πακέτα με μειωμένο πλάτος έντασης ρεύματος
- Για την αύξηση της περιοχής ευστάθειας στο διαμήκη χώρο φάσεων
- Για RF χειρισμούς (διαχωρισμός του πακέτου σωματιδίων, ελεγχόμενη αύξηση της διαμήκους εκπεμπτικότητας).

Οι πρώτες 2 περιπτώσεις στοχεύουν κυρίως στην αύξηση των ορίων ευστάθειας της δέσμης. Στην πρώτη περίπτωση, το υψηλής αρμονικής RF σύστημα καλείται συχνά ως κοιλότητα $Landau$, δηλώνοντας την αναμενόμενη αύξηση της σταθερότητας της δέσμης μέσω $Landau$ απόσβεσης. Το λεγόμενο παθητικό συστήματα RF υψηλής αρμονικής σε δακτυλίους αποθήκευσης ηλεκτρονίων χρησιμοποιεί την τάση που παράγεται από την ίδια τη δέσμη. Μεταξύ των τρόπων λειτουργίας ενός διπλού RF συστήματος, χρησιμοποιείται πολύ πιο συχνά ο τρόπος αύξησης μήκους (BLM), δεδομένου ότι είναι πιο ελκυστική για πολλούς λόγους. Για την ίδια τάση και αρμονικές αναλογίες δίνει μεγαλύτερο εύρος συχνοτήτων σύνχροτρον. Επιπλέον, παρέχει μεγαλύτερη περιοχή ευστάθειας, καθώς και μείωση στο πλάτος έντασης του ρεύματος σωματιδίων, μειώνοντας τα φαινόμενα χωρικού φορτίου. Ωστόσο, όπως δείχνει αυτή η διατριβή, η BLM μέθοδος έχει του δικούς της περιορισμούς. Για παράδειγμα, στην περίπτωση του SPS, η λειτουργία του μηχανήματος με αυτή τη μέθοδο δεν είναι δυνατή.

Το σύστημα δυο ραδιοσυχνοτήτων στο SPS είναι ένα από τα βασικά μέσα, σε συνδυασμό με την ελεγχόμενη αύξηση της διαμήκους εκπεμπτικότητας, και τη νέα οπτική $Q20$, για την σημαντική αύξηση των ορίων σταθερότητας (ενός και πολλών πακέτων) της δέσμης και την παροχή δεσμών καλής ποιότητας στον LHC. Ωστόσο, για το μέλλον του LHC και τα σχέδια αναβάθμισης του, $HL-LHC$ και LIU, όπου απαιτούνται υψηλότερες εντάσεις δέσμης, οι κύριοι περιορισμοί στην απόδοση του LHC προέρχονται από φαινόμενα που προκαλούν ασταθείς δέσμες στον SPS. Με κίνητρο τα προβλήματα διαμήκους αστάθειας των δεσμών του SPS, ο στόχος της παρούσας διατριβής είναι η λεπτομερής μελέτη και ανάλυση της απόδοσης ενός συστήματος 2 ραδιοσυχνοτήτων. Κατά συνέπεια, τα αποτελέσματα εφαρμόζονται κυρίως στις παραμέτρους δέσμης και μηχανής του SPS κατά τη λειτουργία του ως σύστημα παροχής δεσμών στον LHC. Ωστόσο, τα αποτελέσματα μπορούν να γενικευθούν σε πολλούς κυκλικούς επιταχυντές πρωτονίων.

Τα κύρια επιτεύγματα αυτής της εργασίας είναι η εξήγηση, είτε με αναλυτικές μεθόδους ή με προσομοιώσεις, των ακόλουθων σημαντικών πειραματικών παρατηρήσεων, τα οποία περιορίζουν το παρόν και το μέλλον της λειτουργίας του SPS:

- Την εμφάνιση αστάθειας στη δέσμη σε χαμηλό ρεύμα σωματιδίων όταν το σύστημα δυο ραδιοσυχνοτήτων λειτουργεί στην κατάσταση BL.

- Την εμφάνιση αστάθειας στη δέσμη σε χαμηλό ρεύμα σωματιδίων όταν το σύστημα δυο ραδιοσυχνοτήτων λειτουργεί στην κατάσταση BS όταν η αναλογία υψηλής τάσης μεταξύ των δύο συστημάτων RF $V2/V1 \leq 1/4$ για το SPS).

- Την εξάρτηση του κατωφλίου έντασης ενός πακέτου από τη σχετική φάση Φ_2 μεταξύ των δύο συστημάτων RF.

- Τη μη-ομοιόμορφα ελεγχόμενη αύξηση της διαμήκους εκπεμπτικότητας σε σύστημα δυο RF, που οδηγεί σε διακυμάνσεις του μήκους των πακέτων της δέσμης.

Αρχικά η διαμήκης ευστάθεια ενός πακέτου σωματιδίων σε σχέση με την κατανομή συχνοτήτων σύγχροτρον στο εσωτερικό του πακέτου $\omega_s'(J)$, μελετήθηκε για ένα σύστημα 2 RF δεύτερης αρμονικής ($h2/h1 = 2$) για εμπέδηση που περιλαμβάνει μόνο φανταστικό μέρος. Στη μελέτη αυτή δεν λήφθηκε υπόψη η περίπτωση επιτάχυνσης. Συγκεκριμένα, το κατώφλι απώλειας της απόσβεσης $Landau$ βρέθηκε τόσο από προσομοιώσεις όσο και από αναλυτικούς υπολογισμούς λαμβάνοντας υπόψη τη διαταραχή του δυναμικού. Η ημι-αναλυτική προσέγγιση βασίστηκε στην εύρεση των διακριτών $Van\ Kampen$ συχνοτήτων (συλλογικοί τρόποι ταλάντωσης χωρίς απόσβεση $Landau$) λύνοντας αριθμητικά την γραμμικοποιημένη εξίσωση $Vlasov$ [12, 13]. Οι προσομοιώσεις πραγματοποιήθηκαν χρησιμοποιώντας αριθμητικό κώδικα γραμμένο σε $Matlab$ για τους σκοπούς της παρούσας μελέτης.

Και οι δύο προσεγγίσεις έδειξαν ότι για τη λειτουργία BL και για μια επαγωγική εμπέδηση υπάρχει μια κρίσιμη τιμή για τη διαμήκη εκπεμπτικότητα (ή δράση J), πάνω από την οποία το κατώφλι της απόσβεση $Landau$ μειώνεται ταχέως στο μηδέν, όπως φαίνεται στην Εικόνα 1. Αυτή η κρίσιμη τιμή αντιστοιχεί στην περιοχή όπου $\omega_s'(J) = 0$ (ϵ_l=0.6 eVs στην Εικόνα 1). Μια μετατόπιση φάσης μεταξύ των δύο RF συνιστωσών πάνω από 15^o μπορεί να βοηθήσει στην αύξηση του κατωφλίου. Σε αυτή την περίπτωση το σχήμα του πακέτου παύει να είναι επίπεδο. Αυτά τα αποτελέσματα είναι σε θέση να εξηγήσουν τις παρατηρήσεις κατά τη διάρκεια της λειτουργίας του SPS ως συγκρουστήρας $p\bar{p}$ [14, 15]

Για μια χωρητική εμπέδηση (ή χωρικό φορτίο) τα κατώφλια είτε αυξάνονται δραματικά ή δεν μπορούν να υπολογιστούν αναλυτικά. Αυτό είναι σε συμφωνία με τις θεωρητικές προβλέψεις στο [16], όπου αποδείχθηκε ότι για την εμπέδηση χωρικού φορτίου, πάνω από την ενέργεια μετάβασης, μια δέσμη σε στατική κατάσταση είναι πάντα σταθερή.

Η ανάλυση εφαρμόστηκε για διάφορους λόγους αρμονικών συχνοτήτων $h2/h1 = n$ μεταξύ των δύο συστημάτων RF, διατηρώντας την ίδια αναλογία τάσης $V1/V2 = n$. Έχει αποδειχθεί ότι παρότι μεγαλύτερη τιμή του ν παρέχει μεγαλύτερο φάσμα συχνοτήτων σύγχροτρον, η κρίσιμη περιοχή μετατοπίζεται πιο κοντά στο κέντρο του πακέτου, και αυτό περιορίζει το μέγεθος του πακέτου που μπορεί να χρησιμοποιηθεί για σταθερή λειτουργία του επιταχυντή. Αποδείχθηκε επίσης ότι, κατά τη λειτουργία BS με $n \leq 3$, οι περιοχές όπου $\omega_s'(J) = 0$ εμφανίζονται ως τοπικά ακρότατα. Κατά συνέπεια, για τιμές εκπεμπτικότητας μεγαλύτερες από αυτές τις τιμές, το κατώφλι απώλειας της $Landau$ απόσβεσης είναι σημαντικά μειωμένο όπως φαίνεται στην Εικόνα 2 για $n = 4$ (0.3 eVs<ϵ_l<0.6 eVs).

Τα αποτελέσματα αυτά συμφωνούν πολύ καλά με τις πειραματικές παρατηρήσεις από τη λειτουργία του SPS με σύστημα 2 RF 4ης αρμονικής ($h = 4$). Πραγματοποιήθηκαν μετρήσεις του κατωφλίου της διαμήκους αστάθειας ενός πακέτου σε σχέση με τη σχετική φάση μεταξύ των δύο συστημάτων ραδιοσυχνοτήτων. Χρησιμοποιήθηκε λόγος των τάσεων $V2/V1 = 1/4$ και μια σταθερή

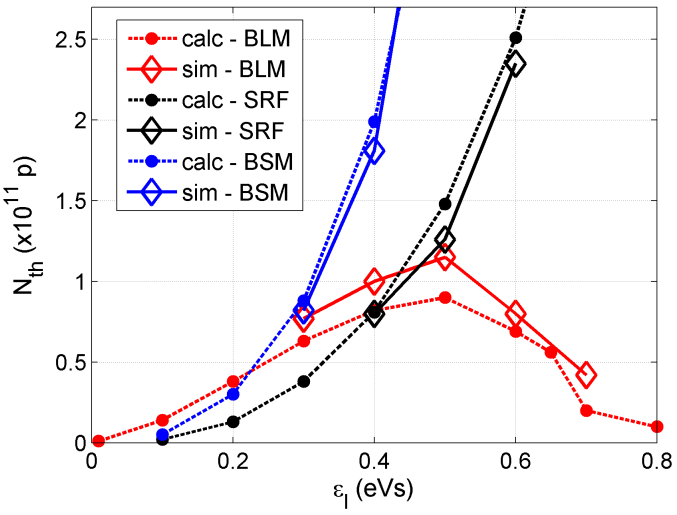

Figure 1: Κατώφλι απώλειας απόσβεσης *Landau* συναρτήσει της διαμήκους εκπεμπτικότητας σε σύστημα δυο RF (BLM - κόκκινο, BSM - μπλε) και σε σύστημα μιας RF (μαύρο) με βάση αναλυτικούς υπολογισμούς (τελείες) και προσομοιώσεις (ρόμβοι).

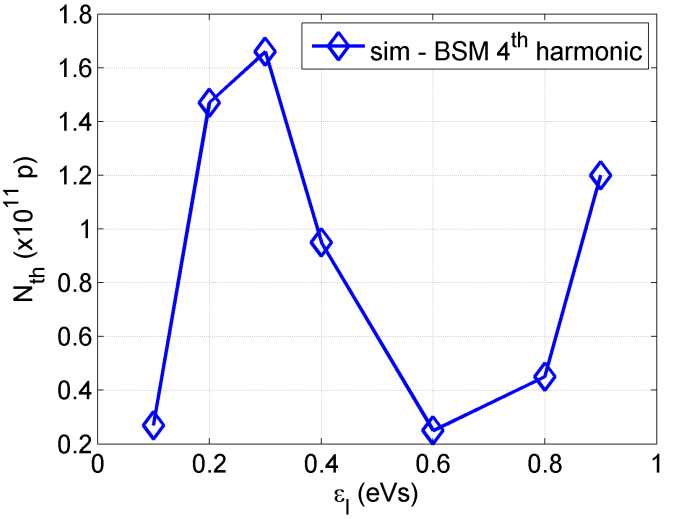

Figure 2: Κατώφλια απώλειας απόσβεσης *Landau* συναρτήσει της διαμήκους εκπεμπτικότητας για $h_2/h_1 = 4$ σε BSM τρόπο λειτουργείας, με βάση προσομοιώσεις.

ένταση δέσμης ανά πακέτο $1.0\ 10^{11}$. Η ανάλυση των μετρήσεων έδειξε ότι η δέσμη είναι ασταθής στη διαμήκη συνιστώσα τόσο στον BS όσο και στον BL τρόπο λειτουργίας. Οι φάσεις αυτές ορίζονται στο μηχάνημα με μία μέθοδο βαθμονόμησης βασισμένη στην ίδια τη δέσμη και η οποία πραγματοποιείται στην αρχή κάθε σειράς μετρήσεων. Σαρώνοντας τη μετατόπιση φάσεως μεταξύ των δύο συστημάτων RF, προσδιορίστηκε μια περιοχή ευστάθειας της δέσμης, μεταξύ 50^o και 100^o (στα 800 MHz) σε σχέση με την λειτουργία BS, όπως φαίνεται στην Εικόνα 3. Πραγματοποιήθηκαν

επίσης προσομοιώσεις χρησιμοποιώντας τον κώδικα $ESME$ [17] και το παρόν μοντέλο εμπέδησης του SPS, με σκοπό την επιβεβαίωση των αποτελεσμάτων.

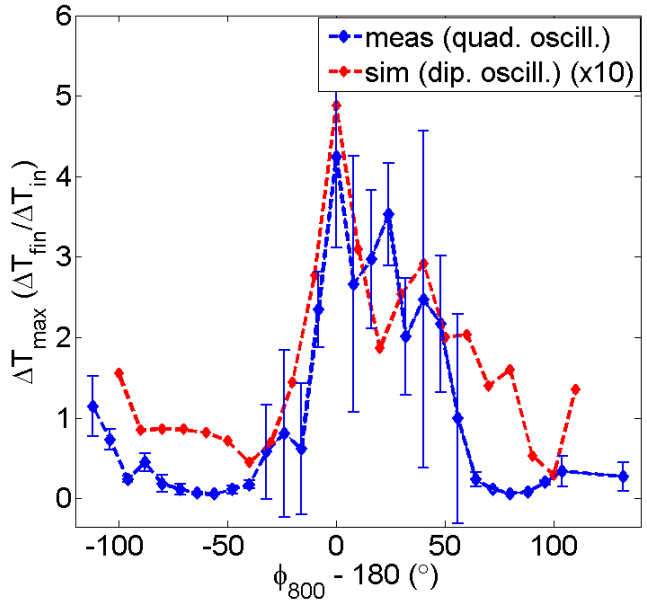

Figure 3: Λόγος τελικών προς αρχικών τετραπολικών (μετρήσεις) και διπολικών (προσομοιώσεις)Ρατιο οφ φιναλ το ινιτιαλ χυαδρυπολε (μεασυρεμεντς) ανδ πλατών ταλάντωσης, πολλαπλασιασμένοι με τη μέγιστη τιμή του (ΔT_{max}) συναρτήσει της ϕ_{800} στο σύστημα 2 RF του SPS με $V_r = 0.25$. Αριθμός προτονίων ανα πακέτο $\sim 1 \times 10^{11}$ με $\epsilon_l \simeq 0.25\ eVs$.

Τα αποτελέσματα των προσομοιώσεων έδειξαν πολύ καλή συμφωνία με τις μετρήσεις καθώς κατέληξαν στην ίδια περιοχή φάσεων. Μειώνοντας το λόγο των τάσεων σε $V2/V1 = 1/10$ (η τιμή που χρησιμοποιείται σήμερα σε λειτουργία) οδήγησε σε σταθεροποίηση της δέσμης σε BS τρόπο λειτουργίας, αποτέλεσμα το οποίο επίσης επιβεβαιώθηκε από τις προσομοιώσεις.

Η εξάρτηση από την φάση μεταξύ των δύο συστημάτων RF, εκτός από την ευαισθησία στο λόγο των τάσεων, δείχνει επίσης ότι η απώλεια της $Landau$ απόσβεσης στην επίπεδη περιοχή της κατανομής φάσεων σύγχροτρον μέσα στη δέσμη, μπορεί να είναι μια πιθανή εξήγηση για την απόσβεση των ταλαντώσεων που παρατηρούνται στις μετρήσεις. Για παράδειγμα, στη λειτουργία BS με $V2/V1 = 1/4$, το μέγεθος των πακέτων που χρησιμοποιούνται στις μετρήσεις (και τις προσομοιώσεις) είναι τέτοιο ώστε πολλά σωματίδια να είναι στην περιοχή όπου $\omega_s'(J) = 0$ όπου η $Landau$ απόσβεση χάνεται. Με τη μείωση της αναλογίας σε $V2/V1 = 1/10$ η κατανομή συχνοτήτων σύγχροτρον γίνεται μονότονη για τη λειτουργία σε BS και ως εκ τούτου επιτυγχάνεται ευστάθεια της δέσμης, όπως φαίνεται στην Εικόνα 4. Το γεγονός αυτό δίνει τόσο την αιτιολόγηση αλλά και τον περιορισμό στην τάση των 800 MHz που χρησιμοποιήθηκε για τις LHC δέσμες στον SPS.

Ακόμη και με το σύστημα 2 ραδιοσυχνοτήτων τέταρτης αρμονικής σε λειτουργία BS με αναλογία τάσης $V2/V1 = 1/10$, οι δέσμες πρωτονίων τύπου LHC στον SPS εξακολουθούν να είναι ασταθείς στο τέλος της επιτάχυνσης. Για το λόγο αυτό εφαρμόζεται μια ελεγχόμενη αύξηση της διαμήκους εκπεμπτικότητας, κατά το δεύτερο μέρος της επιτάχυνσης, με σκοπό την περαιτέρω αύξηση του

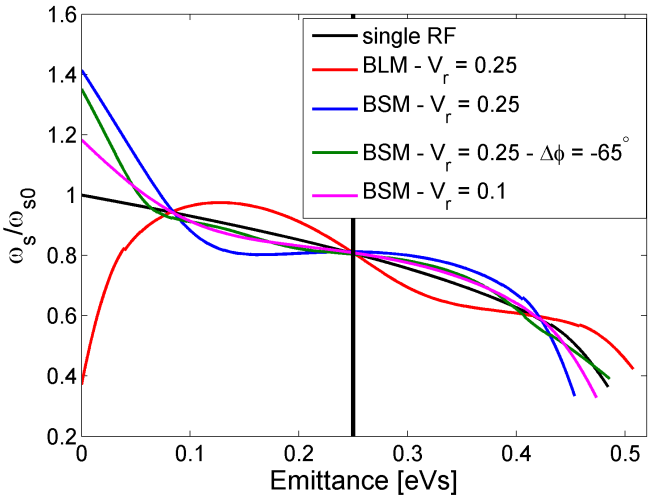

Figure 4: Κατανομή συχνοτήτων σύγχροτρον συναρτήσει της διαμήκους εκπεμπτικότητας για διαφορετικές παραμέτρους της RF. Η μαύρη οριζόνται γραμμή παρουσιάζει το μέγεθος του πακέτου με βάση τις μετρήσεις.

φάσματος των συχνοτήτων σύγχροτρον μέσα στο πακέτο σωματιδίων, ενισχύοντας το φαινόμενο της $Landau$ απόσβεσης. Αυτό επιτυγχάνεται με την εισαγωγή θορύβου στο σύστημα RF των 200 MHz. Ωστόσο, η μέθοδος αυτή έχει τους δικούς της περιορισμούς. Πράγματι, οι πειραματικές μετρήσεις έδειξαν ότι μετά την εισαγωγή του θορύβου, η κατανομή των μηκών των πακέτων έχει μια μη-ομοιόμορφη δομή, όπως φαίνεται στην Εικόνα 5. Το φαινόμενο αυτό γίνεται εντονότερο με την αύξηση του πλάτους του θορύβου και αποτελεί έναν περιορισμό στην εισαγωγή της δέσμης στον LHC όταν για σκοπούς ευστάθειας σε υψηλότερες εντάσεις δέσμης ζητηθεί μεγαλύτερη εγκάρσια εκπεμπτικότητα.

Έχει αποδειχθεί κατά τη διάρκεια αυτής της εργασίας, ότι οι μετρούμενες μεταβολές της τελικής διαμήκους εκπεμπτικότητας κατά μήκος της δέσμης μπορούν να εξηγηθούν από την μεταβολή της κατανομής συχνοτήτων σύγχροτρον λόγω της επαγόμενης τάσης στις κοιλότητες ραδιοσυχνοτήτων ($beam\ loading$) στο σύστημα 2 RF στο SPS. Ειδικότερα, λαμβάνοντας υπόψη την εναπομένουσα επαγόμενη τάση στις κοιλότητες ραδιοσυχνοτήτων των 200 MHz (με τα συστήματα ανάδρασης ($feed-back$) και ανατροφοδοσίας ($feed-forward$)), και την επαγόμενη τάση στις κοιλότητες των 800 MHz, η παρατηρούμενη μεταβολή της θέσης των πακέτων κατά μήκος της δέσμης μπορεί να αναπαραχθεί με καλή ακρίβεια, όπως φαίνεται στην Εικόνα 6. Με βάση αυτό το μοντέλο υπολογίστηκε η κατανομή συχνοτήτων σύγχροτρον για πακέτα σε διαφορετικές θέσεις κατά μήκος της δέσμης η οποία μπορεί να εξηγήσει τη μεγάλη διακύμανση στην εκπεμπτικότητα των πακέτων για την εφαρμοζόμενη συνάρτηση θορύβου.

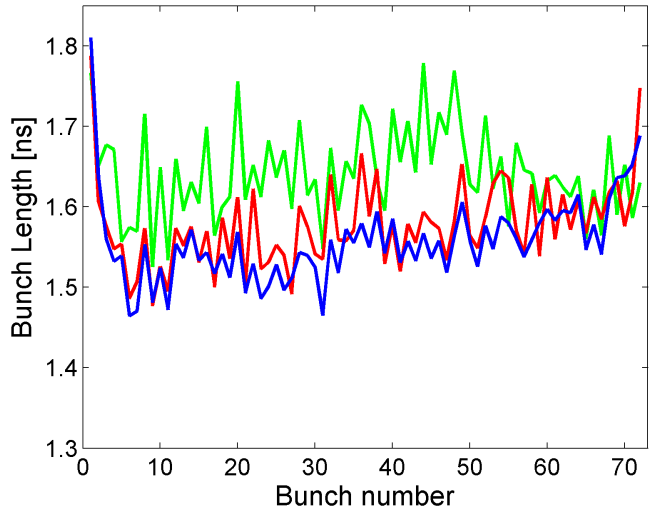

Figure 5: Μετρήσεις μήκους των πακέτων σωματιδίων πριν την ελεγχόμενη αύξηση της διαμήκους εκπεμπτικότητας (πράσινο), αμέσως μετά (κόκκινο) και στο τέλος της επιτάχυνσης (μπλέ).

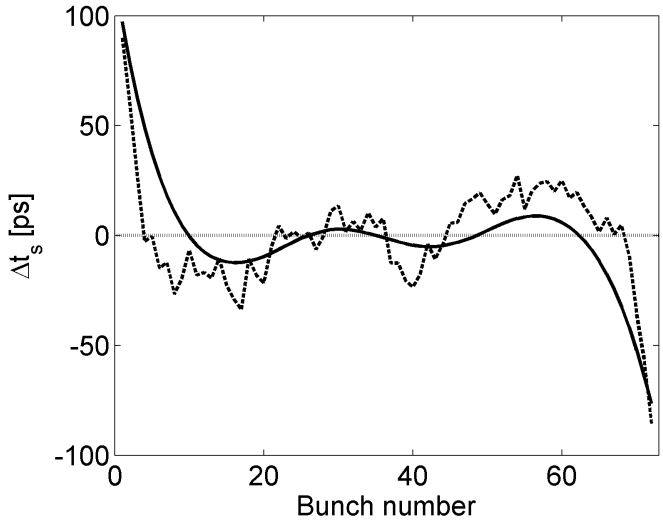

Figure 6: Μεταβολή της θέσης του πακέτου κατα μήκος της δέσμης, πριν την εφαρμογή της συνάρτησης θορύβου. $V_{200} = 4.5\ MV$ και $V_{800} = 0.5\ MV$.

Chapter 1

Introduction

Particle accelerators are widely used today in science, both in fundamental and applied research, but also in many technical and industrial fields. Although, initially proposed for nuclear and particle physics research, now accelerators are of great importance in industrial applications, in material science (synchrotron light sources and spallation neutron sources), in biological and medical research and in radiotherapy (cyclotrons). Over the last 80 years, technological progress allowed a remarkable increase in energy and intensity of the particle beams, leading to numerous achievements in all the previously mentioned fields. However, the constant demand for beams of higher current and luminosity[1] is limited also by the undesirable effects of the electromagnetic (EM) fields produced by the particles themselves. Those effects can degrade the beam quality and in some cases lead to beam instabilities and eventually to particle losses.

This thesis investigates the limits of beam stability for some specific beam parameters and machine conditions, mainly related to the CERN Super Proton Synchrotron (SPS) (see below). We will study these effects in the so-called *circular* accelerators, although their real shape is more complicated, e.g. they usually contain a number of straight sections. Particles in such accelerators perform a periodic motion around the circumference with revolution period T_0. In particular, this thesis is focused on the special type of circular machines called *synchrotrons*, where the external EM fields are synchronized with the particles' revolution frequency $f_0 = 1/T_0$, confining their orbit in a well-defined path. Furthermore, we will restrict the analysis to the longitudinal motion of the particles, assuming that it is completely decoupled from the transverse one. In fact, this assumption is valid for all the considered cases.

Today, in the majority of the circular accelerators, the acceleration of the particles to high energies is performed by the application of longitudinal alternating (sinusoidal) electric field at an RF frequency f_{rf} which, depending on the specific machine and the type of the particles, ranges from a few hundred kHz to 10-30 GHz. In the case of synchrotrons, these frequencies have to be synchronized with the particles' revolution frequency so that $f_{\mathrm{rf}} = hf_0$, where h is an integer called the *harmonic number*. Consequently, this focusing electric field forces the particles to perform (synchrotron) oscillations around a stable phase ϕ_s, with frequencies known as *synchrotron frequencies*. Due to the periodicity of the RF field there are h similar stable regions, called *RF buckets*. For this reason in synchrotrons the particles are usually grouped into bunches. In most of the cases several regularly spaced bunches are accelerated simultaneously, but in some cases there is only a single bunch circulating in the machine.

In addition to the external EM fields which are applied to the charged particles in the bunch, to accelerate and confine them transversely, there are fields which are generated by the beam itself, either directly (space charge forces, intra-beam scattering) or by the interaction with its surrounding (see for example [18]). This effect is imposed by the complexity and diversity

[1] The luminosity, $\mathcal{L}$ in $\mathrm{cm}^{-2}\mathrm{s}^{-1}$ is a measure of the rate the particles interact per unit area in a collision process.

(in shape and materials) of the various machine elements (beam pipes with expansion bellows, connection flanges, accelerating RF cavities, kickers, collimators, beam instrumentation, magnets etc), which create an unavoidable non-uniformity of the beam surrounding. When a charged particle passes through any cross-section discontinuity, it excites an EM field known as *wake field* (or *wake function*) since it remains usually behind the (ultra-relativistic) exciting particle. This wake field will react back on the beam, perturbing the motion of the trailing particles. The integrated effect over a finite distribution of charged particles is described by the *wake potential*, which can be determined by the convolution of the wake function with the charge distribution in the bunch. It is common in accelerator physics to use also frequency domain where analytic calculations are usually easier. In that case, one uses the concept of *beam-coupling impedance* which is defined as the *Fourier transform* of the wake function [1].

Generally, the beam induced fields contain three spatial components, classified as longitudinal, horizontal and vertical (the last two constitute the transverse plane). The longitudinal component of the electric field, on which we will be focusing in this thesis, may change the effective amplitude and phase of the applied accelerating RF field as well as the energy distribution in the bunch and its length. Furthermore, its effect can be separated into single-bunch and multi-bunch, depending on the characteristics of the respective force. Single-bunch effects are caused by wake fields that are strong only within the limits of the bunch size and are decaying fast enough, leaving the coming bunches unaffected. In contrast to that, multi-bunch or coupled bunch effects are caused by forces which remain strong enough to disturb the motion of the later bunches or even of the same bunch in the next revolution turn.

The wake field becomes stronger at higher beam currents. Up to some intensity the beam, although perturbed, remains stable. However, above some threshold current, longitudinal instability of the beam will occur, known as *collective instability* [2]. The type of the instability, which limits the operation of an accelerator depends strongly on the characteristics of the specific machine (machine elements, type of particles) as well as the bunch parameters (length, intensity) [2–4]. For instance, the fast increase of the bunch length observed in the SPS in the past [5] was caused by a short wavelength (compared to the bunch length) resonant impedance and disappeared after shielding of the responsible sources [6]. In particular, under the influence of the wake field, the whole bunch or part of the particles inside the bunch are performing coherent oscillations with frequencies (modes) which can be classified into dipole, quadrupole, sextupole, etc., depending on the shape of the oscillations [7]. Above some intensity threshold, an exponential growth of oscillation amplitude is observed leading to degradation of the beam quality and eventually to particle losses.

A natural mechanism to prevent or damp the beam instabilities arises from the difference of the individual particle frequencies inside the bunch (incoherent synchrotron frequencies). In particular, if the frequency of a coherent mode, excited in a bunch, is within the range of the incoherent frequencies of the particles, then this mode will be damped. This mechanism is known as *Landau damping* and was introduced first in plasma physics [8]. In the context of charged particle beams, a thorough exposition of the basic underlying mechanism has been provided in [9]. For low intensities, the spread in the particle frequencies is defined by the external RF field. For a sinusoidal external RF field the spread is increasing with the bunch length (proportional to $\phi_b^2/16$, where ϕ_b is half the bunch length in radians) and thus Landau damping is more effective.

Besides increasing the bunch size, another common approach to enhance Landau damping in an accelerator is to use a higher harmonic RF system in addition to the main one. In this case, the total external voltage seen by the particles is

$$V_{\text{ext}}(\phi) = V_1 \sin\phi + V_2 \sin(n\phi + \Phi_2), \tag{1.1}$$

where V_1 and V_2 are the voltage amplitudes of the main and high harmonic RF systems, $n = h_2/h_1$ is the ratio between their frequencies, Φ_2 is the relative phase and ϕ is the phase coordinate of the particles at the main RF system. For a non-accelerating bucket the maximum spread of the incoherent synchrotron frequencies inside the bunch is obtained when $\Phi_2 = 0, \pi$ [10], corresponding, above transition energy ($\phi_s = \pi$, the case considered in this thesis), to bunch-lengthening (BL) and bunch-shortening (BS) mode accordingly (see next Chapter).

In many accelerators a high harmonic RF system is installed [11] in addition to the main RF system for various applications:

- To increase the synchrotron frequency spread
- To change the bunch shape: flat bunches with reduced peak line density in BLM
- To increase the available stable area in the longitudinal phase space (bucket area)
- For RF manipulations (bunch splitting, bunch rotation, controlled emittance blow-up etc.), see for example [19].

The first two are mainly aimed at increasing beam stability. In the first case the high harmonic RF system is often called a *Landau cavity* to indicate an expected increase of beam stability through Landau damping. So-called *passive* high harmonic RF systems in electron storage rings use the voltage generated by the beam itself by correct choice of cavity de-tuning. Among the operating modes of a double RF system BLM is used much more often since it is more attractive for many reasons. For the same voltage and harmonic ratios it gives larger synchrotron frequency spread. In addition it provides larger bucket area as well as reduced peak line density and therefore reduced space charge effects and machine elements heating. However, as shown below BLM has its own limitations. For example, in the case of the SPS, operating the high harmonic RF system in BLM is not possible [10].

This thesis is dedicated to the study of the beam dynamics in a double RF system for proton beams. It is motivated by longitudinal stability issues in the CERN SPS [20] during its operation as the injector of the Large Hadron Collider (LHC) [21]. Thus, for most of the cases the obtained results are applied to the beam and machine parameters of the SPS (see below). However, most of them can be generalized to other proton accelerators as well.

1.1 The CERN accelerator complex

The name CERN is derived from the acronym for the French *Conseil Européen pour la Recherche Nucléaire*, or European Organization for Nuclear Research. Founded in 1954 in the Franco-Swiss border near Geneva, by a convention between twelve European countries, CERN is one of the world's largest and most advanced centers for scientific research [22].

During the past years, many significant scientific discoveries were made at CERN (neutral currents, W and Z bosons, first observation of anti-Hydrogen, etc.). Today, CERN is widely known to host the 27 km long *Large Hadron Collider* (LHC) [23]. The LHC is the largest circular accelerator in the world and the main focus of research at CERN. It it operating since 2009. In the LHC the particles are injected at 450 GeV and accelerated up to the energy of 4 TeV (an energy of 7 TeV is planned to be reached from 2015 onwards). At top energy the two, counter rotating, proton or ion beams are made to collide at the four interaction points, where detectors are placed to observe the debris of the collisions and examine any particles that may be produced (ATLAS, CMS, ALICE and LHCb). The biggest of these experiments, ATLAS and CMS, use general-purpose detectors to investigate the largest range of physics possible (as Standard Model, the Higgs mechanism, Super-symmetry and others). In fact, a particle consistent with a Standard Model Higgs boson was discovered in 2012 [24, 25]. Apart from these four, three other, smaller, experiments are installed in the LHC tunnel and many more experiments use beam from other CERN accelerators and facilities, being an important part of the laboratory's activities.

The energy of the particles injected into the LHC is gradually increased to 450 GeV in the LHC injector complex shown in Fig. 1.1. Once accelerated in a particular machine, particles are either transferred to a larger machine or supplied to one of the experiments mentioned before. Currently, two types of particles are accelerated in the LHC: protons (H^+), which are the nuclei of hydrogen atoms; and lead ions (Pb^{+82}).

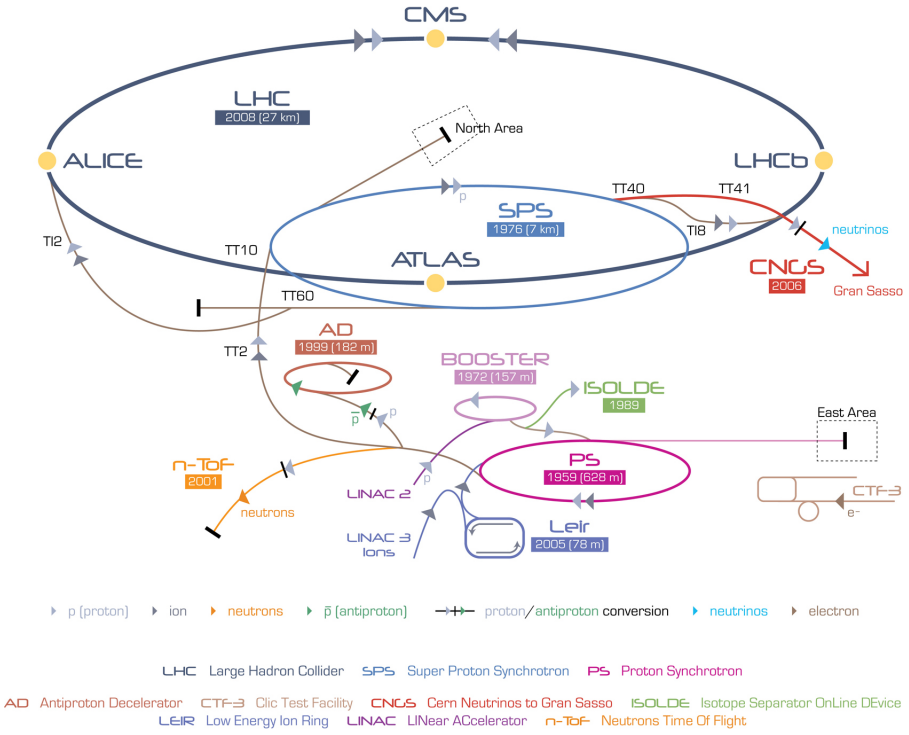

Figure 1.1: Schematic view of the present CERN accelerator complex. ©CERN.

For the protons going to the LHC, the injector chain starts with the linear accelerator LINAC2, accelerating them to 50 MeV. The beam is then accelerated to 1.4 GeV by a 157 m

length synchrotron, called the Proton Synchrotron Booster (PSB) (4 almost identical superimposed rings), before being passed into the Proton Synchrotron (PS). The PS is a 628 m length synchrotron, where the particles are accelerated up to the energy of 25 GeV. This is the machine where the longitudinal bunch structure of LHC-type proton beams is produced by multiple bunch splitting (and merging) using elaborate RF manipulations [26] (see below) which require a variety of RF systems with different harmonics (10 MHz, 20 MHz, 40 MHz, and 80 MHz RF systems). Longitudinal bunch rotation is performed just before extraction to ensure that the bunches have the correct length before injection into the SPS. In the SPS, protons are then accelerated up to 450 GeV and sent to the LHC.

Lead ions for the LHC start from a source of vaporized lead and enter LINAC3 before being collected and accelerated in the Low Energy Ion Ring (LEIR). They then follow the same route to their maximum energy as the protons.

1.2 LHC proton beam production

In the nominal mode of operation for filling the LHC, the PS delivers every 3.6 s a batch of 72 bunches spaced by 25 ns [21]. This distance between bunches is preserved up to the LHC. To prepare this beam two different splitting schemes are used in the PS [26]. Other bunch trains with larger bunch spacing and smaller number of bunches are also produced. In fact, during the previous years of the LHC operation, beam with 50 ns bunch spacing was used, with 36 bunches per PS batch.

The complete process of the production of the 25 ns bunch spacing LHC beam is schematically presented in Fig. 1.2. Six bunches delivered in two batches by the PSB are captured in the PS on harmonic $h = 7$. On the 1.4 GeV (kinetic energy) injection flat bottom, the 6 bunches are triple split. This process is started as soon as the second batch is received (1.2 s after the first injection), which provides 18 consecutive bunches on $h = 21$ (10 MHz RF system). The beam is then accelerated on this harmonic up to the 25 GeV flat top, where each bunch is twice split in two to give 72 consecutive bunches on $h = 84$ (40 MHz). The whole process consists of a complicated RF manipulation where many RF harmonics are required simultaneously ($h = 7, 14, 21$ for the triple splitting and $h = 21, 42, 84$ for the quadruple splitting). Careful design of the RF voltage and phase programs is necessary in order to obtain equal bunches with the same distribution of particle density as the initial one [21]. In addition, a beam phase loop is used to suppress collective oscillations with respect to the RF sum voltage. Moreover,in order to achieve nominal longitudinal emittance (see below) and ensure beam stability a controlled emittance blow-up is applied by using phase modulation of the 200 MHz RF system.

Similar procedure is followed during the production of the 50 ns bunch spacing LHC beam, but without the second splitting in two bunches at 25 GeV. Thus, a batch of 36 bunches are obtained, spaced by 50 ns.

At the end of the splitting process at 25 GeV, the bunches with a length of around 11 ns are held by the RF on $h = 84$ (40 MHz). Since in the SPS the frequency of the main RF system is 200 MHz (RF period of 5 ns) the PS bunches are too long for injection into the SPS. Thus, prior to the transfer to the SPS, the bunches are rotated in the longitudinal plane during a quarter of a synchrotron period by a fast (within a few revolutions) increase of the RF voltage on harmonics

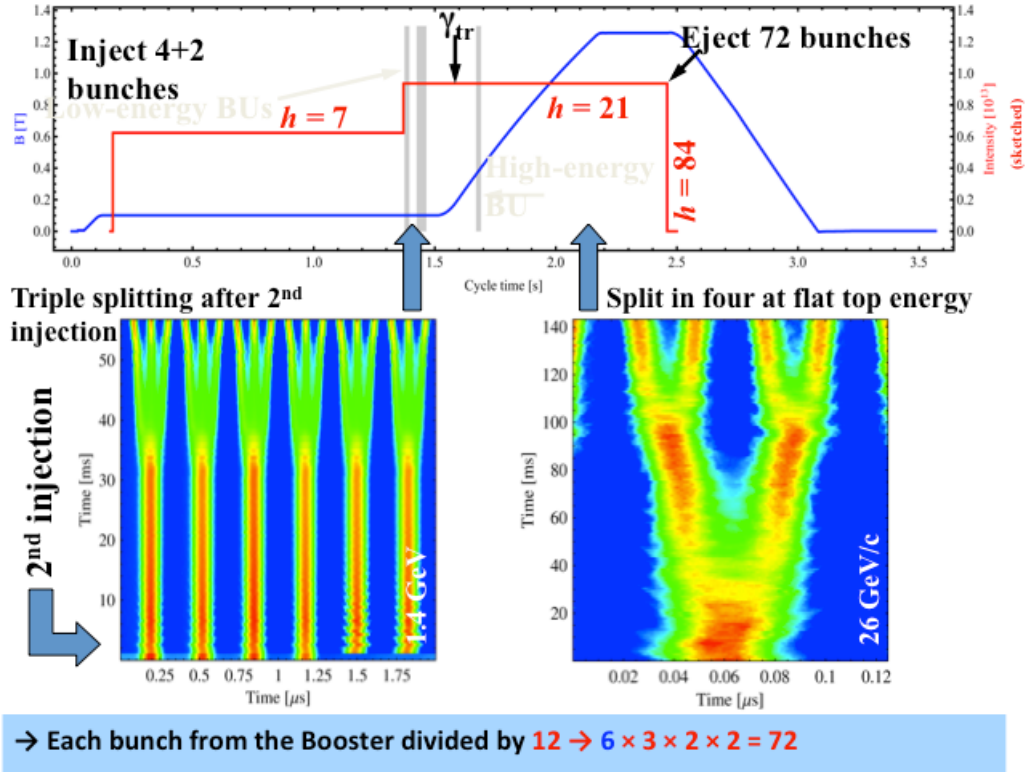

Figure 1.2: Schematic representation of the production of the LHC 25 ns beam in the CERN PS [27].

$h = 84$ and $h = 168$ (80 MHz) [21]. With this, non-adiabatic procedure the bunch length is reduced to about 4 ns. Up to four consecutive batches of 72 (or 36) bunches are injected every 3.6 s into the SPS at 26 GeV/c.

1.3 The Super Proton Synchrotron as the LHC injector

The SPS is the second largest accelerator in the CERN accelerator complex with a circumference of 6.9 km. It was fully commissioned in 1976 and since then, it has been used as a proton-antiproton collider (Sp$\bar{\text{p}}$S), served as the injector for the Large Electron-Positron collider (LEP) and now provides protons and ions to the LHC alongside fixed-target experiments including CNGS (until 2013), COMPASS and the North Area.

Proton beams for the LHC are injected at a momentum of 26 GeV/c from the PS and accelerated up to 450 GeV/c before extraction into the LHC. The usual LHC filling cycle in the SPS (see Fig. 1.3) is designed for up to four injections from the PS. Since the length of the PS cycle is 3.6 s, an injection plateau of 10.8 s is required in the SPS. After the injection of the last batch, a ramp to 450 GeV/c with an average ramp rate of 78 GeV/s takes place. The acceleration voltage is provided by four traveling-wave RF cavities (TWC) [28] operating at 200 MHz. The total length of the cycle is 21.6 s (a multiple of the basic machine period, 1.2 s).

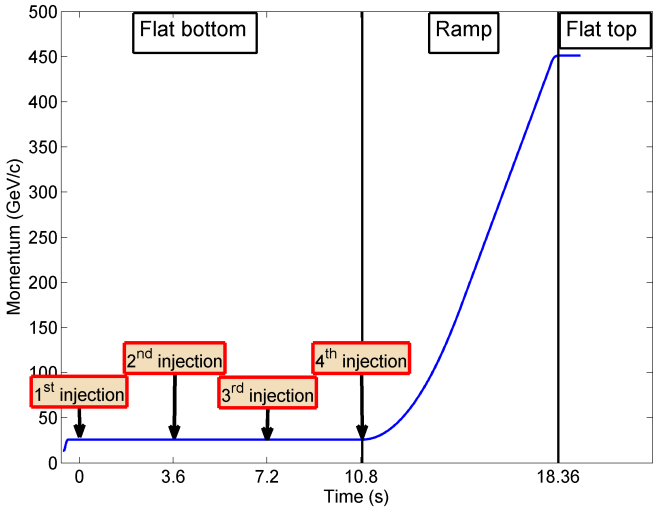

Figure 1.3: Beam momentum variation during the proton cycle in the SPS for the LHC filling.

The beam characteristics as well as the RF settings in the SPS have been chosen to minimize the particle losses, increase the longitudinal stability and produce a beam that fulfills the needs of the LHC. In particular, at PS-SPS transfer the longitudinal emittance ε_l is 0.35 eVs and the bunch length (4 standard deviations in the Gaussian case) is around 4 ns (produced after rotation in the PS). These values are determined by beam stability requirements both in PS and SPS. Smaller ε_l would give more margin for injection errors and hence less risk of capture loss (particles that are not captured in the RF buckets at injection), but will degrade the beam quality due to the decrease of the longitudinal instability thresholds (single and coupled-bunch) [29]. However, recent studies on the beam transfer from PS to SPS [30] demonstrated that the beam losses could be halved by optimizing the PS bunch rotation in longitudinal phase space. With higher voltage and optimized timings used for the rotation, the same bunch length and transmission (in the SPS) can be maintained for a 40% larger longitudinal emittance, which increases significantly the longitudinal beam stability [29]. This optimization of the bunch rotation though requires the use of additional RF cavities in the PS, which are currently reserved as spares.

The matched voltage at injection is 750 kV, but much higher capture voltage is used in operation ($\geq$2 MV). The higher voltage reduces the effect of beam loading [31] (see Chapter 5), provides more stability against coupled bunch instabilities at 26 GeV/c and produces some longitudinal emittance blow-up that helps stabilize the beam against instabilities later in the cycle. After the beam spends a short time (around 100 ms) at injection energy the emittance is $\varepsilon_l \approx 0.4$ eVs. A typical RF voltage programme used for the LHC-type proton beam during the operation in 2011 and 2012 is shown in Fig. 1.4. Note that these estimations correspond to the SPS Q26 optics (see below) used in operation until the September of 2012. Both measurments and simulations presented in the later Chapters of this thesis correspond to these SPS optics.

Up to about 200 GeV (around 14.5 s in the cycle), the 200 MHz voltage is adjusted for a constant bucket area (0.68 eVs for the example in Fig. 1.4). At flat bottom each PS batch is injected at 2 MV. However, in order to reduce the capture losses the RF voltage is within 50 ms

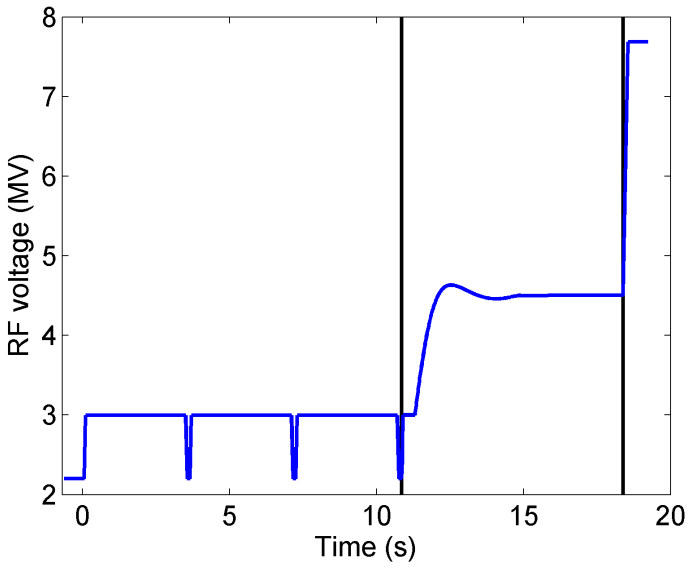

Figure 1.4: Typical voltage programme of the main 200 MHz RF system in the SPS, used in routine operation for LHC filling in 2011 and 2012 for 50 ns spaced beam with intensities up to 1.6×10^{11} p/b. The vertical lines indicate the start and the end of acceleration.

increased from 2 to 3 MV after each injection, as can be seen in Fig. 1.4. Above 200 GeV the voltage is kept constant (higher than the programmed values) to provide a larger bucket that is needed for the controlled longitudinal emittance blow-up. The latter is achieved by injecting band-limited noise through the phase loop of the 200 MHz RF system [32] and helps to stabilize the beam at high energy where the thresholds for both narrow-band and broad-band impedances are significantly decreased [29]. At flat top, the RF voltage is increased for reducing the bunch length before transferring the beam from the SPS 200 MHz bucket to the LHC 400 MHz bucket. The maximum presently available RF voltage of 7.5 MV is used for this manipulation.

Finally, in routine operation with LHC beams (50 ns bunch spaced with intensities up to 1.6×10^{11} p/b), a fourth harmonic RF system (800 MHz) is used as Landau cavity in bunch shortening mode for increasing the synchrotron frequency spread, which helps stabilizing the beam. There are two 800 MHz traveling wave cavities in the SPS. Only one is connected to the RF power, the second is idle. The voltage programme of the 800 MHz system is usually set to 1/10 of the main accelerating system voltage. The reason for this will be explained later in Chapter 4.

Both the controlled longitudinal emittance blow-up and the 800 MHz RF system increase significantly the longitudinal single and coupled bunch instability thresholds (see next Section), making possible the delivery to the LHC of beam with parameters that exceed the initial expectations [21]. An additional improvement in beam quality was achieved by lowering the transition gamma γ_t from 22.8 to 18 [33]. This new optics (Q20) was obtained by decreasing the integer tunes (26.13 and 26.18 in Q26 optics) by 6 units, resulting to a significant increase of the slippage factor $\eta = \gamma^{-2} - \gamma_t^{-2}$ (a factor of 2.8 at 26 GeV/c and 1.6 at 450 GeV/c) and thus to a subsequent increase of the thresholds for longitudinal coupled bunch instabilities, loss of Landau

damping and transverse mode coupling instability (TMCI) [34]. Note here that a proportional increase in the RF voltage $V_{\rm rf}$ is also needed to obtain the same bucket area, since the latter scales as $\sqrt{V_{\rm rf}/\left|\eta\right|}$. This means that the corresponding increase of the instability thresholds is true only as long as the available RF voltage is enough to provide the same longitudinal parameters (emittance, bunch length). As mentioned before, already the maximum RF voltage (7.5 MV) is used for beam transfer to the LHC, but the controlled emittance blow-up can also be reduced for the same intensity. Indeed the threshold for the loss of Landau damping $N_{\rm th}^{\rm LD}$ (for a non-accelerating bucket) due to the reactive impedance scales like [35]

$$N_{\rm th}^{\rm LD} \propto \epsilon_l^2 \left|\eta\right| \tau. \tag{1.2}$$

Thus one needs a smaller emittance $\epsilon_l \sim \sqrt{\eta}$ for stability, which gives the same bunch length τ in the Q20 optics as with the Q26. This scaling is in fact confirmed by many measurements performed in 2011 and 2012 [36]. The beam parameters of the LHC 25 and 50 ns beams, obtained by the end of the LHC operation run 1 until the end of 2012 are listed in Table 1.1.

Table 1.1: Characteristics of the 50 and 25 ns proton beams at 450 GeV/c in the SPS: 2012 achievements and HL-LHC requirements. The longitudinal emittance for the HL-LHC depends on the available RF voltage, where 15 MV are assumed for the low intensity beam [37].

	Achieved		**HL-LHC**	
Bunch spacing [ns]	50	25	50	25
Bunch intensity [$\times 10^{11}$]	1.6	1.3	3.6	2.2
Number of bunches	4×36	4×72	4×36	4×72
Long. emittance [eVs]	0.45	0.5	0.7	0.7
Bunch Length [ns]	1.5	1.55	< 1.8	< 1.8

In order to fully exploit the potential of the LHC and its future upgrades for higher luminosity, the injectors will have to deliver proton beams with significantly higher beam intensity compared to the current operation. The activities concerning the luminosity upgrade of the LHC itself are incorporated in the High Luminosity LHC (HL-LHC) project [38] and the upgrade of the injector complex is subject of the LHC Injectors Upgrade (LIU) project [39]. In particular, the LIU project aims at consolidating and upgrading the existing injector synchrotrons (PSB, PS and SPS) in the CERN complex and using the new linac presently in construction (LINAC4). The characteristics of the 25 and 50 ns proton beams according to the HL-LHC requirements [40] are presented in Table 1.1. After commissioning the LINAC4 and upgrading the PSB and the PS, the main performance limitations of the LHC injector complex are beam instabilities and high intensity effects in the SPS, the longitudinal aspects of which are discussed below.

1.4 Longitudinal instabilities in the SPS.

The longitudinal multi-bunch instability observed during acceleration in the SPS has very low intensity threshold: one batch of 36 bunches at 50 ns spacing with 2×10^{10} p/b and nominal injected longitudinal emittances $\epsilon_l = 0.35$ eVs becomes unstable during the ramp, even with the RF feedback, feed-forward and longitudinal damper (low modes) in operation [41]. This

instability threshold does not depend on the number of batches in the ring, i.e. the same instability threshold in energy is observed for a given intensity per bunch with one or four batches of the 50 ns beam in the machine (with gaps of 250 ns between batches) as can be seen in Fig 1.5. Possible sources of this instability are the fundamental and higher order modes

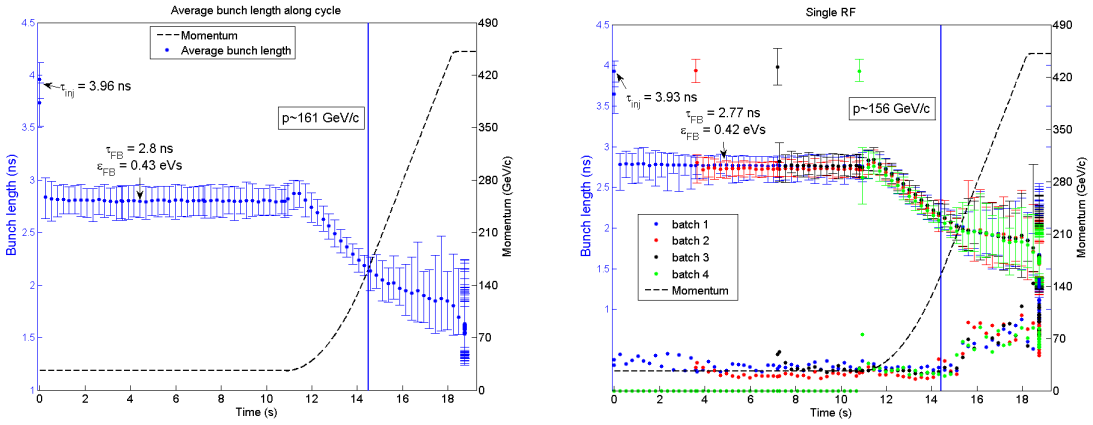

Figure 1.5: Averaged bunch length variation along the cycle for single batch (left) and 4 batches (right) of the 50 ns LHC beam in a single RF system. Intensity of $N_b \approx 1.6 \times 10^{11}$ p/b. The peak-to-peak bunch length spread within the batch is shown by the error bars. The vertical lines indicate the instability onset.

(HOMs) of the main (200 MHz) and high harmonic (800 MHz) RF systems, since their relatively low quality factors of 150, 500 and 300 accordingly are compatible with the short-range wake that is driving this instability. The search for other impedance sources in the SPS ring is ongoing [42].

As expected from calculations, in addition to the impedance, the coupled-bunch instability threshold clearly depends on the beam energy and the longitudinal emittance [29]

$$N_{\rm th}^{\rm CB} \propto \frac{\epsilon_l^2 \, |\eta|}{E_0 \tau}, \tag{1.3}$$

where E_0 is the energy of the synchronous particle, η is the slip factor and τ is the bunch length. More dense bunches become unstable earlier in the cycle. A comparison of LHC beams with different bunch spacing T_b shows that the energy threshold scales roughly as $1/E_{\rm th} \propto N_b/T_b$, or with total beam current. Indeed, as can be seen in Fig 1.6 for the Q26 optics, the 50 ns beam with a bunch intensity of $N_b = 1.6 \times 10^{11}$ p was unstable around 160 GeV/c and the 25 ns beam with $N_b = 1.2 \times 10^{11}$ p at 110 GeV/c. Higher intensity 25 ns and 50 ns beams were also at the limit of stability on the 26 GeV/c flat bottom.

As was mentioned in the previous Section, in routine operation, the fourth harmonic 800 MHz RF system is used in the BS mode [10] in order to increase the synchrotron frequency spread and thus increase both the multi- and single-bunch instability thresholds. To obtain that the phase Φ_2 between the two RF systems (see Eq. (1.1)) is programmed during the acceleration cycle as

$$\Delta\Phi_2 = -4\phi_{s0} + \pi, \tag{1.4}$$

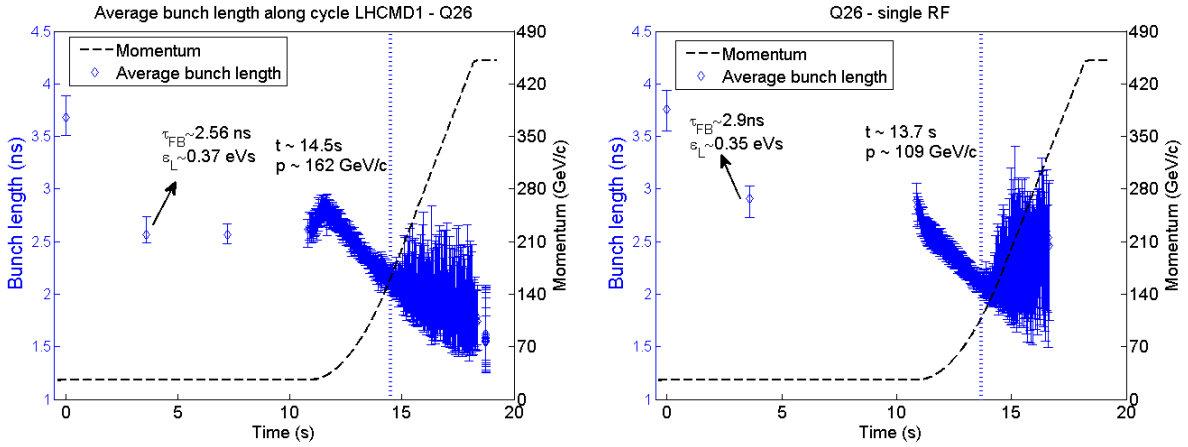

Figure 1.6: Averaged bunch length variation along the SPS cycle for single batch of the 50 ns (left) and the 25 ns (right) LHC beam in a single RF system with average intensity of $N_b = 1.6 \times 10^{11}$ p/b and $N_b = 1.2 \times 10^{11}$ p/b accordingly. The peak-to-peak bunch length spread within the batch is shown by the error bars. The vertical lines indicate the instability onset. Both cases correspond to the Q26 optics.

where ϕ_{s0} is the synchronous phase in a single RF system. However in reality for high intensity beam the phase Φ_2 is strongly affected by beam loading (see Chapter 5) in the 800 MHz RF system itself. In the SPS, unlike many other accelerators, only BS mode is used for beam stabilization, since for the nominal bunch size the beam is unstable in BL mode all along the cycle, both for single and multi-bunch cases. Figure. 1.7 presents an example of a single batch of the 50 ns LHC beam in BS and BL modes with an average intensity of $N_b = 1.2 \times 10^{11}$ p/b. The large errobars in the BL mode case indicate that the beam is unstable even at the injection energy.

Many studies were conducted in order to understand these observations [10,43] and two main restrictions for the BL mode were identified:

1. The very tight requirements on the accuracy of the relative phase Φ_2 between the two RF systems, which is very difficult to achieve due to strong beam loading in both the main and high harmonic RF systems [10].

2. The non-monotonic behavior of the synchrotron frequency distribution as a function of the longitudinal emittance (essential for long bunches) reducing the instability threshold (see Chapter 3).

These two restrictions, also discussed in [41], are thoroughly studied in this thesis together with other issues related to the beam stability in a double RF system. In particular, the beam stability with respect to the phase Φ_2 between the two RF systems is addressed for the case of the SPS. In addition, the effect that global or local maxima in the synchrotron frequency distribution as a function of the longitudinal emittance have on beam stability is further investigated, both by analytical calculations and particle simulations. Note that this effect also appears in the BS mode for sufficiently large voltage ratio V_2/V_1 and harmonic ratio $n = h_2/h_1 > 2$.

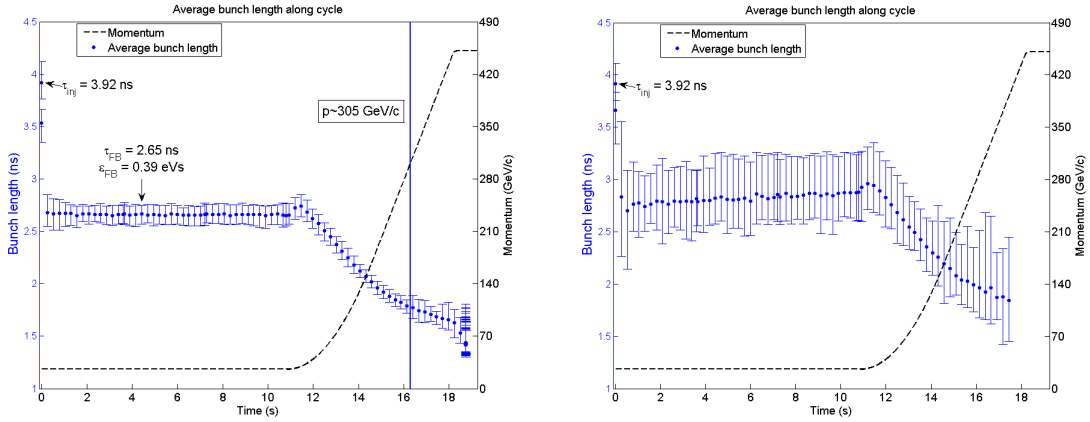

Figure 1.7: Averaged bunch length variation along the cycle for single batch of the 50 ns LHC beam in a double RF system operated in BS mode (left) and BL mode (right). The voltage ratio is $V_2/V_1 = 0.1$. Intensity of $N_b = 1.2 \times 10^{11}$ p/b. The peak-to-peak bunch length spread within the batch is shown by the error bars. In the case of BS mode the vertical line indicates the instability onset, while in BL mode the large errobars mean that the beam is unstable all along the cycle. Both cases correspond to the Q26 optics.

Even with the addition of the 800 MHz RF system, individual bunches injected with small longitudinal emittance can still become unstable during the ramp [35]. An example of the bunch lengths at injection and extraction for a 50 ns beam with an average intensity of $N_b = 1.2 \times 10^{11}$ p/b is presented in Fig. 1.8. As one can see, the bunches with smaller bunch length (emittances) at injection ($\tau < 3.5$ ns) become unstable during ramp or at flat top. This observation could be an indication of the loss of Landau damping for single bunches due to the reactive impedance of the SPS. Note that the loss of Landau damping in a single harmonic RF system, based on the Sacherer criterion [44], scales as [29]

$$N_{\mathrm{th}}^{\mathrm{LD}} \propto \frac{\epsilon_l^2 \, |\eta| \, \tau}{E_0}, \tag{1.5}$$

and as in the case of coupled bunch instability, lower threshold is expected at higher beam energies. Therefore, larger emittances are needed for stability at flat top. However, injecting larger emittances from the PS results in higher particle losses, although resent studies [30] (without taking into account intensity effects) have shown that larger emittances can be injected in the SPS with the same transmission, by using an additional RF system in the PS and optimizing the rotation time. Nevertheless, a controlled emittance blow-up during the SPS ramp is required for stability, which is applied in routine operation by introducing band-limited phase noise in the 200 MHz RF system [32].

However, the emittance blow-up in a double RF system has its own limitations due to the presence of beam loading. This issue is also investigated in details in this thesis. In particular, it is shown that the non-uniform bunch length distribution obtained at flat top after the controlled emittance blow-up (see Fig. 1.9) can be attributed to the residual beam loading in the 200 MHz RF system (with one-turn feedback and feed-forward systems in operation) [45].

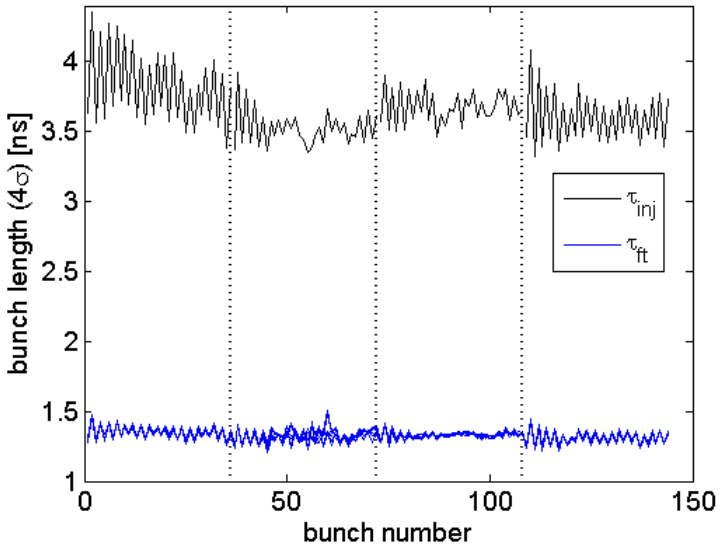

Figure 1.8: Bunch length at injection (upper trace) and on flat top (lower traces) for the 50 ns LHC beam with intensity of $N_b \approx 1.2 \times 10^{11}$ p/b and without controlled emittance blow-up. The 800 MHz RF is on in BS mode. Bunches in the second batch with small emittances are unstable at flat top as can be seen from the bunch length oscillations.

A clear gain in beam stability was expected with the new Q20 optics, since the longitudinal instability thresholds scale roughly with the slip factor η. Many measurements performed in 2011 and 2012 [33, 36] confirmed this expectation and resulted finally in the replacement of the Q26 optics by the Q20 in 2012 operation run. A detailed analysis of the studies concerning the Q20 optics can be found in [34]. Significant improvement in beam stability was obtained on the flat bottom. However on the flat top the high harmonic RF system is still insufficient for stability (due to the limited RF voltage) even for the operational bunch intensities (both for 50 ns and 25 ns LHC beams) and one needs in addition the controlled emittance blow-up, which however can be smaller than in nominal optics.

Using all the measures to cure the longitudinal instabilities, i.e. the 800 MHz RF system operating in BS mode, the controlled emittance blow-up during the ramp and the new Q20 optics, the SPS was able to reliably accelerate much higher beam intensities (see Table 1.1) than expected [21]. Note that in order to achieve those beam intensities many measurements were performed during the machine development (MD) sessions in 2010 - 2012 [46]. Figure 1.10 presents one example of the 25 ns LHC beam, where stable beam with an average bunch intensity of $N_b \approx 1.3 \times 10^{11}$ p was obtained at flat top with parameters acceptable for injection into the LHC. Note that this result represents a record performance of the SPS with the LHC beams. However, it should be emphasized that, due to losses related to the beam capture and losses on the flat bottom, an intensity of more than $N_b \approx 1.4 \times 10^{11}$ p/b had to be injected in this case. When injecting beams with even higher intensity, the transmission was significantly decreasing (for example about 85% for $N_b \approx 1.55 \times 10^{11}$ p at injection). Similar issues were also faced with the 50 ns LHC beam for reaching high intensities at flat top ($N_b > 1.6 \times 10^{11}$ p). In order

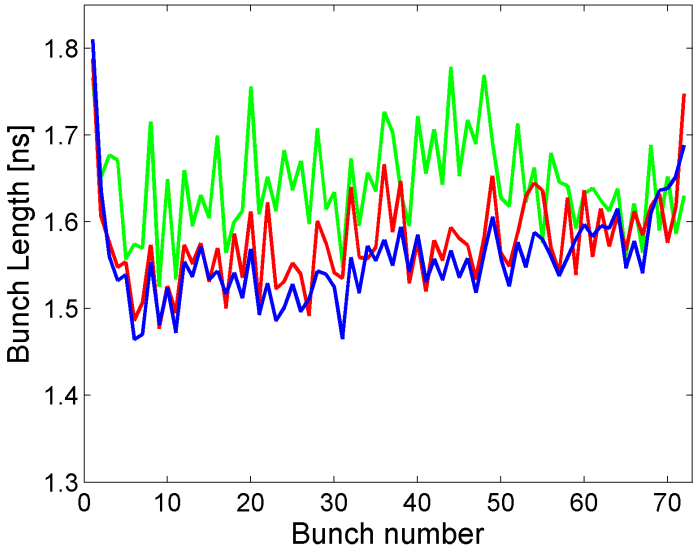

Figure 1.9: Bunch length distribution along the 25 ns batch before the controlled longitudinal emittance blow-up (green), just after (red) and at the flat top of the cycle (blue). Notice the non-uniform shape after the blow-up is applied.

to stabilize the beam with even higher intensities more longitudinal emittance blow-up will be required, which in turn requires larger RF voltage for increasing the bucket size in order to avoid particle loss. However, less RF voltage will be seen by the beam due to the effect of beam loading and the limited currently available RF power. This becomes critical in particular for beam extraction to the LHC, where the maximum available voltage (7.5 MV) is already used to compress the bunch for injection into the LHC 400 MHz bucket. For that reason, an upgrade of the SPS RF system including the rearrangement of the cavities and the construction of two additional power plants, which will allow to have higher RF voltage is in preparation [37] as a part of the LIU project.

Therefore, it is very important to fully understand the benefits that a higher harmonic RF, can provide and also to identify the limitations or the problems that may exist for higher beam intensities.

1.5 Outline of the Thesis

In Chapter 2 a review of the longitudinal beam dynamics is presented. First, the basis of longitudinal motion in synchrotrons without intensity effects is presented. Basic equations and parameters are defined for a single and a double harmonic RF system. Later, the effects of the beam intensity are introduced, starting from the potential well distortion. The Vlasov equation is presented and used together with the perturbation formalism to analyze the coherent motion of the particles inside the bunch, through the dispersion equation. Finally, the concept of Landau damping is introduced and described for a bunched beam in the longitudinal plane.

In Chapter 3 the phenomenon of loss of Landau damping is considered in a single and

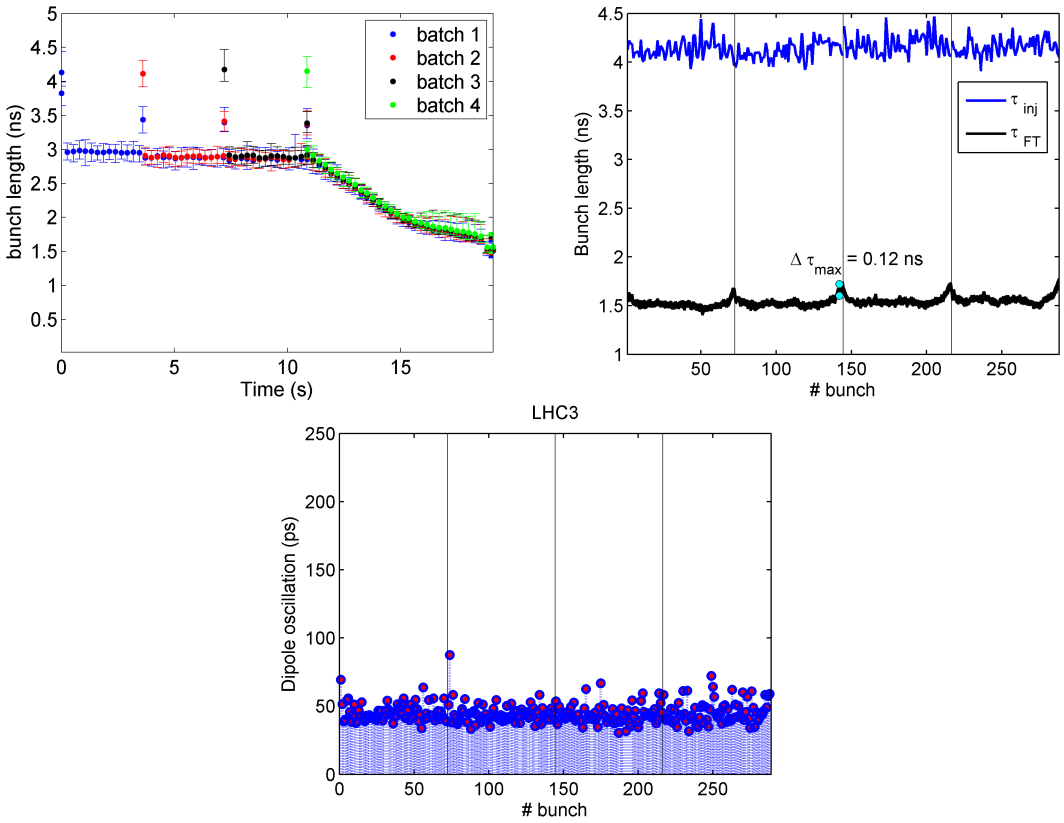

Figure 1.10: Measurements with four batches of 72 bunches spaced by 25 ns with $N_b \approx 1.3 \times 10^{11}$ p/b at SPS. The average bunch length evolution along the cycle (top left), the bunch length distribution along the bunch train at injection and at at top (top right) and the dipole oscillations at at top (bottom right) show stable beam conditions.

a double RF system, in the presence of reactive impedance. Instability thresholds are found both from calculations (by solving numerically the linearized Vlasov equation) and from particle simulations. The analysis is extended to different harmonic ratios between the two RF systems, and the results are used to explain experimental observations during the p$\bar{\text{p}}$ operation of the SPS.

Then in Chapter 4, the particular situation of the SPS is considered, by presenting the single bunch instabilities studies in the double RF system, consisting of the main and the 4^{th} harmonic RF systems. Initially, a beam based method of calibrating the phase between the two RF systems which is used in operation is presented. Then measurements for different values of this phase are shown, providing the stability region for the specific set of parameters used. The stability region is also reproduced by macroparticle simulations performed for the same conditions as in the measurements using the current SPS impedance model and compared with the measurements. Finally, the results are explained theoretically through the mechanism of the loss of Landau damping and more precisely, by the analysis of the synchrotron frequency distribution of the particles inside the bunch.

Chapter 5 deals with issues of the controlled longitudinal emittance blow-up applied, for stability reasons, to the multi-bunch LHC beams in the SPS. Beam measurements are presented, where a non-uniform emittance blow-up is observed together with an anti-symmetric variation of the bunch positions along the batch. The effect of beam loading in a traveling-wave cavity is introduced together with the beam loading compensation currently applied in the SPS TW RF cavities. It is shown that the observed anti-symmetric pattern in the bunch positions, is determined by the beam loading in the main RF system. Finally, by calculating the synchrotron frequency distribution of the particles inside different bunches along the batch, the non-uniform emittance blow-up can be explained.

Chapter 2

Review of longitudinal beam dynamics

In this Chapter some important parameters commonly used in accelerator physics to describe the longitudinal motion of the particles are defined. Furthermore, a short introduction to the necessary theory is also presented, and some useful formulas which will be applied later in the thesis are derived.

2.1 Synchrotron motion

2.1.1 Coordinate system

To describe the longitudinal motion of the particles we first need to define the coordinate system. There is a range of possibilities for the selection of the longitudinal phase-space variables. However, since we want to apply the Hamiltonian formalism, the two variables have to be canonical conjugates [47]. Examples of such pairs are position and momentum (x, p) or time and energy (t, E). In circular accelerators though, and for practical reasons, the azimuthal angle θ of the ring is often used instead of t

$$\theta = \omega_0 t, \tag{2.1}$$

where ω_0 is the angular revolution frequency, $\omega_0 = 2\pi f_0$.

The motion of the particles is described with respect to the motion of a reference particle [48] which has a designated energy E_0 and travels along a close orbit (of length C_0) that passes through the center of any magnet at revolution period $T_0 = 2\pi/\omega_0$. This particle is referred to as synchronous particle, since it is synchronized with the RF voltage waveform (that is normally used to accelerate the beam). Therefore, denoting the phase-space coordinates of the synchronous particle with (θ_0, E_0), the coordinates of an arbitrary particle, which deviate only slightly from those of the synchronous one, can be written:

$$\begin{aligned} \theta &= \theta_0 + \Delta\theta \\ E &= E_0 + \Delta E. \end{aligned} \tag{2.2}$$

For convenience we will use the RF phase angle $\phi = \omega_{\mathrm{rf}} t$, where ω_{rf} is the angular frequency of the RF voltage. In the absence of acceleration, after each revolution along the ring, the synchronous particle will encounter the RF voltage at the same phase $\phi = \phi_{\mathrm{s}}$ called synchronous phase. This requires that

$$\omega_{\mathrm{rf}} = h\omega_0, \tag{2.3}$$

where h is a positive integer called the harmonic number. Its value can range from one up to several thousand. Again, related to the synchronous particle, the phase of any other particle can be written as

$$\phi = \phi_s + \Delta\phi. \tag{2.4}$$

2.1.2 Energy gain and transit time factor

Charged particles can be accelerated using longitudinal electric fields. In synchrotrons, this electric field $\mathscr{E}$ is provided by RF cavities. The time dependence of the longitudinal electric field in the RF gap is given by

$$\mathscr{E} = \mathscr{E}_0 \sin(\omega_{rf} t), \tag{2.5}$$

where $\mathscr{E}_0$ is the amplitude of the electric field. Note that here $\mathscr{E}_0$ is assumed to be constant in the RF gap, which in many practical cases is a good approximation. For circular accelerators, the origin of time is taken at zero crossing of the RF voltage waveform with positive slope. The phase ϕ of the RF voltage when a particle crosses the middle of the accelerating gap (at z =0, z being the longitudinal coordinate) is called the phase of the particle with respect to the RF voltage, and for the synchronous particle $\phi = \phi_s$. If the change in velocity of the particle when crossing the gap is neglected, the phase of the synchronous particle at position z in the gap reads

$$\omega_{rf} t = \phi_s + \frac{\omega_{rf}}{v} z, \tag{2.6}$$

where v is the particle velocity in the middle of the gap.

The energy gain δE_0 of the synchronous particle with charge q, passing through an RF cavity with a gap width g is given by [49]

$$\delta E_0 = q \int_{-g/2}^{g/2} \mathscr{E}_0 \sin(\phi_s + \frac{\omega_{rf}}{v} s) ds, \tag{2.7}$$

where it is assumed that the gap is symmetric with respect to the plane $z = 0$. Then

$$\delta E_0 = q \mathscr{E}_0 g T \sin\phi_s, \tag{2.8}$$

where T is the transit time factor

$$T = \frac{\sin(\omega_{rf} g/2v)}{\omega_{rf} g/2v}, \tag{2.9}$$

which accounts for the fact that the particle passes through the RF gap within a finite time interval. The effective peak voltage $\hat{V}$ seen by the particle is thus

$$\hat{V} = \mathscr{E}_0 g T, \tag{2.10}$$

which depends on the particle velocity v through the transit time factor. Below, for relativistic beams, this effect will be neglected so that all particles will be considered as experiencing the same peak voltage. Finally, the energy gain of the synchronous particle is:

$$\delta E_0 = q \hat{V} \sin\phi_s. \tag{2.11}$$

This energy gain per turn of the synchronous particle should be followed by a variation of the magnetic field in dipoles to keep the particle on the designed orbit of constant radius, R. Usually, in most synchrotrons the acceleration cycle lasts for some thousands to millions of revolutions, which means that the synchronous particle gains a relatively small amount of energy during each revolution. In all the cases considered below this assumption is considered, i.e. E_0 to be a smooth function of t

$$\frac{\delta E_0}{T_0} = \frac{dE_0}{dt} \Rightarrow \frac{dE_0}{dt} = \frac{\omega_0}{2\pi} q\hat{V} \sin\phi_\mathrm{s}, \tag{2.12}$$

or in terms of the synchronous momentum p_0

$$\frac{dp_0}{dt} = \frac{q\hat{V}\sin\phi_\mathrm{s}}{2\pi R}. \tag{2.13}$$

2.1.3 Longitudinal equations of motion

According to Eq. (2.3) the phase coordinate ϕ is related to the azimuthal angle θ by $\phi = h\theta$, and thus one can write

$$\Delta\phi = -h\Delta\theta. \tag{2.14}$$

The convention for the sign shows that particles which lag behind the synchronous one ($\Delta\theta < 0$) will arrive later in the RF cavity ($\Delta\phi > 0$). Using the last equation, the angular revolution frequency deviation of an arbitrary particle from the synchronous one can be written as

$$\Delta\omega = \frac{d}{dt}(\Delta\theta) = -\frac{1}{h}\frac{d}{dt}(\Delta\phi) = -\frac{1}{h}\frac{d\phi}{dt}, \tag{2.15}$$

where it was assumed that ϕ_s is changing much slower in time ($d\phi_s/dt \ll d\phi/dt$). Since $\omega = 2\pi\beta c/C$, where $\beta = v/c$ (c is the speed of light) and C is the circumference of the machine, the relative change in angular revolution frequency with respect to the synchronous particle can be also expressed as:

$$\frac{\Delta\omega}{\omega_0} = \frac{\Delta\beta}{\beta_0} - \frac{\Delta C}{C_0}, \tag{2.16}$$

where β_0 and C_0 are the velocity (in units of c) and the close-orbit length of the synchronous particle.

Particles with different energy (or momentum p) will be affected differently by the bending magnets and due to that they will move along different orbits, C. This effect is described by the momentum compaction factor α, which in first order gives (see for example [48])

$$\alpha = \frac{\Delta C/C_0}{\Delta p/p_0}, \tag{2.17}$$

where p_0 is the momentum of the synchronous particle. Usually $\alpha > 0$, but it can also be negative.

From the relativistic momentum $p = m_0\gamma\beta c$, with $\gamma = 1/\sqrt{1-\beta^2}$ being the Lorentz factor and m_0 the particle's rest mass, one gets:

$$\frac{\Delta p}{p_0} = \gamma^2\frac{\Delta\beta}{\beta_0}. \tag{2.18}$$

Combining Eqs. (2.16), (2.17) and (2.18) gives:

$$\frac{\Delta\omega}{\omega_0} = \left(\frac{1}{\gamma^2} - \alpha\right)\frac{\Delta p}{p_0}. \tag{2.19}$$

Introducing the *slip factor*

$$\eta = \alpha - \frac{1}{\gamma^2}, \tag{2.20}$$

one finally has:

$$\frac{\Delta\omega}{\omega_0} = -\eta\frac{\Delta p}{p_0}. \tag{2.21}$$

Note that η changes sign when γ passes through $\gamma_{\mathrm{tr}} \equiv 1/\sqrt{\alpha}$, and corresponding energy is known as the transition energy of the ring. The transition energy plays a very important role in the beam stability which will be consider later in this Chapter.

Substituting Eq. (2.21) into Eq. (2.15) gives the first equation of motion:

$$\frac{d\phi}{dt} = h\eta\omega_0\frac{\Delta p}{p_0} = \frac{h\eta\omega_0}{\beta^2}\frac{\Delta E}{E_0} = \frac{h\eta\omega_0^2}{\beta^2 E_0}\left(\frac{\Delta E}{\omega_0}\right). \tag{2.22}$$

In the equation above, the relation

$$\frac{\Delta p}{p_0} = \frac{1}{\beta^2}\frac{\Delta E}{E_0}$$

was used, and the coordinates $\left(\phi, \frac{\Delta E}{\omega_0}\right)$ were introduced as the canonical phase-space coordinates. Note that from here on β_0 is replaced by β since, for the relativistic beams considered below, the relative deviations from the synchronous particle are negligible, $(\beta - \beta_0)/\beta_0 \ll 1$.

The next step is to find the second equation of motion, i.e. the time evolution of the energy deviation ΔE. We assume at this point that the energy of the beam can be changed only by the applied RF field, neglecting any energy variation due to the interaction with the environment or due to the synchrotron radiation. In addition, the sinusoidal RF voltage is replaced by a generalized RF voltage $V(\phi)$, to take into account the more general case, where higher harmonics are added to the fundamental sinusoidal RF field. The only conditions $V(\phi)$ needs to fulfill are periodicity at the lowest RF harmonic and the absence of a direct current (DC) component:

$$V(\phi) = V(\phi + 2\pi) \qquad \text{and} \qquad \int_0^{2\pi} V(\phi)d\phi = 0.$$

Therefore, the energy that a particle of charge q and phase ϕ gains during one turn is

$$\delta E = qV(\phi). \tag{2.23}$$

Expressing this energy gain with respect to the energy gain of the reference particle, which finds the RF field always in phase ϕ_{s}, one gets:

$$\delta E - \delta E_0 = q\left[V(\phi) - V(\phi_{\mathrm{s}})\right]. \tag{2.24}$$

Assuming again that both E and E_0 are smooth functions of t, one can write the previous equation as

$$\frac{\dot{E}}{\omega} - \frac{\dot{E}_0}{\omega_0} = \frac{1}{2\pi} q \left[V(\phi) - V(\phi_\mathrm{s}) \right], \tag{2.25}$$

where $\dot{E} \equiv dE/dt$ and $\dot{E}_0 \equiv dE_0/dt$. It can be shown (for example [48,49]) that the last equation can be approximated by

$$\frac{d}{dt}\left(\frac{\Delta E}{\omega_0}\right) = \frac{q}{2\pi} \left[V(\phi) - V(\phi_\mathrm{s}) \right]. \tag{2.26}$$

Equations (2.22) and (2.26) form the system of equations of longitudinal motion.

Combining the two equations of motion and assuming that E_0 varies very slowly during the acceleration cycle, leads to a second order differential equation for the phase motion

$$\frac{d^2\phi}{dt^2} - \frac{h\eta\omega_0^2 q}{2\pi\beta^2 E_0} \left[V(\phi) - V(\phi_\mathrm{s}) \right] = 0. \tag{2.27}$$

Multiplying Eqs. (2.22) and (2.26) across

$$\frac{h\eta\omega_0^2}{\beta^2 E_0}\left(\frac{\Delta E}{\omega_0}\right)\frac{d}{dt}\left(\frac{\Delta E}{\omega_0}\right) = \frac{q}{2\pi}\left[V(\phi) - V(\phi_\mathrm{s}) \right]\frac{d\phi}{dt}, \tag{2.28}$$

and integration, one gets

$$H = \frac{h\eta\omega_0^2}{2\beta^2 E_0}\left(\frac{\Delta E}{\omega_0}\right)^2 - \int_{\phi_s}^{\phi} \frac{q}{2\pi}\left[V(\phi') - V(\phi_\mathrm{s}) \right] d\phi', \tag{2.29}$$

where H is the first integral of the longitudinal motion [47] of the particles circulating in the ring, which is constant along an orbit in the phase-space defined by the conjugate variables $(\phi, \Delta E/\omega_0)$. This function corresponds to the Hamiltonian of the system. Indeed, taking partial derivatives with respect to the phase-space variables we get:

$$\frac{\partial H}{\partial \phi} = -\frac{q}{2\pi}\left[V(\phi) - V(\phi_\mathrm{s}) \right] = -\frac{d}{dt}\left(\frac{\Delta E}{\omega_0}\right), \tag{2.30}$$

and

$$\frac{\partial H}{\partial (\Delta E/\omega_0)} = \frac{h\eta\omega_0^2}{\beta^2 E_0}\left(\frac{\Delta E}{\omega_0}\right) = \frac{d\phi}{dt}, \tag{2.31}$$

which are the canonical Hamilton equations [47] in these variables. The first term in Eq. (2.29) can be identified as the kinetic energy and the second as the potential energy

$$U(\phi) = -\int \frac{q}{2\pi}\left[V(\phi) - V(\phi_\mathrm{s}) \right] d\phi \tag{2.32}$$

showing that the function H is an expression for the total energy of the particle, which in a conservative system has to remain constant [47].

2.1.4 Single harmonic RF system and phase-stability

For the case of a single RF system with angular frequency $\omega_{\mathrm{rf}} = h\omega_0$ Eq. (2.27) can be written

$$\frac{d^2\phi}{dt^2} - \frac{h\eta\omega_0^2 qV_0}{2\pi\beta^2 E_0}(\sin\phi - \sin\phi_s) = 0. \tag{2.33}$$

To find out whether the motion of the particles under the influence of this RF field is stable we can consider small deviations from ϕ_{s}. In that case the parenthesis above can be replaced by

$$(\sin\phi - \sin\phi_s) \approx \Delta\phi\cos\phi_{\mathrm{s}}, \tag{2.34}$$

where $\Delta\phi = \phi - \phi_{\mathrm{s}}$. Combining this with (2.33) and assuming again that ϕ_{s} changes slowly in time, leads to a simplified equation

$$\frac{d^2(\Delta\phi)}{dt^2} - \frac{h\eta\omega_0^2\cos\phi_{\mathrm{s}} qV_0}{2\pi\beta^2 E_0}(\Delta\phi) = 0. \tag{2.35}$$

This equation describes a harmonic oscillator with an angular frequency

$$\omega_{\mathrm{s0}} = \sqrt{-\frac{h\omega_0^2\eta\cos\phi_{\mathrm{s}} qV_0}{2\pi\beta^2 E_0}} \tag{2.36}$$

provided that ω_{s0} is a real and positive number. Therefore, this condition can be written as

$$\eta\cos\phi_{\mathrm{s}} < 0. \tag{2.37}$$

Keeping also in mind that acceleration needs $V_s > 0$ and thus $\sin\phi_{\mathrm{s}} > 0$, two different regions of oscillatory motion can be identified, depending on whether the accelerator is operated below or above transition energy

- Below transition $(\gamma < \gamma_{\mathrm{tr}})$: $\eta < 0 \;\Rightarrow\; \cos\phi_{\mathrm{s}} > 0 \;\&\; \sin\phi_{\mathrm{s}} > 0 \;\Rightarrow\; 0 < \phi_{\mathrm{s}} < \pi/2$
- Above transition $(\gamma > \gamma_{\mathrm{tr}})$: $\eta > 0 \;\Rightarrow\; \cos\phi_{\mathrm{s}} < 0 \;\&\; \sin\phi_{\mathrm{s}} > 0 \;\Rightarrow\; \pi/2 < \phi_{\mathrm{s}} < \pi$

This principle of phase-stability assures that ensembles of particles can be accelerated in synchrotrons even if they are not exactly at the synchronous phase and energy. Such particles just oscillate around the reference particle. The idea of phase-stability due to RF focusing is schematically presented in Fig. 2.1.

Below transition ($\eta < 0$) a particle with higher momentum than the synchronous one ($\delta p > 0$) will also have higher revolution frequency ($\delta\omega > 0$), as can be seen from Eq. (2.21) and therefore it will arrive earlier to the RF gap (point N_1). That means that it will receive less energy gain than the synchronous particle (point P_1) and at the next turn will approach more to ϕ_{s}. Similarly, a lower energy particle will arrive at the RF gap later (point M_1) and gain more energy than the synchronous one. The situation is reversed above transition, where the synchronous phase has to be shifted at $\pi - \phi_{\mathrm{s}}$ (point P_2). Note here that in the case when no acceleration is applied to the synchronous particle i.e.

$$V(\phi_{\mathrm{s}}) = 0 \Rightarrow \sin(\phi_{\mathrm{s}}) = 0$$

the above conditions give for the synchronous phase

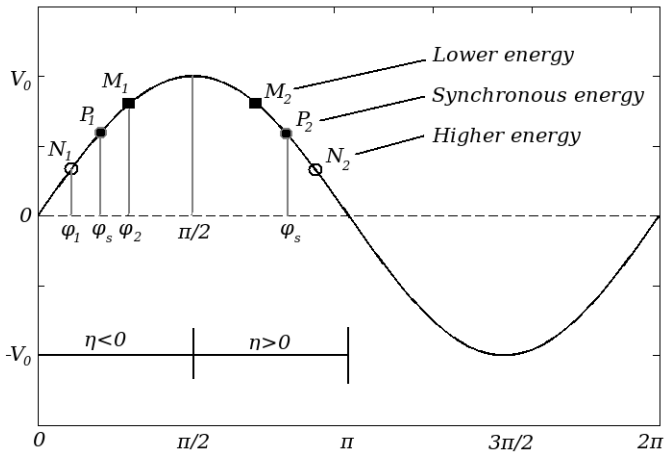

Figure 2.1: Schematic drawing of an RF wave and the RF phase angles of the synchronous particles P_1, P_2, particles with higher momentum N_1, N_2 and particles with lower momentum M_1, M_2, below ($\eta < 0$) and above ($\eta > 0$) the transition energy, respectively.

- $\phi_s = 0$, below transition or
- $\phi_s = \pi$, above transition.

The stability of the particle motion can be better understood from the plot of the RF potential. Let us first consider the Hamiltonian for the sinusoidal RF field

$$H = \frac{h\eta\omega_0^2}{\beta^2 E_0}\frac{1}{2}\left(\frac{\Delta E}{\omega_0}\right)^2 + \frac{qV_0}{2\pi}\left[\cos\phi - \cos\phi_s + (\phi - \phi_s)\sin\phi_s\right], \tag{2.38}$$

where the potential energy is:

$$U(\phi) = \frac{qV_0}{2\pi}\left[\cos\phi - \cos\phi_s + (\phi - \phi_s)\sin\phi_s\right]. \tag{2.39}$$

Figure 2.2 (left) presents $U(\phi)$ for the cases of $\phi_s = \pi$ (no acceleration) and $\phi_s = \pi - \pi/6$ ($\eta > 0$).

Near the synchronous phase the particles feel a restoring force which allows them to execute oscillations around it. Hence, in phase-space they follow closed trajectories with an angular frequency ω_s called the angular synchrotron frequency [1], which in the case of small amplitude oscillations ($\phi - \phi_s = \Delta\phi \ll 1$) is close to ω_{s0}, see Eq. (2.36). However, the trajectories of the particles with large deviations from ϕ_s are not bounded any more by the potential well and so their motion is not oscillatory. This boundary is shown in Fig. 2.2 (left plot) by the horizontal dashed lines.

The division of the phase-space into regions of bounded and unbounded motion in synchrotrons is the reason of grouping the particles into bunches. The boundary between these two

[1] Typically ω_s/ω_0 is of the order $\leq 10^{-3}$ for proton synchrotrons, which justifies the assumption of small changes in particle's energy during one revolution period, see Eq. (2.12).

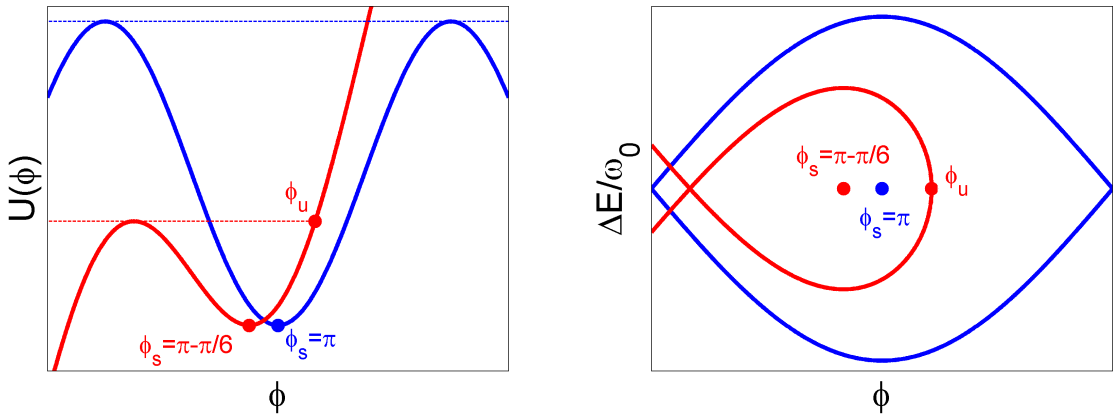

Figure 2.2: The left plot presents the RF potential $U(\phi)$ for $\phi_s = \pi$ (blue curve) and $\pi - \pi/6$ (red curve) ($\eta > 0$). The horizontal dashed lines show the maximum energy for stable motion. The right plot shows the corresponding buckets using the same color convention. The phase ϕ_u presents the turning point of the separatrix.

regions is called the separatrix, while the phase-space area enclosed by the separatrix is called the bucket. Examples of the buckets that correspond to the potentials of Fig. 2.2 are presented on the right plot using the same color convention. Particles that are inside these separatrices can be accelerated to high energies, whiles those that are not captured (outside the separatrix) are lost. Note that for the blue curves in Fig. 2.2 $\phi_s = \pi$ and thus $U(\phi_s) = 0$. This means, as was mentioned before, that the particles are not accelerated. In this special case we have a stationary bucket.

Coming back to the phase-stability condition (2.37), one can see that if the energy of the particles is such that during acceleration γ crosses γ_{tr}, the synchronous phase is shifted from the positive to the negative slope of the RF voltage waveform. For that reason, during operation, the RF phase must quickly be shifted from ϕ_s to $\pi - \phi_s$ as transition is crossed. This situation often occurs at proton synchrotrons where extra care needs to be taken, in order to overcome the difficulties that follow the transition crossing (particle loss, phase-space dilution and instabilities due to intensity effects etc.). Transition crossing is not discussed in this thesis, since for the LHC beam in the SPS the particles are injected above the transition energy ($\gamma_t = 22.8$).

2.1.5 Double RF system

Let's assume now the case where the accelerator is operated with a double RF system with a ratio n between the frequencies of the main and the higher harmonic RF system. The total voltage seen by the particles is (see for example [10])

$$V_t = V_1 \sin\phi + V_2 \sin(n\phi + \Phi_2), \tag{2.40}$$

where V_1, V_2 are the voltage amplitudes of the main and the higher harmonic RF systems and Φ_2 is the relative phase between them. Note that the RF frequencies involved need not

be harmonically related to each other. It is sufficient that both are multiple of the revolution frequency. However, in that case the phase Φ_2 will be different for each bucket.

The potential well $U(\phi)$ is

$$U(\phi) = \frac{qV_1}{2\pi}\Bigg\{\cos\phi - \cos\phi_\mathrm{s} + \frac{V_2}{V_1 n}\Big[\cos(n\phi+\Phi_2) - \cos(n\phi_\mathrm{s}+\Phi_2)\Big] + (\phi-\phi_\mathrm{s})\Big[\sin\phi_\mathrm{s} + \frac{V_2}{V_1}\sin(n\phi_\mathrm{s}+\Phi_2)\Big]\Bigg\}. \tag{2.41}$$

Similar to Eq. (2.33) the second order equation of motion is

$$\frac{d^2\phi}{dt^2} - \frac{h\eta\omega_0^2 qV_1}{2\pi\beta^2 E_0}\left\{\sin\phi - \sin\phi_\mathrm{s} + \frac{V_2}{V_1}\Big[\sin(n\phi+\Phi_2) - \sin(n\phi_\mathrm{s}+\Phi_2)\Big]\right\} = 0. \tag{2.42}$$

Considering now particles very close to the vicinity of the synchronous phase ϕ_s ($\Delta\phi \ll 1$) the bracket in the formula above can be replaced by

$$\left[\cos\phi_\mathrm{s} + \frac{nV_2}{V_1}\cos(n\phi_\mathrm{s}+\Phi_2)\right]\Delta\phi. \tag{2.43}$$

Thus, Eq. (2.42) is simplified to

$$\frac{d^2(\Delta\phi)}{dt^2} + \frac{\omega_{\mathrm{s}0}^2}{\cos\phi_\mathrm{s}}\left[\cos\phi_\mathrm{s} + \frac{nV_2}{V_1}\cos(n\phi_\mathrm{s}+\Phi_2)\right]\Delta\phi = 0, \tag{2.44}$$

where the frequency of the single RF case $\omega_{\mathrm{s}0}$ defined by Eq. (2.36) was introduced. Therefore, these particles perform harmonic oscillations around the phase ϕ_s with angular synchrotron frequency given by the following expression

$$\omega_\mathrm{s} = \omega_{\mathrm{s}0}\sqrt{1 + \frac{nV_2}{V_1}\frac{\cos(n\phi_\mathrm{s}+\Phi_2)}{\cos\phi_\mathrm{s}}}, \tag{2.45}$$

provided again that the condition (2.37) is valid.

Different operating modes of the double RF system are defined by the phase Φ_2 and for a non-accelerating bucket they are named according to the consequent effect they have on the bunch length (for $n = 2$). Above transition (the case considered in this thesis) and for an even n, the bunch becomes shorter for $\Phi_2 = \pi$ and thus one has the bunch-shortening mode (BSM). In contrast, for $\Phi_2 = 0$ we have the bunch-lengthening mode (BLM). The opposite is true for an odd value of n or in the case below the transition energy. The BLM is used much more often in accelerators since it is attractive for many reasons. For the same voltage and harmonic ratios the BLM gives larger synchrotron frequency spread. In addition, it provides larger bucket area as well as reduced peak line density and therefore reduced space charge effects.

For the cases of BSM and BLM with $n = 2$ and $V_2/V_1 = 0.5$ above transition the total RF voltage V_t, the potential energy $U(\phi)$ and the bucket shape (no acceleration) are presented in Fig. 2.3. The single RF case is also shown for comparison. One can see that in the BLM the potential well becomes flat in the center and for the same emittance it leads to a larger bunch length compared to the single RF case. The opposite is true in the BSM.

The case with $V_2/V_1 > 1/n$ is shown in Fig. 2.4. In the BLM the origin of phase-space becomes an unstable fixed point and two sub-buckets are created in which particles circulate around new synchronous phases. In the BSM the bunch is still focused in the center of the bucket but the available stable area has dramatically decreased.

Analytical treatment of the beam dynamics in a double RF system in the BLM with a harmonic ratio of two can be found in [50–52]. However, due to the complicated form of the potential well, a fully analytical treatment for arbitrary parameters $(\Phi_2, V_2/V_1)$ is in general difficult and thus numerical methods are used instead. For this reason the analytical examples below are usually presented for the single RF case.

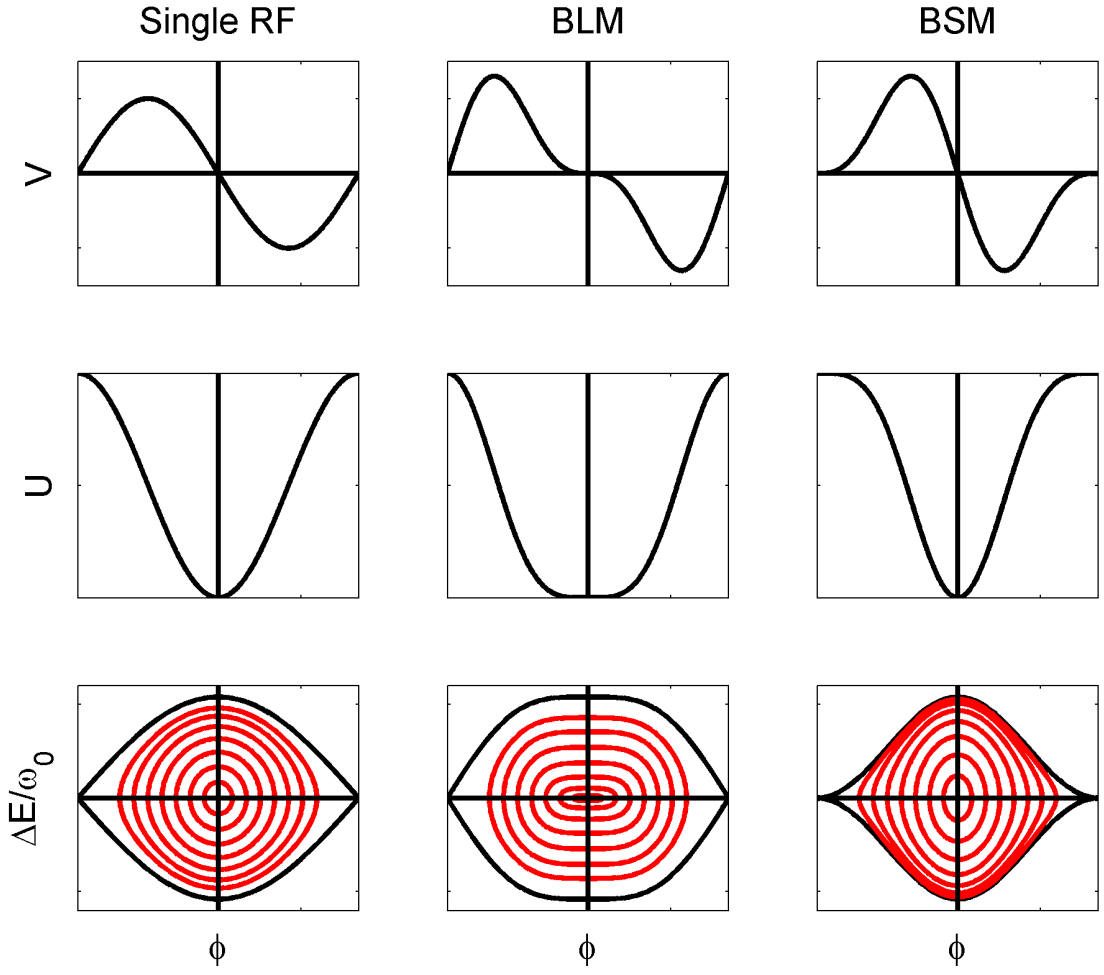

Figure 2.3: RF voltage V_{rf} (top), the potential energy $U(\phi)$ (middle) and the bucket shape (bottom) for the cases of single RF (left), BLM (middle) and BSM (right) with $n = 2$ and $V_2/V_1 = 0.5$ above transition for a stationary bucket. The red curves inside the buckets show different phase-space trajectories of constant energy that the particles follow.

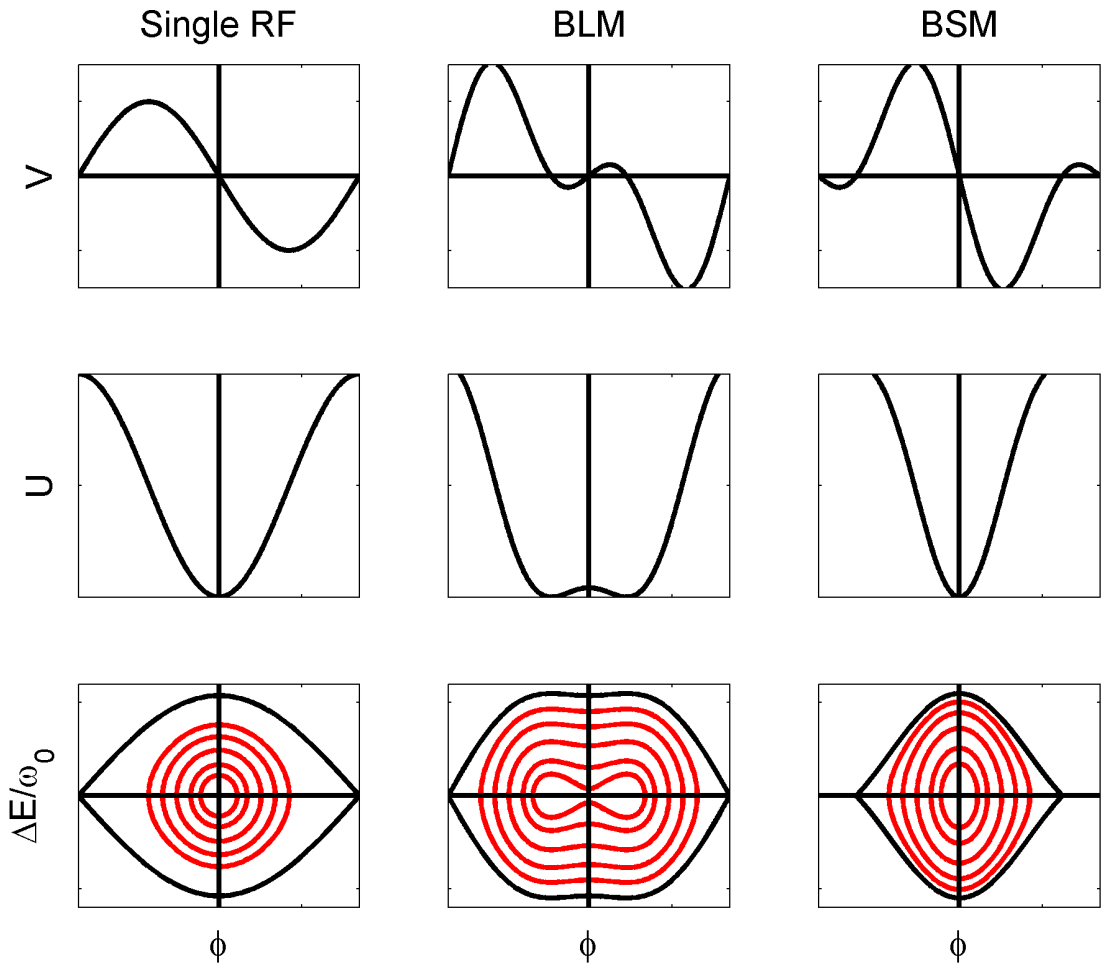

Figure 2.4: RF voltage V_{rf} (top), the potential energy $U(\phi)$ (middle) and the bucket shape (bottom) for the cases of single RF (left), BLM (middle) and BSM (rigth) with $n = 2$ and $V_2/V_1 = 0.75$ above transition for a stationary bucket. The red curves inside the buckets show different phase-space trajectories of constant energy that the particles follow.

2.1.6 RF Bucket parameters

The phase-space area enclosed by particle trajectory is

$$A = \oint \left(\frac{\Delta E}{\omega_0} \right) d\phi. \tag{2.46}$$

It was shown before that$(\phi, \Delta E/\omega_0)$ are canonical conjugate variables, meaning that this integral is the action and thus a constant of motion (Poincare invariant) [47]. The units of an area element are (energy $\times$ time). Normally in accelerators, energy is measured in (eV) and so the resulting phase-space area is in (eVs).

The phase-space area enclosed by the separatrix is called bucket area and the maximum energy deviation of the separatrix is called bucket height. These parameters have special significance since they represent the longitudinal acceptance of the machine.

The value of the Hamiltonian which corresponds to the separtrix can be calculated by taking into account that one limit of the bucket is a local maximum of the potential. Note that a local maximum of the potential appears as an unstable fixed point in the longitudinal phase-space, while local minimum gives a stable fixed point which corresponds to the center of the bucket. Therefore, from the equations of Hamilton one has that both for the stable and unstable fixed points $\Delta E/\omega_0 = 0$.

For a single RF system the separatrix can be calculated analytically. Since the local maximum of the potential is at the point $(\pi - \phi_\mathrm{s}, 0)$ one has

$$H_\mathrm{sep} = U(\pi - \phi_\mathrm{s}) = \frac{qV_0}{2\pi} \left[-2\cos\phi_\mathrm{s} + (\pi - 2\phi_\mathrm{s}) \sin\phi_\mathrm{s} \right]. \tag{2.47}$$

The phase-space trajectory is then:

$$H_\mathrm{sep} = \frac{h\eta\omega_0^2}{\beta^2 E_0} \frac{1}{2} \left(\frac{\Delta E}{\omega_0} \right)^2 + U(\phi) \tag{2.48}$$

or

$$\frac{\Delta E}{\omega_0}(\phi) = \sqrt{\frac{2\beta^2 E_0}{h\eta\omega_0^2} \left[H_\mathrm{sep} - U(\phi) \right]}. \tag{2.49}$$

The second point where particles are still bounded within the separatrix (denoted as ϕ_u in Fig. 2.2), for which the energy deviation should also be zero ($\Delta E/\omega_0 = 0$) has to satisfy the relation:

$$H_\mathrm{sep} = U(\phi_\mathrm{u}) = \frac{qV_0}{2\pi} \left[\cos\phi_\mathrm{u} - \cos(\phi_\mathrm{s}) + [\phi_\mathrm{u} - (\phi_\mathrm{s})] \sin\phi_\mathrm{s} \right] = U(\pi - \phi_\mathrm{s}) \tag{2.50}$$

or

$$\cos\phi_\mathrm{u} + \phi_\mathrm{u} \sin\phi_\mathrm{s} = \cos(\pi - \phi_\mathrm{s}) + (\pi - \phi_\mathrm{s}) \sin\phi_\mathrm{s}. \tag{2.51}$$

The difference $|\phi_\mathrm{u} - (\pi - \phi_\mathrm{s})|$ is called the bucket width.

The bucket height at phase ϕ_s can be evaluated from Eq. (2.49):

$$\frac{\Delta E}{\omega_0}(\phi_\mathrm{s}) = \sqrt{\frac{2\beta^2 E_0}{h\eta\omega_0^2} \left[H_\mathrm{sep} - U(\phi_\mathrm{s}) \right]} = \sqrt{\frac{2\beta^2 E_0}{h\eta\omega_0^2} \frac{qV_0}{2\pi} \left[-2\cos\phi_\mathrm{s} + (\pi - 2\phi_\mathrm{s}) \sin\phi_\mathrm{s} \right]}, \tag{2.52}$$

where Eq. (2.47) has been used and the fact that $U(\phi_s) = 0$.

Using Eq. (2.49) and the symmetry around the ϕ axis one can write for the bucket area

$$A = 2\int_{\phi_l}^{\phi_u} \sqrt{\frac{2\beta^2 E_0}{h\eta\omega_0^2}\,[H_{sep} - U(\phi)]}\,d\phi, \tag{2.53}$$

where $\phi_l = \pi - \phi_s$ and ϕ_u can be found from Eq. (2.51).

In the special case of stationary bucket ($\phi_s = 0$ or π), its area and height can be calculated analytically. Above transition, $\phi_s = \pi$ and then $\phi_l = 0$ and $\phi_u = 2\pi$. Since in this case the potential energy has the form

$$U(\phi) = \frac{qV_0}{2\pi}\,(1 + \cos\phi) \tag{2.54}$$

and $H_{sep} = 2(qV_0/2\pi)$, one has for the bucket area

$$\hat{A} = 2\int_0^{2\pi} \sqrt{\frac{2\beta^2 E_0}{h\eta\omega_0^2}\frac{qV_0}{2\pi}(1 - \cos\phi)}\,d\phi = 8\sqrt{\frac{2\beta^2 E_0 qV_0}{h\eta\omega_0^2\pi}}, \tag{2.55}$$

and for the bucket height

$$\frac{\Delta\hat{E}}{\omega_0} = \sqrt{\frac{2\beta^2 E_0 qV_0}{h\eta\omega_0^2\pi}}. \tag{2.56}$$

The symbol ($\hat{}$) is used to denote the stationary case.

2.1.7 Emittance and bunch characteristics

In the previous section all quantities were calculated to the full extend of the stable area. In practice, in order to avoid particle losses only a fraction of the stable area is usually occupied by beam, enclosed by a single particle trajectory in the phase-space. This area is called single-particle emittance. The trajectory of this particle can be derived from Eq. (2.49)

$$\frac{\Delta E}{\omega_0}\,(\phi) = \sqrt{\frac{2\beta^2 E_0}{h\eta\omega_0^2}\,[H_c - U(\phi)]}, \tag{2.57}$$

where H_{sep} was replaced by the new value of Hamiltonian $H_c = U(\phi_1)$ with ϕ_1 being a given point where the trajectory crosses the horizontal axis. The second point ϕ_2 were the orbit crosses the ϕ axis ($\Delta E/\omega_0 = 0$), fulfills

$$U(\phi_2) = U(\phi_1), \tag{2.58}$$

or equivalently for a single RF system

$$\cos\phi_2 + \phi_2 \sin\phi_s = \cos\phi_1 + \phi_1 \sin\phi_s. \tag{2.59}$$

After identifying the two turning points, the area under a given trajectory can be calculated from the integral

$$\varepsilon_\ell = 2\int_{\phi_2}^{\phi_1} \sqrt{\frac{2\beta^2 E_0}{h\eta\omega_0^2}\,[H_c - U(\phi)]}\,d\phi, \tag{2.60}$$

where the index ℓ indicates the longitudinal single particle emittance. Finally, the energy spread of the trajectory is determined by Eq. (2.57) evaluated at $\phi = \phi_s$ and considering the fact that $U(\phi_s) = 0$

$$\frac{\Delta E}{\omega_0}(\phi_s) = \sqrt{\frac{2\beta^2 E_0}{h\eta\omega_0^2} H_c}. \tag{2.61}$$

The emittance of a bunch, consisting of many particles (usually in the range of 10^9 - 10^{15} particles), is a statistical quantity and the percentage of the particles contained in a limiting contour depends strongly on their phase-space distribution. Therefore, the bunch emittance can be defined in many different ways. One of the most common is the root mean square (RMS) emittance. Another approach is to define the emittance through the single-particle emittance of a phase-space trajectory, which contains a certain percentage of the total amount of particles within the bunch (90%, 95% or 100%-full emittance).

Usually, in the SPS (and at CERN in general) the convention for the longitudinal emittance used in practice corresponds to the single particle emittance for trajectory in which $\phi_2 - \phi_1$ corresponds to the 4σ bunch length. This bunch length (or the σ) is obtained by applying a Gaussian fit to the acquired bunch profiles.

2.1.8 Synchrotron frequency distribution

As was discussed above, particles bounded within the bucket are performing oscillations around the stable phase ϕ_s. The oscillation frequency in the longitudinal phase-space is called the synchrotron frequency f_s. It has been shown, for a single RF system, that for particles close to the synchronous particle, f_s is given by Eq. (2.36), which for convenience is repeated below

$$f_{s0} = \frac{\omega_{s0}}{2\pi} = \frac{1}{2\pi}\sqrt{\frac{h\omega_0^2 \left|\eta \cos\phi_s\right| qV_0}{2\pi\beta^2 E_0}}. \tag{2.62}$$

In order to evaluate the time needed for one full synchrotron oscillation, we start from the first equation of motion

$$\frac{d\phi}{dt} = \frac{h\eta\omega_0^2}{\beta^2 E_0}\left(\frac{\Delta E}{\omega_0}\right) \tag{2.63}$$

or

$$dt = \frac{\beta^2 E_0}{h\eta\omega_0^2}\frac{1}{(\Delta E/\omega_0)} d\phi. \tag{2.64}$$

Assume now that an arbitrary particle in a single RF system follows in the phase-space a trajectory with Hamiltonian H_c

$$H_c = \frac{qV_0}{2\pi}\left[\cos\phi_1 - \cos\phi_s + (\phi_1 - \phi_s)\sin\phi_s\right], \tag{2.65}$$

where ϕ_1 is the maximum phase deviations of the trajectory. Using Eq. (2.57) the synchrotron oscillation period can be found from the following expression

$$T_s(H_c) = 2\int_{\phi_1}^{\phi_2}\left(\frac{\beta^2 E_0}{h\eta\omega_0^2}\frac{1}{(\Delta E/\omega_0)}\right) d\phi = \sqrt{\frac{2\beta^2 E_0}{h\eta\omega_0^2}}\int_{\phi_1}^{\phi_2}\left(H_c - U(\phi)\right)^{-1/2} d\phi, \tag{2.66}$$

with ϕ_2 evaluated through the potential well function $U(\phi)$, so that $U(\phi_2) = H_c$. Substituting H_c and $U(\phi)$ and using also the definition of ω_{s0} (2.62) one has

$$T_s(H_c) = \frac{\sqrt{2|\cos\phi_s|}}{\omega_{s0}} \int_{\phi_1}^{\phi_2} [\cos\phi_1 - \cos\phi + (\phi_1 - \phi)\sin\phi_s]^{-1/2}\, d\phi. \tag{2.67}$$

In the stationary case ($\phi_s = \pi$) the synchrotron frequency period becomes:

$$T_s(\Delta\phi_1) = \frac{1}{\omega_{s0}} \int_{-\Delta\phi_1}^{\Delta\phi_1} \frac{d(\Delta\phi)}{\sqrt{\sin^2(\Delta\phi_1/2) - \sin^2(\Delta\phi/2)}}, \tag{2.68}$$

where the Hamiltonian of the trajectory has been replaced by the maximum phase deviation ($\Delta\phi_1 = \phi_1 - \phi_s$). The fact that in this case the trajectory is symmetric around ϕ_s is also taken into account in the integration limits. Changing the integration variable from $\Delta\phi$ to θ via the substitution $\sin(\Delta\phi/2) = \sin(\Delta\phi_1/2)\sin\theta$, it can be shown that

$$T_s(\Delta\phi_1) = \frac{4K(\sin(\Delta\phi_1/2))}{\omega_{s0}}, \tag{2.69}$$

where

$$K(x) = \int_0^{\pi} \frac{d\theta}{\sqrt{1 - x^2\sin^2\theta}}, \tag{2.70}$$

is the complete elliptic integral of the first kind. Therefore, the angular synchrotron frequency $\omega_s(\Delta\phi_1)$ of the particle on this phase-space trajectory is given by

$$\omega_s(\Delta\phi_1) = \frac{\pi\omega_{s0}}{2K(\sin(\Delta\phi_1/2))}. \tag{2.71}$$

In the small amplitude approximation, using the power series expansion of $K(x)$

$$K(x) = \frac{\pi}{2}\left[1 + \left(\frac{1}{2}\right)^2 x^2 + \ldots\right], \tag{2.72}$$

the angular synchrotron frequency as a function of the maximum phase deviation can be approximated by

$$\omega_s(\Delta\phi_1) = \omega_{s0}(1 - \frac{\Delta\phi_1^2}{16}). \tag{2.73}$$

The synchrotron frequency as a function of the phase deviation for the case of a stationary bucket is shown in Fig. 2.5. The approximated formula is also presented for comparison. Note that the synchrotron frequency tends to zero when the particles approach the separatrix, since there the focusing force becomes smaller.

As is shown in Fig. 2.5, there is a spread in the synchrotron frequencies among the particles in the bunch, which is important for the Landau damping of the collective instabilities (see Section 2.6). Depending on the bunch emittance, the synchrotron frequency spread of the particles may vary a lot. Therefore, in the case of a large bunch (substantial fraction of the bucket area) that is not matched to the bucket (for example the bunch is injected into the bucket from another ring), this difference in frequencies leads to the so-called beam filamentation. This process causes the mismatched bunch distribution to evolve into spirals, diluting the phase-space

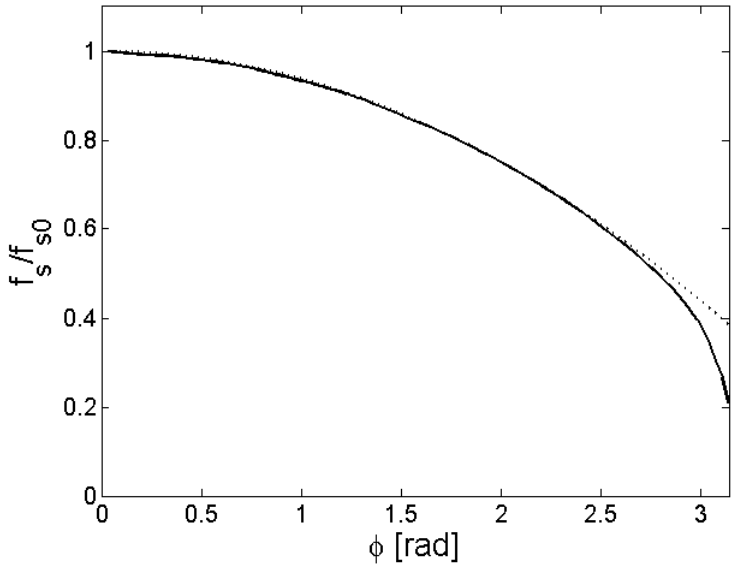

Figure 2.5: Synchrotron frequency versus the RF phase in the case of a single RF system and a stationary bucket. The exact curve is plotted with a solid line, while the approximated one with a dotted line.

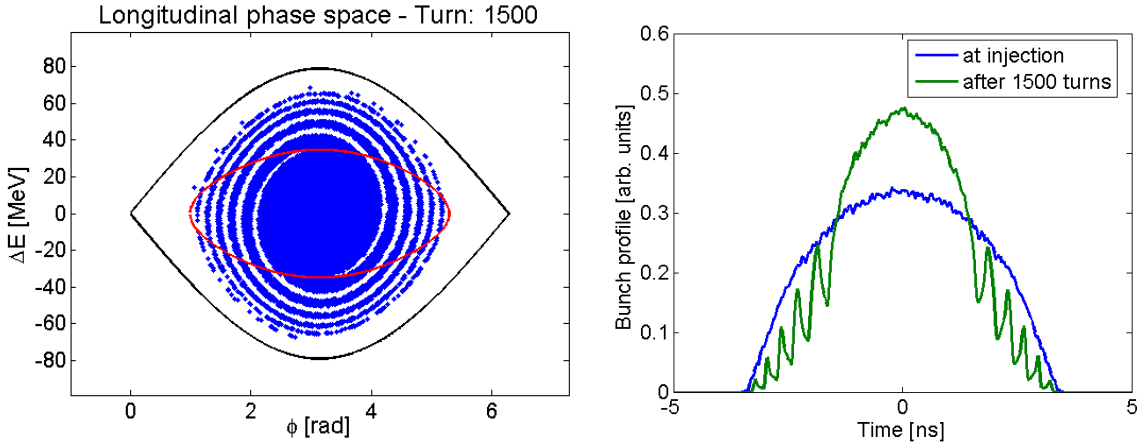

Figure 2.6: Simulated particle distribution in the longitudinal phase space (left) and its line density (right) after 1500 revolution periods (≈11 synchrotron periods). The fact that the injected distribution (red trajectory on the left plot), was not matched to the RF bucket led to strong beam filamentations. No intensity effects are included. Simulations carried out by a beam dynamics code written in Matlab (see next Chapter).

density of the beam. An example of a mismatched bunch injection and the subsequent beam filamentation is shown in Fig. 2.6.

The synchrotron frequency spread can be significantly increased by using a double RF system. Analytical calculations of the synchrotron frequency distribution in BLM and for harmonic ratio

$n = 2$ can be found in [50–52]. For example, in the case of a stationary bucket with $V_2/V_1 = 1/2$, one can find in [51]

$$f_s(r) = \frac{\pi\omega_{s0}}{K(m_2)}\sqrt{r/2}, \tag{2.74}$$

where $r = \sqrt{H_c/2}$ and H_c in this case can be obtained from Eq. (2.41) by $H_c = U(\phi_1)$. The parameter m_2 of the elliptic integral is $m_2 = (r+1)/2$.

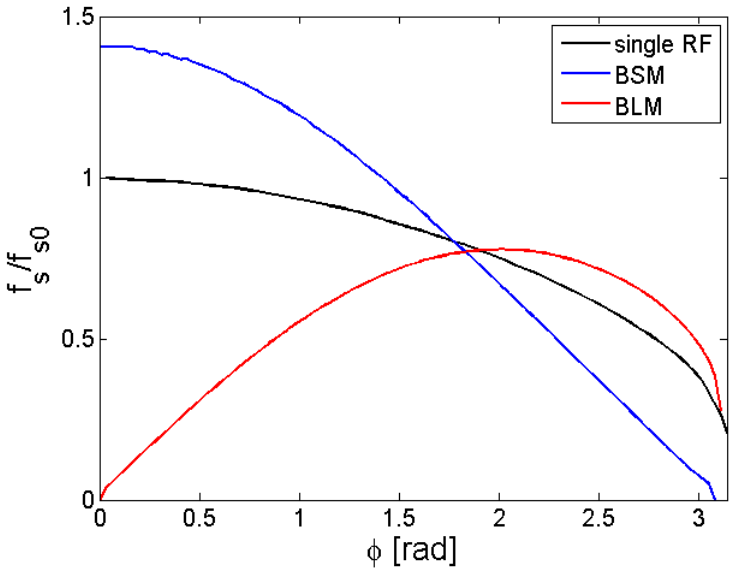

Figure 2.7: Synchrotron frequency versus the RF phase angle in the cases of BSM (black), BLM (red) and single RF system (blue). Note the increase of the frequency spread for the double RF system (in both modes). A stationary bucket is considered.

The increase of the synchrotron frequency spread in a double RF system with respect to a single harmonic can be seen in Fig. 2.7 for the case of the RF voltage and harmonic ratios $V_2/V_1 = 0.5$ and $n = 2$, respectively. In the BLM the spread on the frequencies of the beam is maximum for a $\phi \approx 2$. For larger ϕ the region where the derivative of f_s is zero appears. For long enough bunches, this can lead to a decrease of the loss of Landau damping threshold (see next Chapter).

2.1.9 Action-angle variables

The synchrotron frequency distribution inside the bunch can be also calculated by making use of the so-called action-angle variables, meaning that the Hamiltonian of the motion is transformed using a new set of canonical coordinates (ψ, J). In fact, this is a common approach when one is interested in oscillatory motion characterized by an amplitude or a phase [47].

The action variable J is defined as

$$J = \frac{1}{2\pi}\oint\left(\frac{\Delta E}{\omega_0}\right)d\phi \tag{2.75}$$

gives the phase-space area enclosed by a particle trajectory divided by 2π, i.e. comparing with Eq. (2.46)

$$J = \frac{A}{2\pi}. \tag{2.76}$$

Therefore, for a conservative system (as the one discussed here), J is a constant of motion [47]. From the Hamilton equation

$$\frac{\partial H(\psi, J)}{\partial \psi} = -\frac{dJ}{dt} = 0, \tag{2.77}$$

one can see that the Hamiltonian depends only on action, i.e. $H(\psi, J) = H(J)$.

The angle variable ψ can be obtained from the second Hamilton equation for the new set of variables

$$\frac{\partial H(J)}{\partial J} = \frac{d\psi}{dt} = \omega_s(J), \tag{2.78}$$

where $\omega_s(J)$ is the synchrotron frequency distribution of particles with action J.

2.2 Wake fields and impedances

So far it was assumed that the motion of the particles is determined by the external voltage applied by the RF cavities, and no interaction of the beam with its environment was considered. However, the beam consists of charged particles which interact with the surrounding equipment (RF cavities, injection and extraction kickers, various beam pipes, beam instrumentation etc.) generating electromagnetic fields [18]. These fields act back on the beam perturbing the particle motion. In the following, we assume that the beam is moving with the speed of light (this is practically the case for the high-energy proton beams in the SPS studied in this thesis) and therefore causality dictates that there is no electromagnetic field in front of it. That is why also these fields are known as wake fields [18].

Let us consider a particle with charge q moving with constant velocity $v = \beta c$ inside the ring. When this particle comes across a discontinuity (for example an RF cavity) or if the wall of the beam pipe is not perfectly conducting, an electromagnetic field is left behind. If $E_z(z, t)$ is the longitudinal component of the electric field, a second (witness) particle, at a distance Δz behind the source particle, which is traveling with the same speed (see Fig. 2.8), will feel this field.

The induced voltage per unit charge seen by the trailing particle is defined as wake function (see for example [1]) and is given by

$$W(\Delta z) = \frac{1}{q}\int E_z(z + \Delta z, t)dz, \tag{2.79}$$

where the integration is taken over the length of the corresponding ring element.

Applying a Fourier transform over the variable $\tau = \Delta z/(\beta c)$ one can get the longitudinal coupling impedance (in Ohms) [18]

$$Z(\omega) = \frac{1}{2\pi}\int W(\tau)e^{i\omega\tau}d\tau. \tag{2.80}$$

It is a complex, Hermitian quantity with $\mathrm{Re}Z(\omega)$ and $\mathrm{Im}Z(\omega)$ being an even and odd function of ω, respectively. Thus, the interaction of the beam with its surroundings can be described

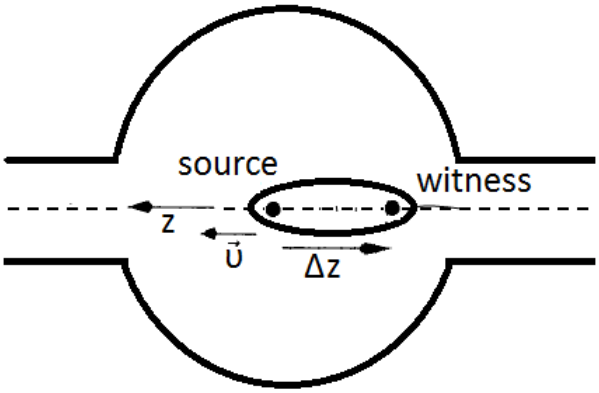

Figure 2.8: Schematic drawing of a witness particle at a distance Δz behind some source particle in a beam. Both particles are traveling along the direction z with velocity $\vec{v}$.

equivalently either through the wake functions (time domain) or the impedances (frequency domain). Depending on the problem, one or the other approach might be preferable.

For a bunch with a particle distribution in the phase-space $F(\phi, \Delta E/\omega_0)$, the line density $\lambda(\phi)$ can be defined as

$$\lambda(\phi) = \int_{-\infty}^{\infty} F(\phi, \Delta E/\omega_0) d\Big(\Delta E/\omega_0\Big). \tag{2.81}$$

Using the normalization

$$\int_{-\pi}^{\pi} \lambda(\phi) d\phi = 1, \tag{2.82}$$

the voltage induced by the bunch is given by [2]

$$V_{\mathrm{ind}}(\tau) = Nq \int_{-\infty}^{\tau} \lambda(\tau^{'}) W(\tau - \tau^{'}) d\tau^{'} \tag{2.83}$$

or in frequency domain

$$V_{\mathrm{ind}}(\omega) = Nq\lambda(\omega) Z(\omega), \tag{2.84}$$

where $\lambda(\omega)$ is the Fourier transform of $\lambda(\tau)$. Note that above the phase variable ϕ was replaced by the time variable τ.

The wake fields can be categorized as short-range (single-bunch effect) or long-range (multi-bunch effect) depending on the duration of their oscillations inside the different machine elements after the bunch passage. Local interactions (or short-range) are caused mainly by the space charge or the inductive wall impedance [2]. All particles of the beam have the same charge, resulting in a repulsive force between them (space charge). In the ultra-relativistic case (as the case studied in this thesis), space charge practically does not affect the bunch motion since the electric field generated by each particle is perpendicular to their motion [18]. The influence of the beam pipe walls on the beam behavior has a similar but opposite effect as the space charge. In most accelerators, the walls have inductive impedance at low and medium frequencies and the space charge acts like a capacitive impedance. Thus, the effects of space charge and inductive impedance on the bunch can be partly or completely compensated. However, the effect of the

inductive impedance does not vanish at high energies. It can be shown for a beam with radius α circulating in a round beam pipe of radius b that the normalized space charge and inductive wall impedance $Z(\omega)/n$, with $n = \omega/\omega_0$ is given by (see for example [2])

$$\frac{Z(\omega)}{n} = i\left(\frac{g_0 Z_0}{2\beta\gamma^2} - \omega_0 L\right), \tag{2.85}$$

where $g_0 = 1 + 2\ln b/\alpha$, Z_0 is the free space impedance and L is the wall inductance. Therefore, in this approximation the value of $Z(\omega)/n$ is independent of frequency and is purely imaginary. In practice, $Z(\omega)/n$ remains almost constant up to the so-called cut-off frequencies [18]. Note the $1/\gamma^2$ dependance of the space charge term meaning that at high energies its contribution can become negligible.

Long-range wakes can be produced by the RF cavities or other cavity-like objects. The total duration of the excited fields depends on the characteristics of the specific cavity. It can last long enough to affect the trailing bunches or even the same bunch in the next revolution period. The coupling impedance of a resonator can be written in the form

$$Z(\omega) = \frac{R_{\mathrm{sh}}}{1 + iQ\left(\frac{\omega}{\omega_r} - \frac{\omega_r}{\omega}\right)}, \tag{2.86}$$

where R_{sh}, ω_r and Q are the shunt impedance, the resonant frequency and the quality factor, respectively. Depending on Q this impedance can be either narrow-band (high Q, long-range wake) or broad-band (low Q, short-range wake). Applying the inverse Fourier transform one can show [18] that the wake field of a resonator is

$$W(\tau) \propto W_0 \exp^{-\omega_r \tau/2Q}, \tag{2.87}$$

and thus decays exponentially in time with a time constant $2Q/\omega_r$. Therefore, for bunches spaced by 25 ns (as in the LHC beam) and a resonator at frequency $f_r = \omega_r/(2\pi) = 1$ GHz, if $Q > \pi$ the induced field of one bunch will affect the motion of the next bunch. Typically, for the main resonators included in the SPS impedance model, Q is between 5 and 300 within a frequency range of (0.2 - 1.6) GHz [53]. This is the reason why in beam measurements in the SPS, a coupling between roughly 10 bunches in the batch is observed [41].

2.3 Vlasov equation

In the conservative deterministic system of the particles in the longitudinal phase-space, described by the canonical conjugate variables $(\phi, \Delta E/\omega_0)$, the particle trajectories are completely determined by their initial conditions. That means that two particles starting from the same point will follow the same phase-space trajectories. For convenience, below we denote the phase-space variable $\Delta E/\omega_0$ by ϵ.

Due to the very large number of particles $(10^{10} - 10^{15})$ in the accelerator, we are more interested in the evolution of the phase-space distribution function $F(\phi, \epsilon)$ and not in single particle trajectories. The number of particles occupying some small phase-space area is $dN = F(\phi, \epsilon) d\phi d\epsilon$ and therefore the total number of particles in the bunch is given by the integral

$$N = \int\int F(\phi, \epsilon) d\phi d\epsilon. \tag{2.88}$$

The time evolution of the distribution function $F(\phi, \epsilon)$ is described by the Liouville's theorem [54]. It asserts that the phase-space distribution function is constant along the trajectories of the system and can be expressed by the equation

$$\frac{dF(\phi, \epsilon)}{dt} = 0, \tag{2.89}$$

or taking into account the dependance on ϕ and ϵ

$$\frac{\partial F}{\partial t} + \frac{\partial F}{\partial \phi}\dot{\phi} + \frac{\partial F}{\partial \epsilon}\dot{\epsilon} = 0. \tag{2.90}$$

This expression is known as the Vlasov equation [54].

Using the Hamilton equations of motion (2.30) and (2.31) we can write Eq. (2.90) in the form

$$\frac{\partial F}{\partial t} + [F, H] = 0, \tag{2.91}$$

where the second part on the right hand side is the Poisson bracket [47] and H is the Hamiltonian given by Eq. (2.29).

In the case of electron beams, however, the contribution of the synchrotron radiation to damping and diffusion is much stronger and one needs to use the Fokker-Planck equation instead [55].

2.4 Potential well distortion

The stationary state of the particle distribution and the way it is affected by interaction with the machine impedance, are important for analysis of beam stability. Since the stationary distribution function does not depend explicitly on time, we get from the Vlasov equation (2.91)

$$\frac{\partial F}{\partial t} = 0 \Rightarrow [F, H] = 0, \tag{2.92}$$

which means that in this case the distribution function is a function of the Hamiltonian only, $F = F(H)$.

At low intensities, when $V_{\mathrm{ind}} \ll V_{\mathrm{rf}}$ the potential well is mainly defined by the external RF voltage (see Fig. 2.2). As the intensity increases, the effect of the wake fields becomes stronger, leading to the distortion of the RF potential well. To illustrate this effect we will consider again the case of a single RF system and a bunch with a length that is short compared to the RF wavelength. Then the equation of motion for zero intensity is given by Eq. (2.35)

$$\frac{d^2\phi}{dt^2} + \omega_{\mathrm{s0}}^2 \phi = 0, \tag{2.93}$$

where ω_{s0} can be found from Eq. (2.36). Note that for convenience, in the equation above ϕ was used instead of $\Delta\phi$ compared to Eq. (2.35).

Introducing now intensity effects through the wake function $W(\phi)$, and assuming a short range wake, the previous equation is modified to

$$\frac{d^2\phi}{dt^2} + \omega_{\mathrm{s0}}^2 \phi = \frac{\omega_{\mathrm{s0}}^2 V_{\mathrm{ind}}(\phi)}{V_{\mathrm{rf}} \cos\phi_{\mathrm{s}}}, \tag{2.94}$$

where $V_{\rm ind}$ is given by Eq. (2.83) with $\phi = \omega_{\rm rf}\tau$

$$V_{\rm ind}(\phi) = Nq\int_{-\infty}^{\phi}\lambda(\varphi)W(\phi-\varphi)d\varphi. \tag{2.95}$$

Here $\lambda(\phi)$ is the particle line density normalized according to Eq. (2.82). Expanding $V_{\rm ind}$ into a Taylor series up to the first order in ϕ (small angle approximation) we have

$$V_{\rm ind}(\phi) = V_{\rm ind}(0) + V_{\rm ind}^{'}(0)\phi + \ldots, \tag{2.96}$$

where

$$V_{\rm ind}(0) = Nq\int_{-\infty}^{0}\lambda(\varphi)W(-\varphi)d\varphi \tag{2.97}$$

and

$$V_{\rm ind}^{'}(0) = Nq\lambda(0)W(0) + Nq\int_{-\infty}^{0}\lambda(\varphi)W^{'}(-\varphi)d\varphi. \tag{2.98}$$

Thus in this approximation Eq. (2.94) becomes [4]

$$\frac{d^2\phi}{dt^2} + \omega_{\rm s0}^2\phi = \frac{\omega_{\rm s0}^2}{V_{\rm rf}\cos\phi_{\rm s}}\left(V_{\rm ind}(0) + V_{\rm ind}^{'}(0)\phi\right) \tag{2.99}$$

.

The first, constant term on the right hand side of Eq. (2.99) shifts the synchronous phase by

$$\Delta\phi_{\rm s} = \frac{Nq}{V_{\rm rf}\cos\phi_{\rm s}}\int_{-\infty}^{0}\lambda(\varphi)W(-\varphi)d\varphi = \frac{Nq}{V_{\rm rf}\cos\phi_{\rm s}}\frac{1}{2\pi}\int_{-\infty}^{\infty}\lambda(\omega)Z(\omega)d\omega. \tag{2.100}$$

Since $\lambda(\omega)$ is an even function, ${\rm Im}Z(\omega)$ (odd function) does not contribute to the later integral and only the real part of the impedance (even function) is responsible for the phase shift

$$\Delta\phi_{\rm s} = \frac{Nq}{2\pi V_{\rm rf}\cos\phi_{\rm s}}\int_{-\infty}^{\infty}\lambda(\omega){\rm Re}Z(\omega)d\omega. \tag{2.101}$$

The second term on the right hand side of Eq. (2.99) will cause a shift in the synchrotron frequency given by

$$\frac{\omega_{\rm s}^2-\omega_{\rm s0}^2}{\omega_{\rm s0}^2} = \frac{Nq}{V_{\rm rf}\cos\phi_{\rm s}}\int_{-\infty}^{0}\lambda(\varphi)W^{'}(-\varphi)d\varphi = -\frac{iNq}{V_{\rm rf}\cos\phi_{\rm s}}\frac{1}{2\pi}\int_{-\infty}^{\infty}\omega\lambda(\omega)Z(\omega)d\omega. \tag{2.102}$$

In this case $\omega\lambda(\omega)$ is an odd function and therefore only the imaginary part of the impedance will contribute to the integral and consequently to the synchrotron frequency shift:

$$\frac{\omega_{\rm s}^2-\omega_{\rm s0}^2}{\omega_{\rm s0}^2} = \frac{Nq}{V_{\rm rf}\cos\phi_{\rm s}}\frac{1}{2\pi}\int_{-\infty}^{\infty}\omega\lambda(\omega){\rm Im}Z(\omega)d\omega. \tag{2.103}$$

Note that the last equation gives the synchrotron frequency shift of the particles inside the bunch, oscillating with small amplitudes around the synchronous particle. However, this is not the case for the rest of the particles, where the effect of the impedance is in general

different, leading to a change of the synchrotron frequency distribution inside the bunch (see next Chapters).

An analytical solution of Eq. (2.103) can be obtained when the wake function has the special form [2]

$$W(\phi) = S\delta^{'}(\phi). \tag{2.104}$$

This wake function can be produced by a purely imaginary impedance with constant $\mathrm{Im}Z/n$, and S being

$$S = h^2\omega_0 \frac{i(i\mathrm{Im}Z)}{n}, \tag{2.105}$$

Inserting this wake into Eq. (2.95) we have for the induced voltage

$$V_{\mathrm{ind}}(\phi) = NqS\lambda^{'}(\phi). \tag{2.106}$$

Assuming now a so-called parabolic line density (often a good approximation for protons) [4] with $\hat{\phi}_0$ denoting the half bunch length (in rad)

$$\lambda(\phi) = \frac{3}{4\hat{\phi}_0}\left[1 - \left(\frac{\phi}{\hat{\phi}_0}\right)^2\right] \tag{2.107}$$

and following the same steps as before, the synchrotron frequency shift becomes

$$\frac{\omega_{\mathrm{s}}^2 - \omega_{\mathrm{s0}}^2}{\omega_{\mathrm{s0}}^2} = \frac{V_{\mathrm{ind}}^{'}(0)}{V_{\mathrm{rf}}\cos\phi_{\mathrm{s}}} = -\frac{3Nq}{2V_{\mathrm{rf}}\cos\phi_{\mathrm{s}}}\frac{S}{(\hat{\phi}_0)^3} \tag{2.108}$$

or in terms of the impedance, using Eq. (2.105),

$$\frac{\omega_{\mathrm{s}}^2 - \omega_{\mathrm{s0}}^2}{\omega_{\mathrm{s0}}^2} = \frac{3Nq}{2V_{\mathrm{rf}}\cos\phi_{\mathrm{s}}}\frac{h^2\omega_0}{(\hat{\phi}_0)^3}\frac{\mathrm{Im}Z}{n}. \tag{2.109}$$

From the latter equation we can see that above transition energy, where $\cos\phi_{\mathrm{s}} < 0$ the synchrotron frequency is reduced if the impedance is inductive ($\mathrm{Im}Z/n > 0$) and increased if it is capacitive ($\mathrm{Im}Z/n < 0$). The reverse applies below transition. Similar dependance of the synchrotron frequency spread on the beam and machine parameters can be obtained for other distributions but different in absolute values [4].

The same is also true for the effective voltage that the particles see

$$V_{\mathrm{eff}} = V_{\mathrm{rf}} + \frac{3Nq}{2\cos\phi_{\mathrm{s}}}\frac{h^2\omega_0}{(\hat{\phi}_0)^3}\frac{\mathrm{Im}Z}{n}. \tag{2.110}$$

Above transition and for inductive impedance the effective voltage is smaller than the RF voltage with a consequent reduction of the bucket height. In addition, considering a proton beam with constant emittance, one would expect that the corresponding bunch length will be increased. It can be shown [4] that due to the effect of potential well distortion the new bunch length $\hat{\phi}$ satisfies the relation

$$\left(\frac{\hat{\phi}}{\hat{\phi}_0}\right)^2 = \frac{\omega_{\mathrm{s0}}}{\omega_{\mathrm{s}}}\sqrt{\frac{\cos\phi_{\mathrm{s}}}{\cos(\phi_{\mathrm{s}} + \Delta\phi_{\mathrm{s}})}}. \tag{2.111}$$

The last formula can be used to distinguish in measurements between the bunch lengthening due to the potential well distortion from the one resulting from instability [4]. In particular, usually one observes that by increasing the bunch current the bunch length is increasing with a certain slope given by Eq. (2.111), until some threshold current, where the slope becomes stepper. This point is considered to be the instability threshold.

2.5 Perturbation and coherent modes of oscillations

In addition to the potential well distortion, the induced voltage can force all or some of the particles in the bunch to execute also a collective motion starting from a small perturbation. This perturbation, under certain circumstances, can grow exponentially leading to beam instability. Initially, the particle distribution can be presented as a sum of the stationary distribution $F_0(H)$ and a small perturbation $F_1(\phi, \epsilon, t)$

$$F(\phi, \epsilon, t) = F_0(H) + F_1(\phi, \epsilon, t). \tag{2.112}$$

This perturbation will introduce an extra term in the voltage

$$V(\phi) = V_0(\phi) + V^1_{\text{ind}}(\phi, t), \tag{2.113}$$

where $V_0 = V_{\text{ext}} + V^0_{\text{ind}}$ is the full voltage in the stationary state and V^1_{ind} is the additional voltage induced by $F_1(\phi, \epsilon, t)$

$$V^1_{\text{ind}}(\phi, t) = Nq \int_{-\infty}^{\infty} \lambda_1(\phi^{'}, t) W(\phi - \phi^{'}) d\phi^{'} = Nq \int_{-\infty}^{\infty} \int_{-\infty}^{\infty} F_1(\phi^{'}, \epsilon^{'}, t) W(\phi - \phi^{'}) d\phi^{'} d\epsilon^{'}, \tag{2.114}$$

where $\lambda_1(\phi, t)$ is the line density perturbation given by

$$\lambda_1(\phi, t) = \int_{-\infty}^{\infty} F_1(\phi, \epsilon, t) d\epsilon.$$

The second equation of motion (2.26) becomes

$$\dot{\epsilon} = \frac{q}{2\pi} \left[V_0(\phi) + V^1_{\text{ind}}(\phi, t) \right]. \tag{2.115}$$

For the stationary case, the Vlasov equation (2.91) can be written in terms of the phase-space variables

$$\frac{\partial F_0}{\partial \phi} \dot{\phi} + \frac{q}{2\pi} V_0(\phi) \frac{\partial F_0}{\partial \epsilon} = 0. \tag{2.116}$$

Introducing Eqs. (2.112) and (2.115) into the Vlasov equation (2.90) and keeping only linear terms in the perturbation (quadratic terms in F_1 and also products of $F_1 V^1_{\text{ind}}$ are neglected), we end-up with the linearized Vlasov equation [7]

$$\frac{\partial F_1}{\partial t} + \frac{\partial F_1}{\partial \phi} \dot{\phi} + \frac{q}{2\pi} V_0 \frac{\partial F_1}{\partial \epsilon} + \frac{q}{2\pi} V^1_{\text{ind}}(\phi, t) \frac{\partial F_0}{\partial \epsilon} = 0, \tag{2.117}$$

where Eq. (2.116) was also used.

Transforming the phase-space coordinates (ϕ, ϵ) to the action-angle (ψ, J) we find

$$\begin{aligned} \dot{\phi}\frac{\partial}{\partial\phi} + \dot{\epsilon}\frac{\partial}{\partial\epsilon} &= \left(\frac{\partial\psi}{\partial\phi}\dot{\phi} + \frac{\partial\psi}{\partial\epsilon}\dot{\epsilon}\right)\frac{\partial}{\partial\psi} + \left(\frac{\partial J}{\partial\phi}\dot{\phi} + \frac{\partial J}{\partial\epsilon}\dot{\epsilon}\right)\frac{\partial}{\partial J} \\ &= \omega_s(J)\frac{\partial}{\partial\psi}, \end{aligned} \tag{2.118}$$

where the two parenthesis in the above formula were replaced using Eqs. (2.77) and (2.78) as follows:

$$\begin{aligned} \frac{dJ}{dt} &= 0 \Leftrightarrow \frac{\partial J}{\partial\phi}\dot{\phi} + \frac{\partial J}{\partial\epsilon}\dot{\epsilon} = 0 \\ \frac{d\psi}{dt} &= \omega(J) \Leftrightarrow \frac{\partial\psi}{\partial\phi}\dot{\phi} + \frac{\partial\psi}{\partial\epsilon}\dot{\epsilon} = \omega_s(J). \end{aligned} \tag{2.119}$$

Remembering the definition of the potential energy in Eq (2.32), we have

$$\frac{\partial U^1_{\text{ind}}(\phi, t)}{\partial\phi} = -\frac{q}{2\pi}V^1_{\text{ind}}(\phi, t), \tag{2.120}$$

while

$$\frac{\partial F_0}{\partial\epsilon} = \frac{dF_0}{dH}\frac{\partial H}{\partial\epsilon} = \frac{dF_0}{dJ}\frac{dJ}{dH}\frac{\partial H}{\partial\epsilon} = \frac{dF_0}{dJ}\frac{\dot{\phi}}{\omega(J)}. \tag{2.121}$$

Combining the last two equations with Eq (2.118), the linearized Vlasov equation becomes

$$\frac{\partial F_1}{\partial t} + \omega_s(J)\frac{\partial F_1}{\partial\psi} - \frac{\partial U^1_{\text{ind}}(\phi, t)}{\partial\psi}\frac{dF_0}{dJ} = 0. \tag{2.122}$$

The solutions of this equation, for a particular stationary distribution function F_0 and wake function W, determine whether the system is stable or not.

In the case of very weak self-forces, compared to the external forces ($U^1_{\text{ind}} \ll V_{\text{rf}}$), the last term of Eq. (2.122) can be neglected. Following Sacherer [7], it can be shown that in this case the solution of the Vlasov equation has the form

$$F_1 = R_m(J)e^{im\psi}e^{-i\omega t}, \tag{2.123}$$

with $\omega = m\omega_s(J)$ and m being an integer which defines the azimuthal mode. This type of solutions tells us that the azimuthal modes m, oscillate with frequencies $m\omega_s(J)$, defined by the potential well distortion. A few azimuthal are shown in Fig. 2.9 [3]

Depending on the azimuthal number m, the modes are usually classified as dipole ($m = 1$), quadrupole ($m = 2$), sextupole ($m = 3$), etc. For example, $m = 1$ in Fig. 2.9 corresponds to the rigid-dipole mode oscillations which is usually observed when the bunch is injected with a phase error. Mode $m = 2$ corresponds to the rigid-quadrupole oscillations when there is a mismatch between the bunch shape in phase-space and the RF bucket and then the oscillations appears to be twice as fast. In general these modes can be described by $\cos m\phi$ with $2m$ nodes in the longitudinal phase-space (top row of Fig. 2.9). The projection of the phase-space distribution on the phase axis is the line density which has m nodes in the mth mode not including the ends (bottom row of Fig. 2.9).

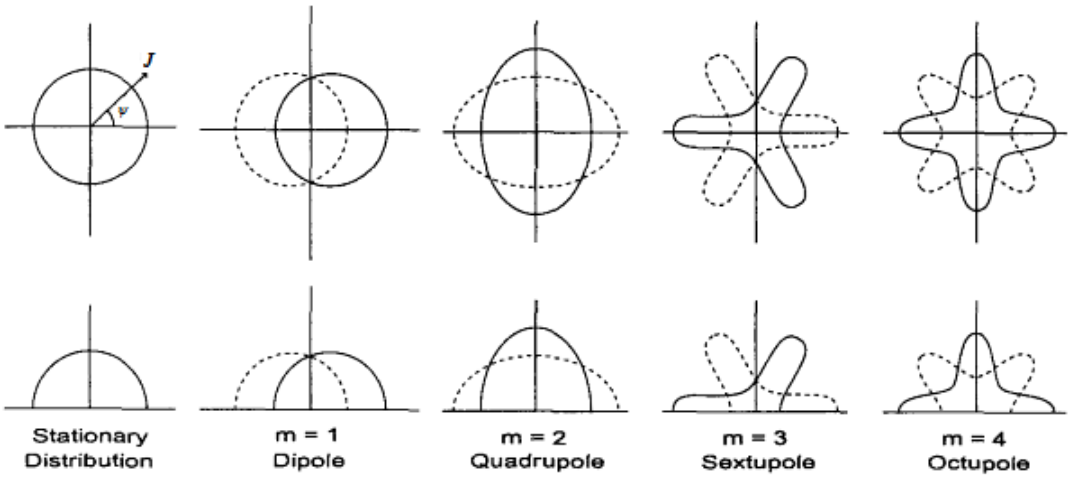

Figure 2.9: Azimuthal synchrotron modes of a bunch in the longitudinal phase-space (top) and the resulting line density (bottom) [3].

The function $R(J)$ defines the radial dependance of the solutions. In fact, there are, for example, an infinite number of dipole-type modes [7]. A non-rigid mode only appears if the central part of the initially stationary distribution (first column in Fig. 2.9) is displaced from the origin. Similarly there is an infinite number of quadrupole modes and of the higher multipole modes.

For large number of particles the last term of Eq. (2.122) should be also taken into account. The perturbed distribution can be expanded in the longitudinal phase-space as

$$F_1 = \sum_m R_m(J) e^{im\psi} e^{-i\omega t}, \tag{2.124}$$

where ω is the collective frequency to be determined. In principal ω is a complex number, and therefore, when $\mathrm{Im}\omega > 0$ the beam is unstable.

Substituting Eq. (2.124) into Eq. (2.122), multiplying both sides by $e^{-im'\psi}$ and integrating over ψ we get the following equation

$$[\omega - m\omega_s(J)]R_m(J) = -\frac{dF_0}{dJ} \sum_{m'} \int_0^\infty dJ' R_{m'}(J') g_{mm'}(J, J'), \tag{2.125}$$

where

$$g_{mm'}(J, J') = \frac{i}{2\pi} \int_0^{2\pi} d\psi \int_0^{2\pi} d\psi' \frac{\partial \phi}{\partial \psi} W(\phi - \phi') e^{im'\psi' - im\psi}. \tag{2.126}$$

In the derivation of Eq. (2.125) the following equation was used

$$\begin{aligned} \frac{\partial U^1_{\mathrm{ind}}(\phi)}{\partial \psi} &= -\int_0^\infty dJ' \int_0^{2\pi} d\psi' \frac{\partial \phi}{\partial \psi} F_1(\psi', J') W(\phi - \phi') \\ &= -\int_0^\infty dJ' \int_0^{2\pi} d\psi' \frac{\partial \phi}{\partial \psi} \sum_m{}' R_{m'}(J') e^{im'\psi'} W(\phi - \phi'). \end{aligned} \tag{2.127}$$

Finally we end up with the integral equation (2.125) [7], which is an eigen-value problem for $R_m(J)$. Given a longitudinal wake $W(\phi)$ and an unperturbed distribution $F_0(J)$, the coherent frequencies of excitation ω can be found. Unfortunately, finding analytic solutions is possible only for some particular functions $W(\phi)$ and $F_0(J)$, and becomes difficult in general case, especially with a spread in the incoherent synchrotron frequency $\omega_s(J)$.

In this thesis, solutions of the linearized Vlasov equation were found in a semi-analytical way following the approach from [12, 13], where the potential well distortion and the incoherent synchrotron frequency distribution were taken into account. We also used the approximation that the perturbation is small $\omega - m\omega_s(J) \ll \omega_s(J)$, implying that the coupling between different azimuthal modes can be neglected. This simplifies the Vlasov equation from a system of infinite equations to one involving only one azimuthal mode m.

2.6 Landau damping

Landau damping was initially formulated by Landau [8] in plasma physics, as a natural stabilization mechanism against collective instabilities. Today, this phenomenon is of common-place occurrence in the physics of charged particle beams in storage rings, in the context of beam stability against the collective modes. The first time that Landau damping was introduced in beam physics was by Neil and Sessler [56] and since then many studies (see for example [2, 9, 57]) revealed its great importance for the daily operation of the circular accelerators.

Its application in the accelerators is based on the fact that the beam particles behave as an ensemble of oscillators with (in principle) a spread in their natural frequencies. For a bunched beam in the longitudinal plane, Landau damping proceeds through the spread in synchrotron frequency. This spread is responsible of stabilizing the beam which would otherwise be unstable due to the various perturbations.

Let us assume that an ensemble of oscillators (as is the bunch) with frequency spread $\Delta\omega$ is subjected to a monochromatic excitation with frequency Ω ($f \sim e^{-i\Omega t}$) which lies within the frequency band $\Delta\omega$. The equation describing the displacement y of a single particle is given by

$$\ddot{y} + \omega^2 \dot{y} = Ae^{-i\Omega t}, \tag{2.128}$$

where the overdots represent derivatives with respect to time and A denotes the amplitude of the force. The solution of the above equation proportional to the driving force can be written as

$$y(t) = \frac{A}{\omega^2 - \Omega^2} e^{-i\Omega t}. \tag{2.129}$$

For a large number of particles the displacement of the center of mass is

$$< y(t) >= A \int_{\infty}^{\infty} d\omega \frac{\rho(\omega)}{\omega^2 - \Omega^2} e^{-i\Omega t}, \tag{2.130}$$

where the $\rho(\omega)$ is the distribution of the resonance frequencies of the particles normalized according to

$$\int_{\infty}^{\infty} \rho(\omega) d\omega = 1. \tag{2.131}$$

Following a treatment by [3] it can be shown that in the approximation when $\rho(\omega)$ in narrow around a center frequency $\overline{\omega}$, the oscillation amplitude of a component corresponding to frequency ω is

$$\text{Amplitude}(\omega) = \frac{A}{\overline{\omega}} \frac{\sin(\omega - \Omega)t/2}{\omega - \Omega}. \tag{2.132}$$

This means that all particles having frequency ω are excited at $t = 0$, increase to the maximum amplitude at $t \approx \pi/(\omega - \Omega)$ which is damped down to zero at $t = 2\pi/(\omega - \Omega)$. Thus, energy is gained but is given back to the system. For ω closer to Ω, the response amplitude rises to a larger value and the energy is given back to the system at a later time. For those particles that have exactly the frequency Ω, the amplitude grows linearly with time and the energy keeps on growing. This process of transferring energy to the few particles having frequencies very close to Ω is called Landau damping. An illustration is shown in Fig. 2.10, where the red curve in the bottom plot shows a particle having exactly the same frequency as Ω with oscillation amplitude growing linearly, while the other curves show particles with frequencies different from Ω and their oscillations are decaying with time. The decay time and maximum amplitude depend inversely on the frequency difference $\Delta\omega = \omega - \Omega$. In other words, particles with ω far away from Ω get excited, but the energy is returned to those particles having ω close to Ω, which are absorbing energy.

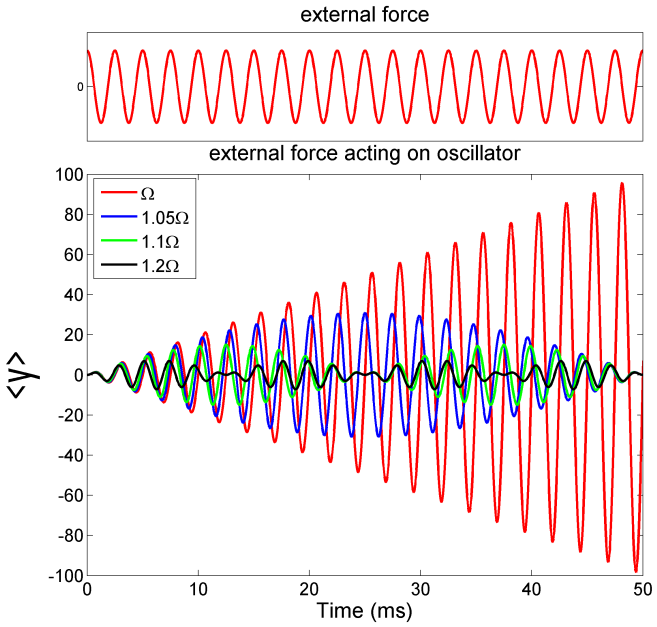

Figure 2.10: Oscillator's response to a sinusoidal driving force $f(t) = A\cos\Omega t$ (top plot). The bottom plot shows the response of oscillators with different frequencies compared to Ω.

The energy of the system of the particles on the other hand, is proportional to

$$\big[\text{Amplitude}(\omega)\big]^2 = \frac{\sin^2(\omega - \Omega)t/2}{\omega - \Omega}. \tag{2.133}$$

One can see that as time progresses the amplitude square becomes larger and larger ($\propto t^2$), while

its width shrinks ($\Delta\omega \propto 1/t$). This confirms that energy is being transferred by the particles having frequencies far away from Ω to particles having frequencies closer to Ω. Finally, as $t \to \infty$, the linear increase in the energy of the system of the particles is concentrated at those particles having exactly the same frequency as Ω. However, it can be shown that the centroid motion of the ensemble of the particles, $< y >$, will be still damped even when a few particles have very large and still growing amplitudes.

The asymptotic behavior mentioned before applies if one waits for a time longer than $1/\Delta\omega$. For $t < 1/\Delta\omega$, the beam response is confounded by transient terms. Furthermore, the resistive term is proportional to the particle distribution $\rho(\Omega)$. If the spectrum is such that there are no particles near frequency Ω to continuously absorb energy, Landau damping will cease and a beating phenomenon takes over. Since a beam consists of a finite number of particles, Landau damping will cease when t is larger than $1/\delta\omega$, where $\delta\omega$ is the frequency spacing between two nearest particles. The range of time for Landau damping to be effective is therefore

$$1/\delta\omega >> t >> 1/\Delta\omega. \tag{2.134}$$

With N particles in the beam, one might have $\delta\omega \approx \Delta\omega/N$. Taking $N = 10^{11}$ and $\Delta\omega = 10^3$ s^{-1} for example, the time is limited to the range between 1 ms and 10^8 s.

Chapter 3

Loss of Landau damping in a double RF system

In this Chapter the thresholds of the loss of Landau damping due to the presence of reactive impedance are determined in a single and double harmonic RF systems, both from calculations and particle simulations. It is shown that in the bunch lengthening mode (BLM), Landau damping is effective only below some critical value of longitudinal emittance. Above this value bunches become more unstable than even in a single RF system. A phase shift of more than 15 degrees between the two RF components is proven able to stabilize the bunch. These results can explain now observations during the p$\bar{\text{p}}$ operation of the SPS. The critical regions of the bunch size appear also in the case of bunch shortening mode (BSM) for high harmonic ratio and sufficiently large voltage ratio between the two RF systems.

3.1 Introduction

The BLM was used in the SPS during its operation as a p$\bar{\text{p}}$ collider, when a 100 MHz RF system was installed in addition to the existing 200 MHz RF system [14]. At that time, transverse space charge de-tuning effects together with microwave instability were the main bunch intensity limitations. By operating in BLM it was possible to significantly increase the bunch intensity.

The bunches were injected into the SPS with a nominal longitudinal emittance of $\varepsilon_\ell = 0.65$ eVs (2σ). However, the synchrotron frequency spread introduced by the second harmonic RF component was barely sufficient for stability and any injection errors were un-damped with bunch oscillating along the injection plateau (26 GeV/c). Furthermore, for larger emittances instability was occurring in the tails of the bunch, and the feedback loops were not able to damp it. To counteract this instability a phase shift between the 2 RF systems was introduced [15].

Previous studies of beam stability in a double RF system already pointed out that in the BLM Landau damping can be lost for particles in the region where the synchrotron frequency distribution has its maximum ($\omega_s^{'}(J) = 0$) outside the bunch center [51,58]. This region was also creating problems in the beam control of the CERN PS Booster due to the large coherent signal in a double harmonic RF system [59]. Indeed, large amplitude coherent response was measured in beam transfer function (BTF) in the BLM at frequencies corresponding to $\omega_s^{'}(J) = 0$ [60]. Recently, an analytical approach made it possible to find this threshold through the onset of a discrete Van Kampen mode (coherent mode without Landau damping) by solving numerically the linearized Vlasov equation [12, 13].

The latter method is used in this thesis, together with particle simulations for inductive impedance, to explain the observations during the p$\bar{\text{p}}$ operation. Only the dipole modes ($m = 1$) are addressed since they are expected to have the lowest threshold and no coupling between

different azimuthal modes is considered. The analysis is also expanded to the cases of the BSM and a single RF to get a better understanding of the different operating modes. Moreover, the situation of a higher harmonic ratio between the two RF systems is also considered, which in fact corresponds to the current situation in the SPS.

3.2 Method of calculations

Below the semi-analytical calculations are done in two steps. First, a steady state solution needs to be found for the specified conditions (RF voltages, emittance ε_l, intensity and impedance) and then the linearized Vlasov equation can be solved. These parts are described in more details in the following sections.

3.2.1 Steady state solution

In order to find the steady state solution, we need to deal with the potential-well distortion. As mentioned in section 2.2, the induced voltage depends on the line density $\lambda(\phi)$ and therefore a self-consistent solution needs to be found. This can be done by solving the following system of equations (see ref. [12]):

$$\begin{aligned} U(\phi) &= U_{\mathrm{rf}} + U_{\mathrm{ind}} = U_{\mathrm{rf}} - \frac{q}{2\pi}\int_{-\infty}^{\phi} d\phi^{'}\int_{-\infty}^{\phi^{'}} d\phi^{''}\lambda(\phi^{''})W(\phi^{'}-\phi^{''}) \equiv U_{\mathrm{RHS}}[\lambda], \\ J(H) &= \frac{\varepsilon_\ell}{2\pi} = \frac{A}{\pi}\int_{\phi_2}^{\phi_1}\sqrt{[H-U(\phi)]}d\phi \equiv J_{\mathrm{RHS}}[U], \\ \lambda(\phi) &= 2\int_0^{\varepsilon_1} F_0\left(J\left(H\right)\right)d\varepsilon = 2A\int_{U(\phi)}^{H_{\max}}\frac{F_0\left(J\left(H\right)\right)}{\sqrt{2\left[H-U(\phi)\right]}}dH \equiv \lambda_{\mathrm{RHS}}[J,U], \end{aligned} \tag{3.1}$$

where $A=\sqrt{2\beta^2E_0/h\eta\omega_0^2}$ and use has been made of Eqs. (2.41), (2.32), (2.83) , (2.75), (2.57) and (2.60). In the last of the above equations $H_{\max}$ corresponds to the Hamiltonian of the particles placed at the very edge of the pre-defined bunch emittance. The phase-space density as a function of action $F_0(J)$ and the wake function $W(\phi)$ are required as an input. In order to solve this system, an iteration procedure can be applied with the initial condition $U_0(\phi)=U_{\mathrm{rf}}(\phi)$:

$$\begin{aligned} U_n(\phi) &= U_{n-1}(\phi) - \epsilon(U_{n-1}(\phi) - U_{\mathrm{RHS}}[\lambda_{n-1}]), \\ J_n(H) &= J_{\mathrm{RHS}}[U_n], \\ \lambda_n(\phi) &= \lambda_{\mathrm{RHS}}[J_n, U_n]. \end{aligned} \tag{3.2}$$

If the solution exists, the process converges to it provided the convergence parameter $\epsilon > 0$ is sufficiently small. The problem of existence and uniqueness of that solution is also considered and discussed in [12]. For the case of the inductive impedance and for the intensities considered here the algorithm was always converging.

3.2.2 Stability analysis

Taking into account the potential-well distortion, stability can be determined by solving the linearized Vlasov equation for a small perturbation $F_1(J,\psi,t)$ to $F_0(J)$ as mentioned in section 2.5. Using the Oide-Yokoya expansion [61] of the perturbation $F_1(J,\psi,t)$ in terms of the orthogonal basis we have

$$F_1(J,\psi,t) = e^{-i\omega t}\sum_{m=-\infty}^{\infty}[f_m(J)\cos(m\psi) + g_m(J)\sin(m\psi)]. \tag{3.3}$$

Substituting Eq. (3.3) into the Vlasov equation (2.122) after multiplying both sides by $\cos(m\psi)$ or $\sin(m\psi)$ and integrating over ψ we get the following system of equations:

$$\begin{aligned} i\omega f_m(J) &= m\omega_s(J)g_m(J), \\ i\omega g_m(J) &= -m\omega_s(J)f_m(J) - \frac{1}{\pi}\frac{dF_0(J)}{dJ}\int_0^{2\pi} d\psi\sin(m\psi)\frac{\partial U^1_{\rm ind}(\phi,t)}{\partial\psi}. \end{aligned} \tag{3.4}$$

In the above equations we use the fact that $\phi(\psi) = \phi(2\pi-\psi)$ and therefore by making the substitution $\psi = 2\pi - \psi$ one can show that

$$\int_0^{2\pi} d\psi\cos(m\psi)\frac{\partial U^1_{\rm ind}(\phi,t)}{\partial\psi} = 0, \tag{3.5}$$

since the integrand is an odd function. Combining the two equations (3.4) and integrating by part the integral we get

$$\left[\omega^2 - m^2\omega_s^2(J)\right] f_m(J) = -\frac{m^2\omega_s(J)}{\pi}\frac{dF_0(J)}{dJ}\int_0^{2\pi} d\psi\cos(m\psi)U^1_{\rm ind}(\phi,t), \tag{3.6}$$

where

$$\begin{aligned} U^1_{\rm ind}(\phi) &= -\frac{Nq^2}{2\pi}\int_0^{2\pi} d\psi'\int_0^{\infty} dJ' F_1(\psi',J')S\left[\phi(\psi,J) - \phi'(\psi',J')\right] \\ &= -\frac{Nq^2}{2\pi}\int_0^{2\pi} d\psi'\int_0^{\infty} dJ' S\left[\phi(\psi,J) - \phi'(\psi',J')\right]\sum_{m'=-\infty}^{\infty} f_{m'}(J')\cos(m'\psi') \end{aligned} \tag{3.7}$$

and

$$S(\phi) = \int_{-\infty}^{\phi} d\phi' W(\phi'). \tag{3.8}$$

Again for the same reason as before

$$\int_0^{2\pi} d\psi' S\left[\phi(\psi,J) - \phi'(\psi',J')\right]\sin(m'\psi') = 0. \tag{3.9}$$

Inserting Eq. (3.7) into Eq. (3.6) we finally obtain the following integral equation

$$\left[\omega^2 - m^2\omega_s^2(J)\right] f_m(J) = -2m^2\omega_s(J)\frac{dF_0(J)}{dJ}\sum_{m'=-\infty}^{\infty}\int_0^{\infty} dJ' V_{mm'}(J,J')f_{m'}(J'), \tag{3.10}$$

where

$$V_{mm'}(J,J') = -\frac{Nq^2}{\pi^2}\int_0^{\pi} \mathrm{d}\psi \int_0^{\pi} \mathrm{d}\psi' \cos(m\psi)\cos(m'\psi')\; S\left[\phi(\psi,J) - \phi'(\psi',J')\right] \tag{3.11}$$

Approximating the integral in Eq. (3.10) by a sum, one ends up with a standard eigenvalue problem of linear algebra. This equation can be solved numerically to get the spectrum of the Van Kampen modes as was done in [12,13]. after some modifications to take into account cases of non-symmetric RF potentials (double RF with a phase shift).

Analyzing the dispersion integral obtained from the Vlasov equation for infinite plasma, Van Kampen [62,63] has found that it consists of a continuous and a discrete part. The continuous spectrum (Van Kampen modes) is described by singular eigen-functions coinciding with the incoherent synchrotron frequencies inside the bunch $\omega_s(J)$. Landau damping results then from phase mixing of the Van Kampen modes which are real and do not represent collective motion of the particles. At low intensities, when the interaction term is negligible ($U^1_{\mathrm{ind}}(\phi) \approx 0$), all the modes belong to the incoherent spectrum, $\omega = m\omega_s(J)$, see Eq. (2.123). On the contrary, above a certain intensity N_{th} the discrete modes can emerge. These modes are described by regular functions and by definition they lie outside $\omega_s(J)$, implying that Landau damping is lost [12,13].

Figure 3.1 presents an example of the eigen-modes (red points) obtained from Eq. (3.10) for the rigid dipole mode ($m = 1$) and a double RF system in the BLM. One can clearly notice the discrete mode emerging above the incoherent spectrum (blue curve) meaning that for that mode Landau damping is lost.

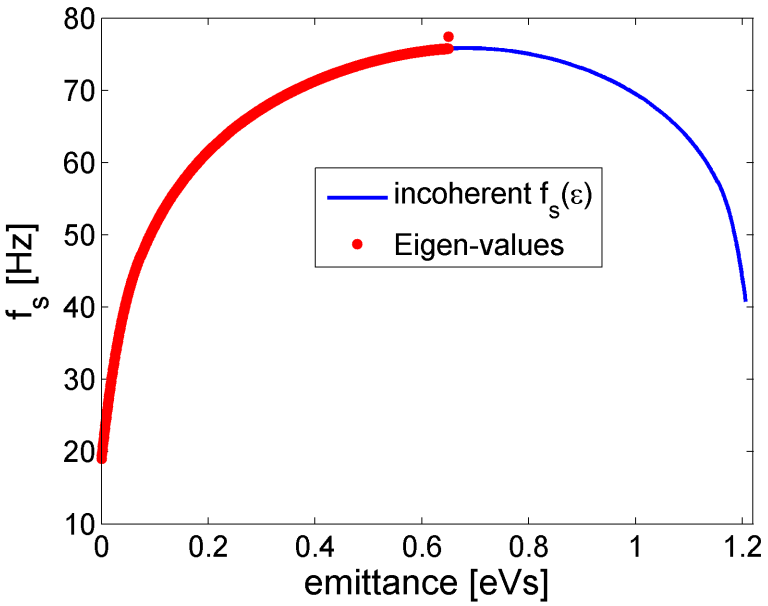

Figure 3.1: Example of the eigen-modes (red points) obtained from Eq. (3.6) for $m = 1$ and a double RF system in the BLM. The red point above $\omega_s(J)$ (blue curve) corresponds to a discrete mode which shows that for the emittance of 0.65 eVs Landau damping is lost. The bunch intensity was $7{\times}10^{10}$ p.

3.3 Macroparticle simulations

In order to verify the loss of Landau damping obtained by the semi-analytical approach described in section 3.2, a multi-particle tracking code was created in Matlab to simulate the effect. The concept of macroparticles was used to represent a bunch. Each macroparticle i is tracked in the phase space (ϕ_i,ΔE_i) of the RF phase (defined by the main RF system) and the energy coordinate. The longitudinal equations of motion Eqs. (2.30), (2.31) were used including the intensity effects. The code was developed for protons and based on the SPS parameters, so radiation damping and quantum fluctuation were not considered. The minimum values of ϕ_i correspond to the head of the bunch and the maximum to the tail, while $\Delta E_i \equiv u_i$ is the energy difference between the macroparticle i and the synchronous particle.

Each turn, the induced voltage is calculated in frequency domain $V_{\rm ind}(\omega)$ from the spectrum $\lambda(\omega)$ of the line density (projection of macroparticles onto the ΔE axis) according to Eq. (2.84). Standard smoothing algorithms were also applied to $\lambda(\phi)$ in order to get rid of the numerical high frequency noise due to a limited number of particles. Then $V_{\rm ind}(\phi)$ is obtained from the inverse Fourier transform of $V_{\rm ind}(\omega)$ and added to the external RF voltage $V_{\rm rf}(\phi)$ to get the total effective voltage $V_{\rm tot}(\phi)$ seen by the particles. The advance of each macroparticle after one turn at $\rm n_{th}$ turn is given by the following equations:

$$\begin{aligned} u_{i,n+1} &= u_{i,n} + V_{\rm tot}(\phi_i) \\ \phi_{i,n+1} &= \phi_{i,n-1} + \frac{2\pi h\eta}{\beta^2 E_0} u_{i,n+1}, \end{aligned} \tag{3.12}$$

with h being the harmonic number of the main RF system.

Numerical simulations presented here were performed using 5×10^5 macroparticles. The initial matched distribution was created iteratively (as in the semi-analytical calculations) and placed into the RF bucket with a small phase error of $\phi_0 = 3^\circ$, enough to excite the rigid dipole motion of the bunch. Tracking the particles for ∼300 synchrotron periods T_s was adequate to study the effect of Landau damping. Figure 3.2 presents examples of the rms bunch position evolution for the cases below and above the threshold.

The criterion used here to estimate the threshold is based on the relative change of the dipole oscillation amplitude $\phi_{\rm max}$ (envelope of the oscillations in Fig. 3.2), averaged after 100 T_s (transients). The ratio $\phi_{\rm max}/\phi_0$ is plotted in Fig. 3.3 for different emittances for the BLM. The threshold was selected to be 80% (horizontal line) and although being a rather random choice it affects only the absolute values and not the physical interpretation. In particular, as can be seen in Fig. 3.3, choosing the threshold to be at another level, for example at 50%, it would still give the same relative result for the different longitudinal emittances.

A comparison of both the analytical approach and the simulations with another tracking code, for different particle distributions in the case of single RF system and inductive impedance, showed a very good agreement [64].

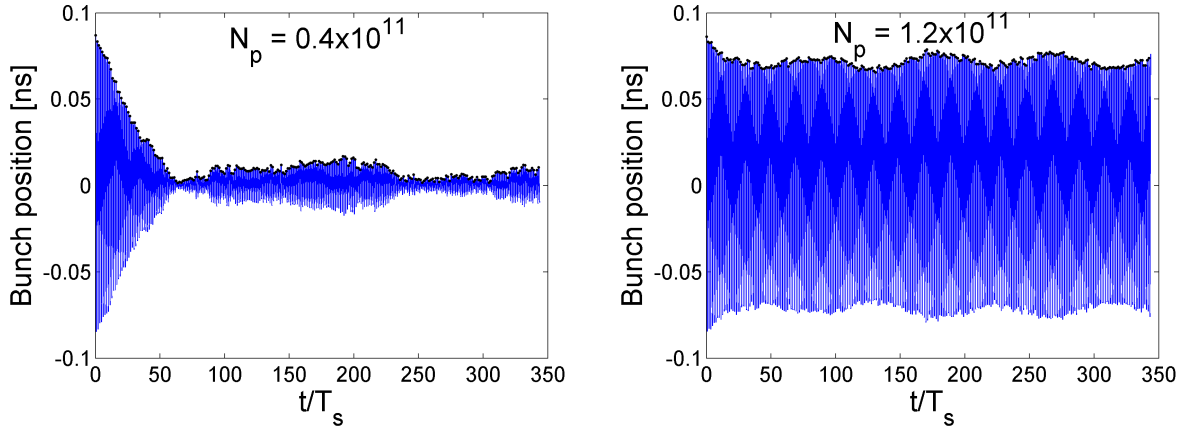

Figure 3.2: The rms bunch position versus number of synchrotron periods for bunch intensity below the threshold of loss of Landau damping (left) and above it (right) in a double RF system in BLM. The voltage ratio between the two RF systems at $V_1/V_2 = 2$.

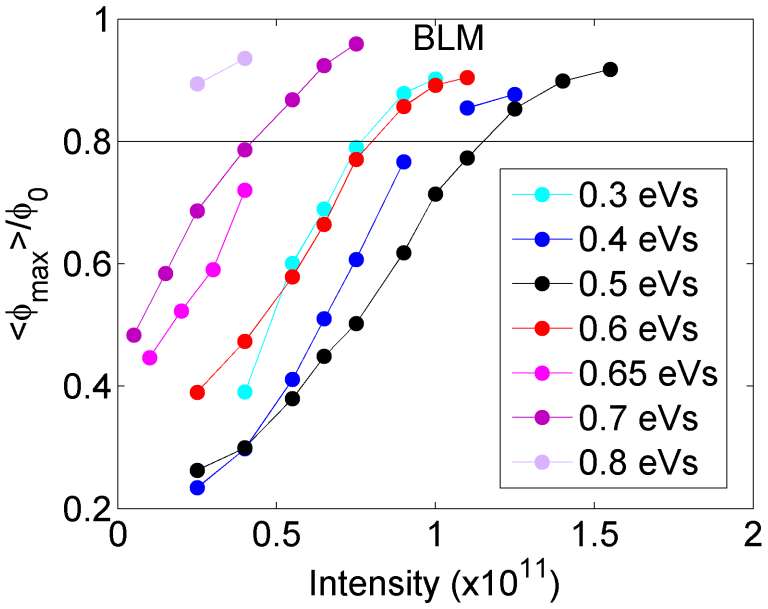

Figure 3.3: Relative change of the averaged dipole oscillation amplitude versus bunch intensity for different emittances in BLM, $\phi_0 = 3°$. The voltage ratio between the two RF systems at $V_1/V_2 = 2$.

3.4 Results for a second harmonic RF system (n=2)

As mentioned above, both calculations and simulations were applied for the SPS during the p$\bar{\text{p}}$ operation. The 2 RF systems were set up in the BLM with voltage amplitudes $V_{100} = 0.6$ MV and $V_{200} = 0.3$ MV, while for the phase-space density the distribution $F(J) = (J_{\text{lim}} - J)^2$ [14] was used, close to the one fitted to measurements. The intensity thresholds of the loss of Landau damping were defined for different longitudinal emittances. These thresholds N_{th}, found for the BLM by calculations from the onset of the discrete Van Kampen mode and in simulations from the crossing of the horizontal line in Fig. 3.3 with the curves for different emittance, are presented in Fig. 3.4 (red color).

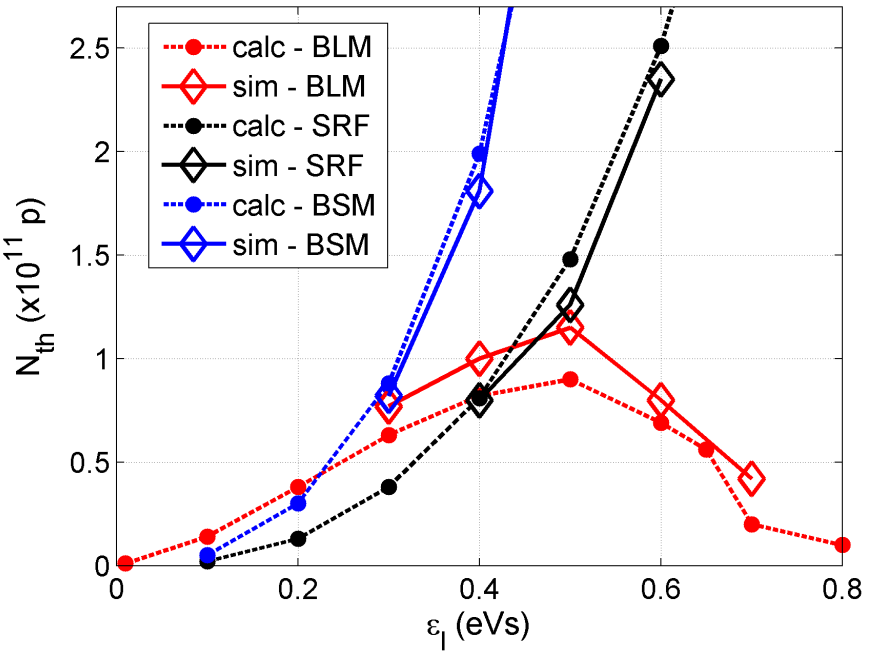

Figure 3.4: Loss of Landau damping thresholds versus bunch emittance for a double RF (BLM - red, BSM - blue) and a single RF (black) systems found from calculations (dots) and simulations (diamonds). Application for the SPS during the p$\bar{\text{p}}$ operation at injection energy (26 GeV/c). Voltage ratio between the two RF systems at $V_1/V_2 = 2$.

Both curves, being in a very good agreement, show that N_{th} increases with emittance ε_ℓ until some value of ~0.5 eVs. After this point further increase in ε_ℓ leads to threshold reduction. In fact, an inspection of the incoherent synchrotron frequency distribution, see Fig. 3.5 (red curve), shows that the flat region where $\omega_s^{'}(J) = 0$ (vertical line) corresponds to the critical emittance $\varepsilon_{\text{cr}} = 0.65$ eVs.

This result can actually explain the un-damped oscillations at the injection plateau during the p$\bar{\text{p}}$ operation, since for the nominal (0.65 eVs) or larger emittances the threshold for the loss of Landau damping is very low. Although the spread of the $\omega_s(J)$ inside the bunch is still big, the lack of stability in this case is determined by the non-monotonic behavior of the $\omega_s(J)$ in

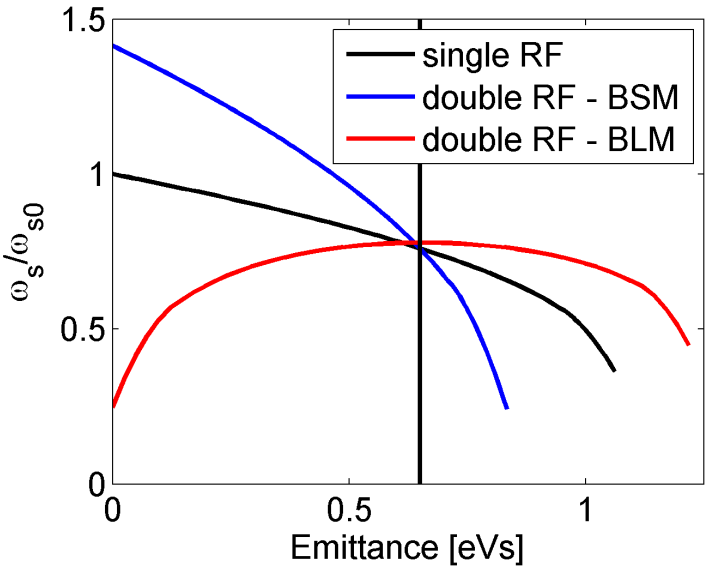

Figure 3.5: Relative synchrotron frequency distribution for a double RF (BLM - red, BSM - blue) and a single RF (black) systems. No intensity effects are included. The vertical line at 0.65 eVs indicates the maximum of the BLM curve. Similar conditions as in Fig. 3.4.

the tails of the bunch.

The effect of the phase shift ($\Delta\phi$) between the 2 RF systems around $\varepsilon_{\rm cr}$ was also studied. The calculated $N_{\rm th}$ is presented in Fig. 3.6, where one can see that although for small shifts the threshold goes down, after around 15° a dramatic increase takes place, explaining again the cure of the instability which was found empirically during the p$\bar{\rm p}$ operation. However, in this case the flatness of the bunches is lost since the potential well is not anymore symmetric (see Fig. 3.7).

For completeness, the same studies were also applied for a single RF and a double RF in the BSM. The results are presented in Fig. 3.4, where one can see that for both of them $N_{\rm th}$ keeps increasing with the emittance, as was expected from the monotonic behavior of their $\omega_s(J)$ distributions shown in Fig. 3.5. For bunches with $\varepsilon_\ell < 0.2$ eVs, the BLM is the preferable mode at operation, while after this value the threshold of the BSM is rapidly increasing, making this mode a better choice for stability. However, it is clear from Fig. 3.8 that the BSM is unacceptable above 0.6 eVs due to lack of longitudinal acceptance, which would lead to significant particle losses. For $\varepsilon_\ell > 0.6$ eVs a single RF seems to be the best option.

Similar results were obtained in ref [12] for a resistive wake where again the threshold for loss of Landau damping in BLM is the highest for small emittances but for higher emittances drops first below the threshold in BSM and then below the single RF case.

For a space charge wake above transition the threshold, found both from simulations and calculations, is significantly increasing, which is in good agreement with theoretical predictions in [16]. In that case, the induced voltage enhances the focusing of the particles, leading to an increase of the incoherent and coherent synchrotron frequencies, see Eq. (2.109). In the BLM the region of $\omega_s^{'}(J) = 0$ is still present. However, the frequency shift of the coherent mode $\delta\omega_{\rm c}$ is less than the incoherent one $\Delta\omega_{\rm s}$ and hence the coherent motion is still Landau damped.

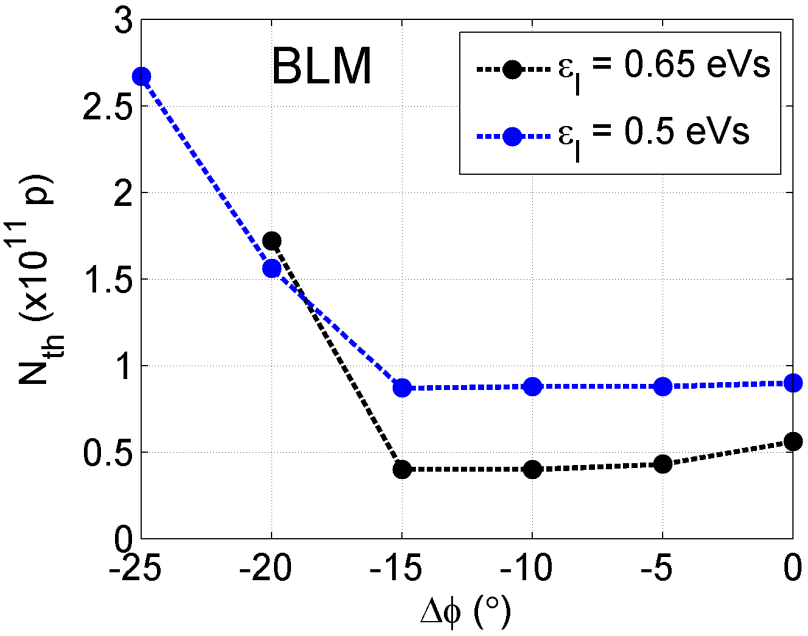

Figure 3.6: Loss of Landau damping thresholds versus the phase shift between the 2 RF systems found from calculations. Similar conditions as in Fig. 3.4.

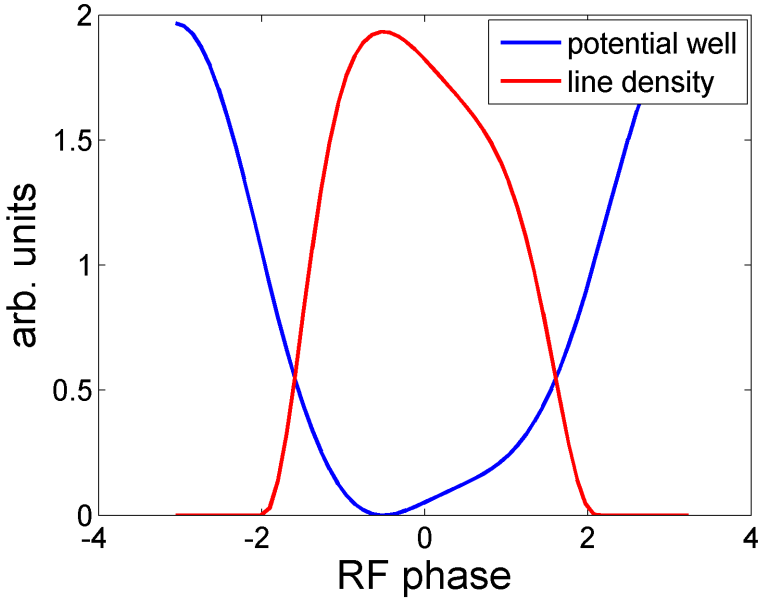

Figure 3.7: Potential well (blue curve) and line density (red curve) in the case of BLM with $\varepsilon_\ell = 0.65$ eVs and a phase shift of $-20°$. Bunch intensity of 1×10^{11}.

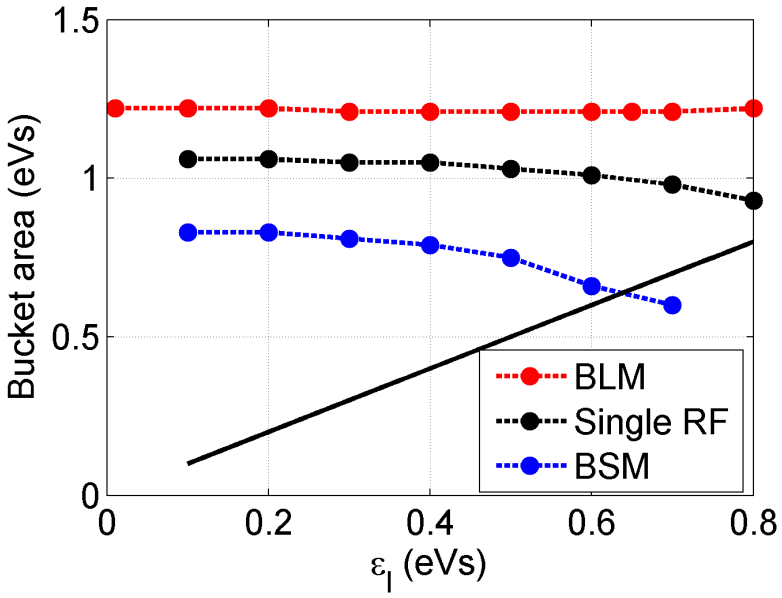

Figure 3.8: Bucket area versus emittance for a double RF (BLM - red, BSM - blue) and a single RF (black) in the cases corresponding to the N_{th} in Fig. 3.4. The black straight line is the limit where ε_ℓ is equal to the bucket area.

3.5 Results for higher harmonic RF systems (n>2)

In the SPS the 4th harmonic RF system (800 MHz) is installed and used in operation for the LHC beams. For higher harmonic ratios $n = h_2/h_1$ a region where $\omega_s^{'}(J) = 0$ appears again in the BLM (Fig. 3.9). Note that in the following results, in order to ensure the maximum synchrotron frequency spread inside the bunch, the ratio between the two RF voltages is assumed to be $V_1/V_2 = n$.

As Fig. 3.9 shows, the second RF system with a high harmonic ratio provides larger synchrotron frequency spread. However, the maximum bunch length is more restricted in operation due to the fact that the regions where Landau damping is lost are in this case closer to the center of the bunch. From this point of view the second harmonic RF system has the largest useful parameter space.

Furthermore, unlike in the case of the second harmonic with n =2, for n =3, 4 the regions where $\omega_s^{'}(J) = 0$ appear also in the BSM (Fig. 3.10). As mentioned above, particularly interesting, for the SPS today, is the case of the 4th harmonic in the BSM (Fig. 3.10, red curve). Indeed, simulations for this case and inductive impedance show that the threshold of the loss of Landau damping is sensitive even to the local extremums of the synchrotron frequency distribution. These thresholds versus the longitudinal emittance, found from simulations with the same method as before, are presented in Fig. 3.11. Note that for this shape of the synchrotron frequency distribution the analytical calculations predict a much higher threshold. That is justified by the fact that the emerge of the discrete mode, above the incoherent spectrum, corresponds to the center of the bunch ($J = 0$), where we have the global maximum of $\omega_s(J)$. Therefore, much

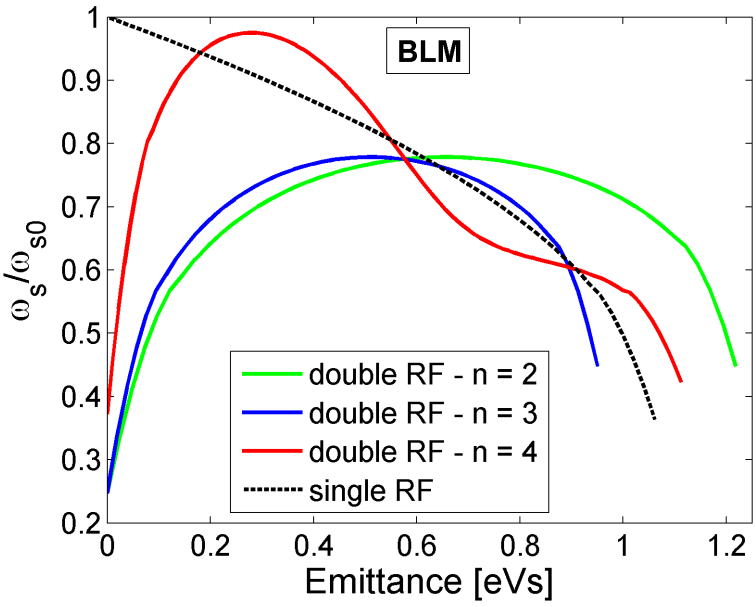

Figure 3.9: Relative synchrotron frequency distribution inside the bunch for different harmonic ratios $n = h_2/h_1$ and voltage ratio $V_1/V_2 = n$ for the BLM. Example for the 100 MHz voltage $V_1 = 0.6$ MV, 26 GeV/c.

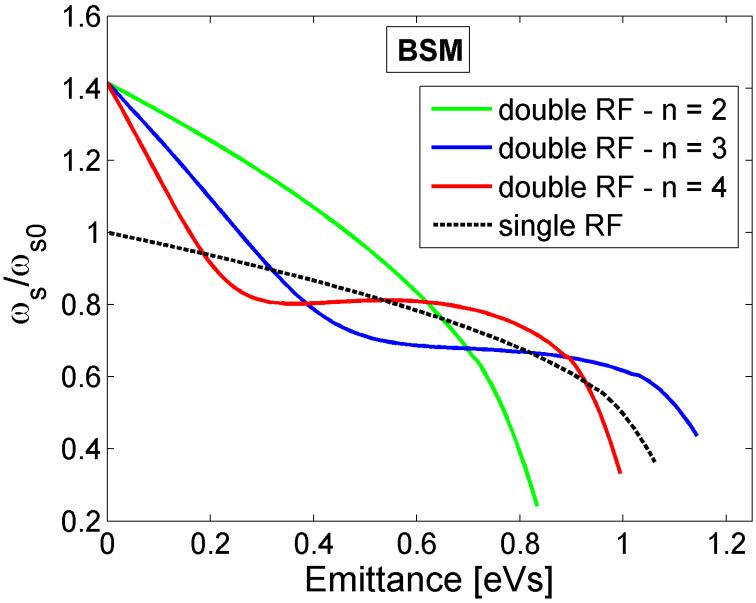

Figure 3.10: Relative synchrotron frequency distribution inside the bunch for different harmonic ratios $n = h_2/h_1$ and voltage ratio $V_1/V_2 = n$ for the BSM. Example for the 100 MHz voltage $V_1 = 0.6$ MV, 26 GeV/c.

higher number of particles is needed.

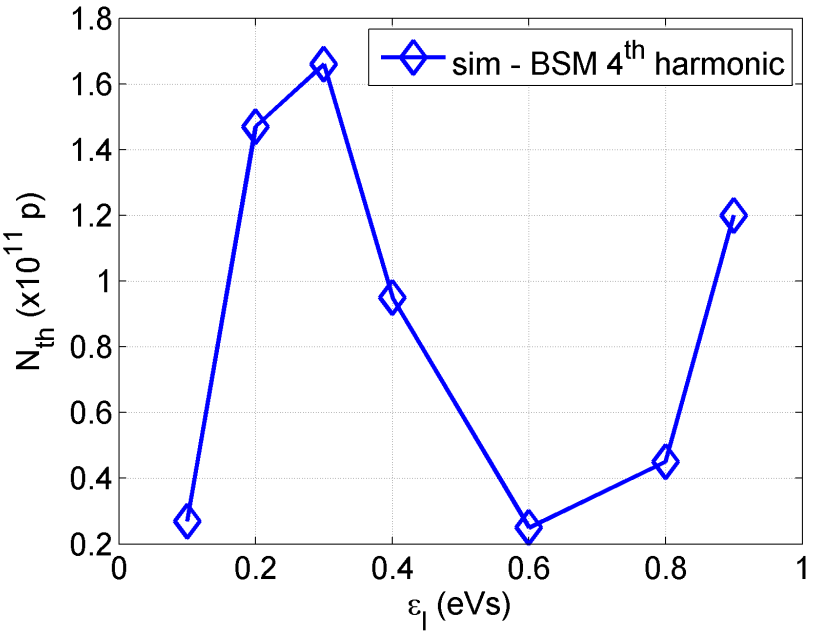

Figure 3.11: Loss of Landau damping thresholds versus bunch emittance for $h_2/h_1 = 4$ in BSM found from simulations.

One can see from Fig. 3.11 that for small bunches ($\varepsilon_\ell < 0.3$ eVs), where $\omega_s(J)$ is monotonically decreasing, the threshold is growing with the emittance. That is not anymore true above the first minimum in $\omega_s(J)$ when we observe a significantly lower threshold. However, by increasing further the bunch emittance the situation is improving once again. This can be attributed to the further increase of the spread $\Delta\omega_s$ of the incoherent synchrotron frequencies inside the bunch (see Fig. 3.10, red curve).

Today the SPS is used as the LHC injector, where the beam is captured and accelerated with the 200 MHz RF system. In addition the 4^{th} harmonic RF system (800 MHz) is used in the BSM to stabilize the beam [60]. Since the nominal values of the injected emittances are around 0.35 eVs the bunch size is bigger than ε_{cr} for the BLM ($\sim$0.15 eVs) and thus in this mode, and for purely inductive impedance, no Landau damping is present. As mentioned before, the same is also true for the case of the BSM when the voltage ratio between the two RF components is high ($V_1/V_2 = 4$). The detailed studies for the current parameters of the SPS RF system with a more realistic model of the longitudinal impedance are presented in the next Chapter.

3.6 Conclusions

Many accelerators in our days are operating with a double RF system in the BLM in order to decrease the peak line density and to increase the synchrotron frequency spread inside the bunch, making Landau damping more effective. However, it was proven here, both by simulations and calculations, that for the inductive impedance there is a critical value of the longitudinal

emittance, above which the Landau damping threshold decreases rapidly to zero. A phase shift between the two RF components of more than 15° in the BLM can help to increase the threshold, but the flatness of the bunches is lost. These results are able to explain observations during the $p\bar{p}$ operation of the SPS.

For a capacitive impedance (or space charge above transition) the thresholds are either dramatically increased or could not be found, which is in agreement with the theoretical prediction in [16], where it was proved that for the space charge impedance above transition, a bunch steady state is always stable.

The analysis was applied for different harmonic ratios $h_2/h_1 = n$ between the two RF systems, by keeping the voltage ratio $V_1/V_2 = n$. It was shown that although higher n provides larger synchrotron frequency spread, the critical region moves closer to the center of the bunch, which is limiting the bunch length (or the longitudinal emittance for fixed voltage V_1) that can be used in operation. In addition, in the case of the BSM with $n \geq 3$ the regions where $\omega_s^{'}(J) = 0$ are also appearing as local extrema. Consequently, for emittances larger than those regions, the threshold of the loss of Landau damping is significantly decreased. These results agree very well with the recent measurements in the SPS using the 4^{th} harmonic RF and this will be presented in the next Chapter.

Chapter 4

Single bunch instabilities in the CERN SPS double RF system

A fourth harmonic RF system is used in the SPS as a Landau cavity, in order to stabilize the high intensity LHC proton beam against the longitudinal instabilities. Numerous studies proved that operation of the two RF systems in bunch shortening mode through the whole cycle is necessary to provide a good quality beam at extraction to the LHC. Furthermore, it was shown that the choice of RF parameters such as voltage amplitude ratio and relative phase, is critical for the beam stability. In this Chapter the single bunch measurements performed in single and double RF systems with various RF settings are presented and compared with results of macroparticle simulations for the SPS impedance model. It will be shown that the theoretical approach of the previous Chapter is also applicable in this, more realistic, situation.

4.1 Introduction

In the SPS, operation of the fourth harmonic RF system is required through the whole cycle, together with the main 200 MHz RF system, to deliver a good quality beam for the LHC. Indeed, in a single RF system and the Q26 optics, the LHC beam (one batch of 36 bunches spaced by 50 ns with injected longitudinal emittances of 0.35 eVs) becomes longitudinally unstable during acceleration already at 2×10^{10} ppb (eight times less than the nominal intensity) [41]. Note that this instability can not be damped by the present RF feedback, feed-forward (around the 200 MHz RF cavities) and longitudinal damper (low modes) used in operation.

The necessity of the double RF system operation for the beam stability in the SPS and the effect the relative phase (ϕ_{800}) has on it, has initiated different studies both for multi and single bunch beams [10,65–67]. All these studies had consistently shown that the best operating mode of the 4^{th} harmonic RF system is the BSM, whereas in the BLM it is not possible to produce a stable beam above a relatively low intensity threshold. Moreover, in agreement with the results of the previous Chapter, instability was also measured in the BSM when the voltage ratio between the two RF systems was equal to the harmonic ratio, i.e $V_r = V_{800}/V_{200} = 1/4$.

In the previous Chapter we showed that the phase shift between the two RF systems, for a 2^{nd} harmonic RF in the BLM, increases significantly the loss of Landau damping threshold and therefore should lead to the damping of the bunch oscillations at the injection plateau (26 GeV/c). In this Chapter we investigate the effect of ϕ_{800} on the bunch stability, in the case of the 4^{th} harmonic RF, also at the injection energy. In order to enhance the effect of the 800 MHz component, we selected rather a large value of $V_r = 0.25$. Scanning ϕ_{800} for this voltage ratio, different stability regions were obtained as compared to the BSM phase that is being used

in operation (with $V_r \simeq 0.1$). Numerical simulations, performed using the code ESME [17] for the impedance model of the SPS are compared with the measurements.

4.2 Phase calibration of a double RF system

In a double RF system the total external voltage seen by the particles has the form

$$V = V_{200} \sin\phi + V_{800} \sin(4\phi + \phi_{800}), \tag{4.1}$$

where V_{200} and V_{800} are the voltage amplitudes of the 200 MHz and 800 MHz RF components and ϕ_{800} is the relative phase. In operation though, ϕ_{800} is defined up to some unknown phase offset ϕ_0,

$$\phi_{800} = \phi_0 + \Delta\phi_{800}, \tag{4.2}$$

which can be found from a calibration, performed at the beginning of each beam run. This phase calibration is based on measuring the symmetry of the longitudinal profile of a single low intensity bunch ($\sim 1\times10^{10}$ p) as a function of the phase ϕ_{800}, at the injection energy (26 GeV/c).

Indeed, in the case of a stationary bunch, the potential well (found from Eq. (2.32)) is symmetric both in the BSM and the BLM (above transition $\phi_{800} = \pi$ and $\phi_{800} = 0$, respectively). However, by introducing a phase shift between the 2 RF systems, the potential well loses its symmetry and so does the bunch line density. This can be seen in Fig. 4.1 where the cases of $\phi_{800} = 180°$ and $\phi_{800} = 180° - 50°$ in the BSM are presented. In addition, one can see in

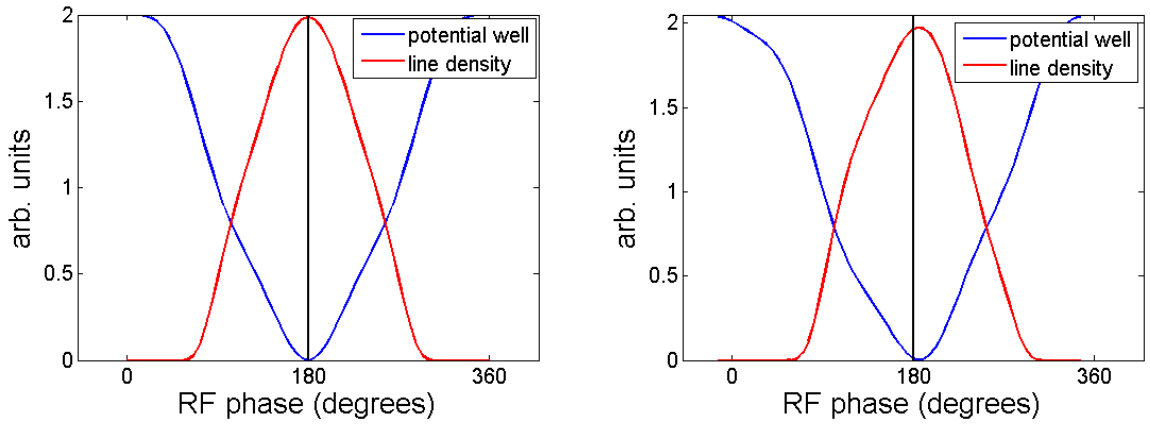

Figure 4.1: Potential well (blue curve) and line density (red curve) in the case of the BSM with a 4^{th} harmonic RF system for $\phi_{800} = 180°$ (left) and $\phi_{800} = 180° - 50°$ (right) No intensity effects were included.

the right plot of Fig. 4.1 that the synchronous phase ϕ_s, which can be obtained by solving the following equation for ϕ

$$V_{200} \sin\phi + V_{800} \sin(4\phi + \phi_{800}) = 0, \tag{4.3}$$

is not anymore 180° (above transition energy), but an extra phase of $\sim 6°$ was added. The shift of ϕ_s versus ϕ_{800}, calculated from the above equation and for different voltage ratios of the two

RF systems, is depicted in Fig. 4.2. The points where the curves are crossing zero designate the BSM or BLM. From this plot one can also see that the region of the allowed phase shift is much wider in the BSM than in the BLM, where even small variations in ϕ_{800} cause a big change in ϕ_s. That tight requirements on the accuracy of ϕ_{800} is in fact the second main restriction of operation in the BLM[1] which, due to strong beam loading in both the main and high harmonic RF systems, is very difficult to achieve in the SPS (see next Chapter).

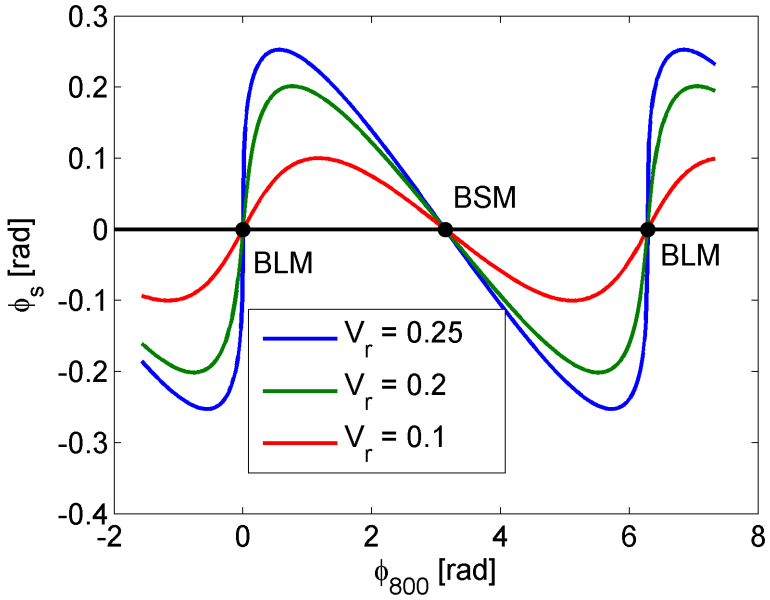

Figure 4.2: Calculated shift of the synchronous phase versus phase ϕ_{800} for different RF voltage ratios V_r. The region of the BLM is decreasing with the voltage ratio increase.

Similar behavior due to variation of the ϕ_{800} is expected for the asymmetry of the bunch. Therefore, by scanning the phase ϕ_{800} and measuring how much the bunch is tilted it is possible to estimate the points that correspond to the BSM and the BLM. The algorithm used to estimate the tilt is based on the full widths of the average bunch profile (out of 100 consecutive turns) at 95% and 30% of the maximum (horizontal black lines in Fig. 4.3). After finding the latter, the tilt is calculated from the difference between the middle points of the two lines (red points in Fig. 4.3).

Figure 4.4 presents the results obtained in measurements after a full scan of $\Delta\phi_{800}$, see Eq. (4.2). Note that in this plot the phase on the horizontal axis is defined in degrees at the 200 MHz. In addition, in order to minimize the intensity effect on the bunch shape we used bunches with a relatively low intensity ($\sim 1\times10^{10}$ p). The voltage ratio between the 2 RF systems was $V_r = 0.25$ with the 200 MHz RF voltage at 2 MV. For each phase offset we performed three acquisitions (blue circles in Fig. 4.4), the mean value of which (black curve) was used to define the tilt.

[1]The first restriction is due to the region with a local maximum in the synchrotron frequency distribution inside the bunch, which, as we saw on Chapter 3, is reducing the instability threshold.

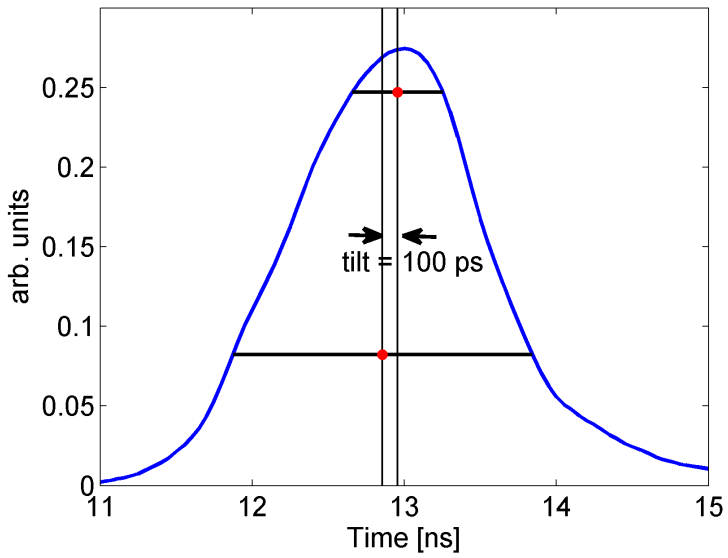

Figure 4.3: Schematic example of the algorithm used to calculate the tilt of the bunch profiles. The horizontal lines correspond to the full widths at 95% and 30% of the line density maximum. This measured bunch profile corresponds to a case of $\phi_{800} \approx 76°$. Voltage ratio $V_r = 0.25$ and $V_{200} = 2$ MV.

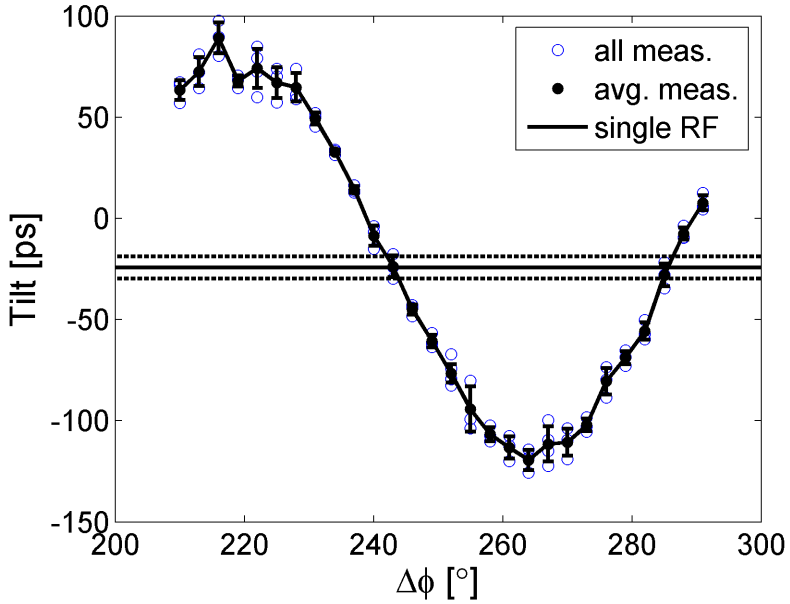

Figure 4.4: Measured bunch tilt versus relative phase (in deg at 200 MHz, unknown offset), 26 GeV/c, $V_r = 0.25$ and $V_{200} = 2$ MV.

Measurements were also performed in a single RF system in order to define the baseline. The average tilt from 10 acquisitions and its standard deviation are shown in Fig. 4.4 with the solid and dotted horizontal lines respectively. This baseline is not perfectly identical to zero due to the remaining induced voltage and also the effects of the pick-up and cable transfer functions, which also modify the symmetry of the bunch profile. Intersections of the horizontal line with the calibration curve of the double RF give the correct phases for the BSM and the BLM. By applying a linear fit to the points around the intersection we have in this case

$$\Delta\phi_{800}^{\mathrm{BSM}} = 242.95 \pm 0.87 \tag{4.4}$$

$$\Delta\phi_{800}^{\mathrm{BLM}} = 286.02 \pm 0.78 \tag{4.5}$$

where the errors are defined by the intersection with the dotted lines. As expected, the difference between the two modes is around 45° (at 200 MHz).

Finally, for high intensity operation the relative phase is selected by small scanning around the BSM and finding the value of ϕ_{800} that provides also the most stable beam on the SPS flat top.

4.3 Measurements in single and double RF systems

The results presented below were obtained during one machine development (MD) session in the SPS (November 2011) using the Q26 optics. The single bunch intensity was constant and around 1×10^{11}, close to the nominal value of the LHC beam with a 25 ns bunch spacing. The voltage amplitude of the 200 MHz RF was set to $V_{200} = 1$ MV since it was found [41] that bunches with this intensity are much more stable in this capture voltage. This value is close to the matched voltage for the bunch injected from the PS, and is much lower than the one used in operation with the LHC beam, where capture losses due to beam loading impose higher values (2 MV at injection increased after 50 ms to 3 MV). Note that the results obtained for matched voltage would be easier to compare with analytical calculations, where a steady state distribution is assumed. The longitudinal emittance ε_ℓ of the injected bunches was around 0.25 eVs, again lower than the nominal 0.35 eVs. The scanning of ϕ_{800} was performed around the BSM phase (ϕ_{800}^{BSM}). The feed-back, feed-forward and longitudinal dampers were switched off, whereas the phase loop was still acting on the bunch. The chromaticity was set high enough for the beam to be stable in the transverse plane. Longitudinal bunch profiles were acquired along the first 3.7 s of the 26 GeV/c flat bottom.

The stability analysis is based on the evolution of the 4σ bunch length τ along the flat bottom, obtained after applying to each acquired profile a Gaussian fit (without corrections for pick-up and cable transfer functions [68] which can be neglected in our case). An increase of τ at the end of the acquisition time (3.7 s) together with large bunch length amplitude oscillations (ΔT) indicates an unstable situation.

Prior to the phase scan in a double RF system, measurements in a single RF were performed showing that the bunch was stable under these conditions. Figure. 4.5 presents an example of the bunch length evolution along the flat bottom where one can see that, after the injection oscillations, the bunch is very stable (no bunch length oscillation or growth).

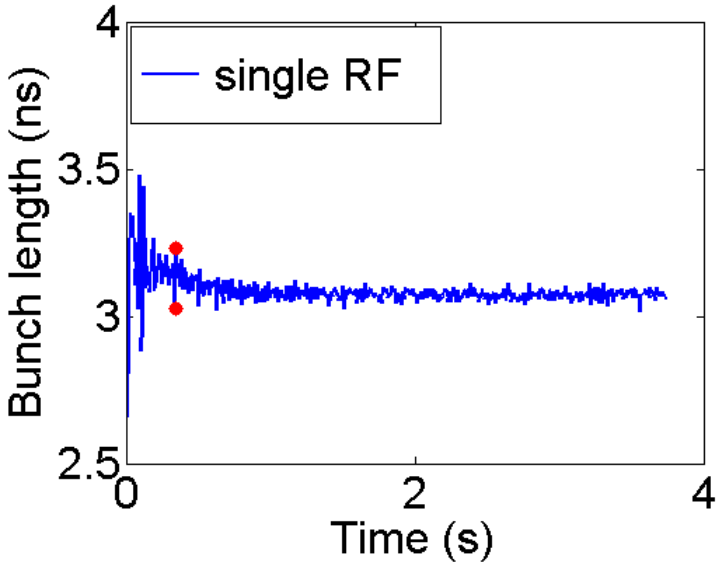

Figure 4.5: Bunch length evolution along the flat bottom in a single RF system. $V_{200} = 1$ MV. Bunch with intensity $\sim 1 \times 10^{11}$ and $\varepsilon_\ell \simeq 0.25$ eVs.

On the other hand, in the case of double RF system operating in the BSM with $V_r = 0.25$ the situation was very unstable. This case is shown in Fig. 4.6 where one can observe a continuous increase both in τ and oscillation amplitude ΔT, the maximum of which is presented in the plot with the two red points.

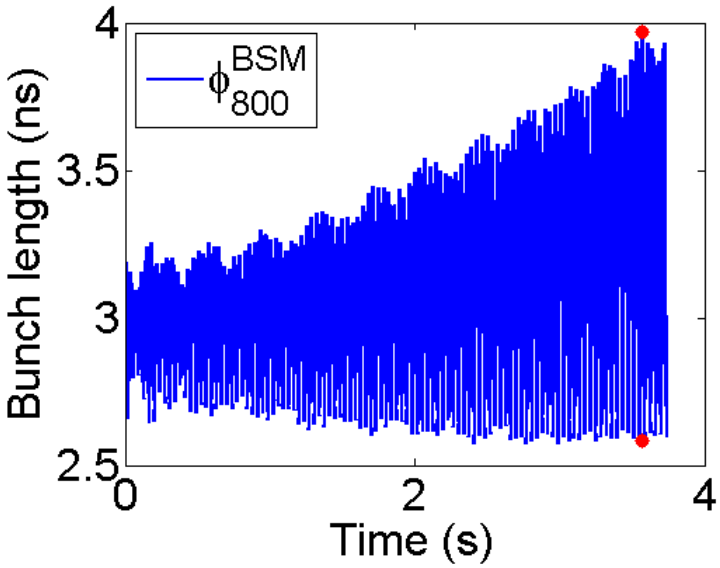

Figure 4.6: Bunch length evolution along the flat bottom for $\phi_{800} = \phi_{800}^{BSM}$, $V_{200} = 1$ MV and $V_{800} = 0.25$ MV. Bunch with intensity $\sim 1 \times 10^{11}$ and $\varepsilon_\ell \simeq 0.25$ eVs.

This observation does not in fact contradict to the statement that 800 MHz RF is necessary for beam stability in the SPS, since in operation a ratio of $V_r \simeq 0.1$ is used. Decreasing V_r to this value confirmed this result (Fig. 4.7).

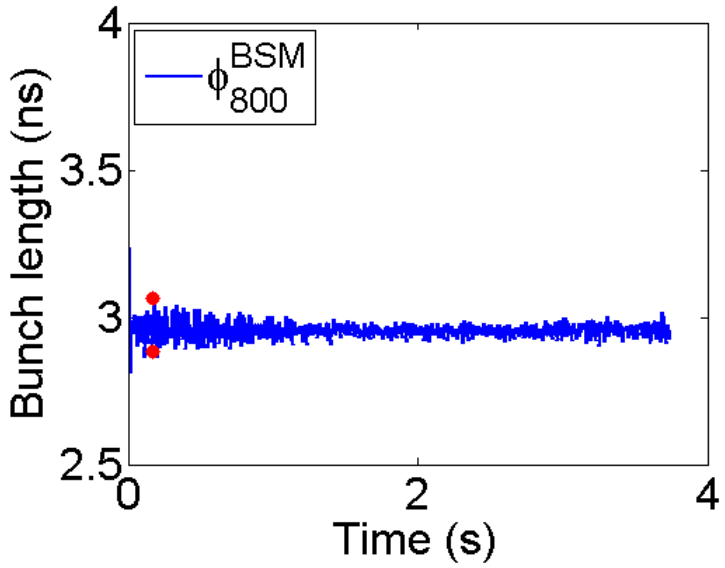

Figure 4.7: Bunch length evolution along the flat bottom for $\phi_{800} = \phi_{800}^{BSM}$, $V_{200} = 1$ MV and $V_{800} = 0.1$ MV. Bunch with intensity $\sim 1 \times 10^{11}$ and $\varepsilon_\ell \simeq 0.25$ eVs.

Stability could also be improved for $V_r = 0.25$ by shifting ϕ_{800} in both directions from the BSM phase, arriving after some point to a stable situation. Figure 4.8 shows the bunch length variation along the flat bottom for different values of ϕ_{800}. For completeness the case of $\phi_{800} = \phi_{800}^{BSM}$ is also included (top left plot).

As can be seen from Fig. 4.8, by shifting the phase from the BSM in both directions ($\phi_{800} = \phi_{800}^{BSM} - 64°$ - top right and $\phi_{800} = \phi_{800}^{BSM} + 80°$ - bottom left) the bunch remains stable along the cycle. Note that the initial oscillations, caused by the injection mismatch, are quickly damped ($\sim$ 100 ms). Further, a phase shift towards the BLM (bottom right plot) is again leading to instability.

A summary plot of all the measurements for $V_r = 0.25$ and different values of ϕ_{800} (average of three acquisitions per value of ϕ_{800}) is presented in Figs. 4.9 and 4.10 (blue trace). Figure 4.9 displays the ratio of final to initial bunch lengths $\tau_{\rm fin}/\tau_{\rm in}$ (averages for 100 ms), while Fig. 4.10 shows the ratio of final to initial bunch length oscillation amplitudes $\Delta T_{\rm fin}/\Delta T_{\rm in}$, multiplied by its maximum value $\Delta T_{\rm max}$ (to take into account the cases where the maximum was reached not at the end of the acquisition). Therefore, in both figures higher values correspond to more unstable situations.

As follows from Figs. 4.9 and 4.10, stable regions appear for phase shifts between 50° and 100°, relatively far from the BSM phase in both directions and a phase shift of around ±70° gives the best stability. Moreover, we can see that moving the phase ϕ_{800} towards the BLM leads again to degradation of the beam stability.

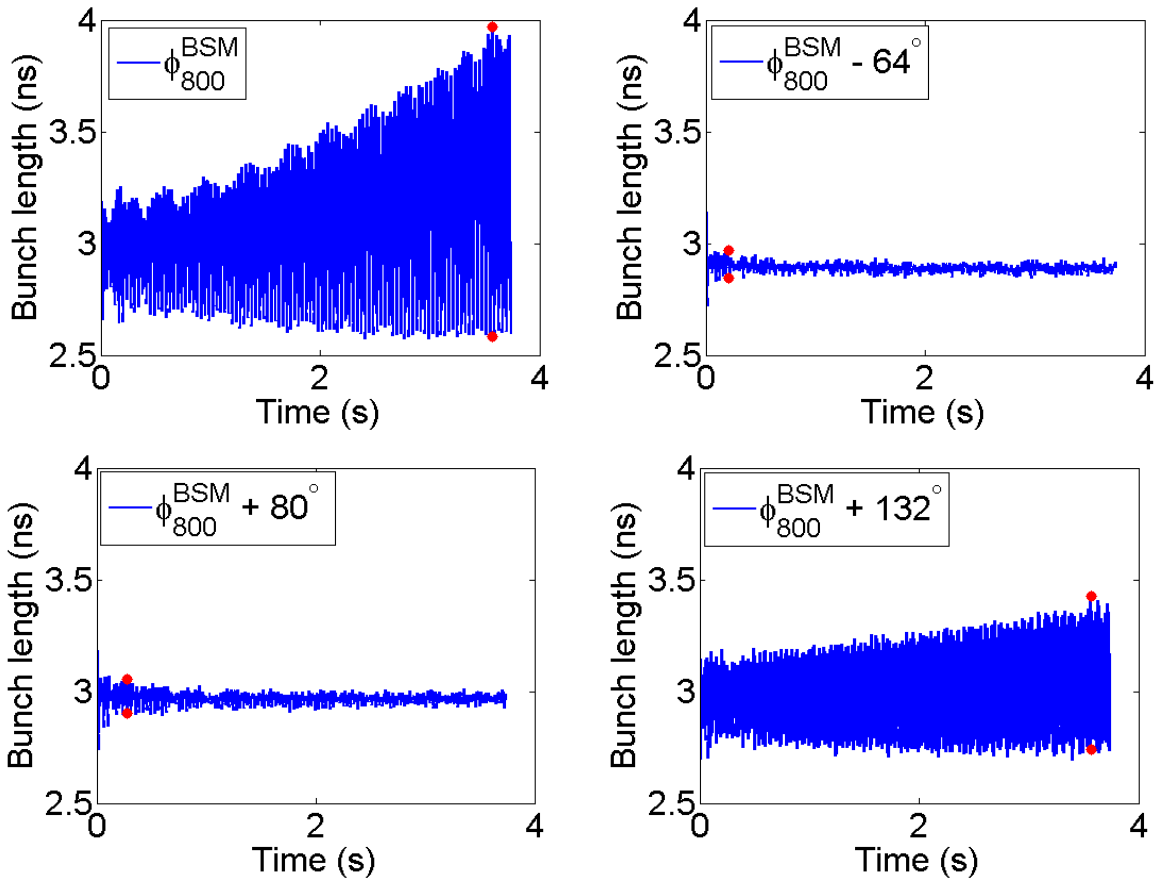

Figure 4.8: Bunch length evolution along the flat bottom for different values of ϕ_{800}, $V_{200} = 1$ MV and $V_{800} = 0.25$ MV. Bunch with intensity $\sim 1 \times 10^{11}$ and $\varepsilon_\ell \simeq 0.25$ eVs.

4.4 Macroparticle simulations

The results obtained in the measurements were compared with simulations performed using the code ESME (version es2009_4), a longitudinal beam dynamics simulation program [17], after introducing the SPS impedance model. This model was including the fundamental modes of the 200 MHz (long and short types) and 800 MHz traveling wave RF systems, one higher order mode (HOM) of the 200 MHz RF system [69] and the impedance of 16 kickers, the latter approximated by a broad-band resonator with Q=1. The parameters of the impedance sources used in simulations are presented in Table 4.1.

The initial phase-space particle distribution of the bunch was obtained by reconstructing a typical tomography measurement in the PS [70] and simulating it through the following complicated RF manipulations till extraction to the SPS [30]. Figure 4.11 presents this distribution at injection into the SPS. One can see that the bunch is not matched to the SPS bucket. Moreover, due to the bunch rotation applied in the PS before extraction, the distribution has an unconventional "S-shape".

Examples of evolution of the rms bunch position (dipole oscillations), obtained in simulations

Table 4.1: SPS impedance model used in ESME simulations

	f_r (MHz)	R_s (MΩ)	Q
TWC200-F (long)	200.2	2.86	150
TWC200-F (short)	200.2	1.84	120
TWC200-H	629.0	0.39	500
TWC800-F	800.8	1.94	150
Kickers	800.0	0.06	1

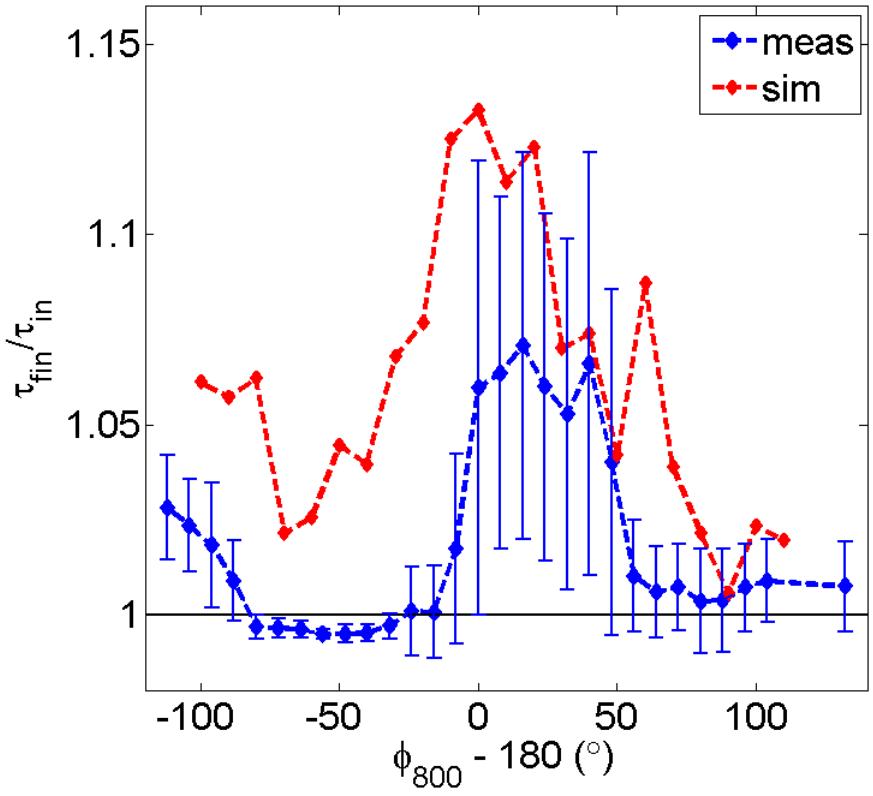

Figure 4.9: Ratio of final to initial bunch length on SPS flat bottom obtained from measurements and simulations in the SPS double RF system for different values of ϕ_{800} for $V_r = 0.25$. Bunch with intensity $\sim 1 \times 10^{11}$ and $\varepsilon_\ell \simeq 0.25$ eVs.

for $\phi_{800} = \phi_{800}^{BSM}$ and $\phi_{800} = \phi_{800}^{BSM} \pm 60°$ are shown in Fig. 4.12. Similarly to the measurements, the bunch is unstable in the BSM with $V_r = 0.25$, while it can be stabilized by applying a phase shift of 60° in both directions.

The simulation results are summarized in Figs. 4.9 and 4.10 (red trace) together with the measurements. A very good agreement between measurements and simulations can be seen in Fig. 4.9 for bunch length evolution in the SPS double RF system. Since simulations were performed without beam phase loop, the dipole oscillations were not damped and can be used

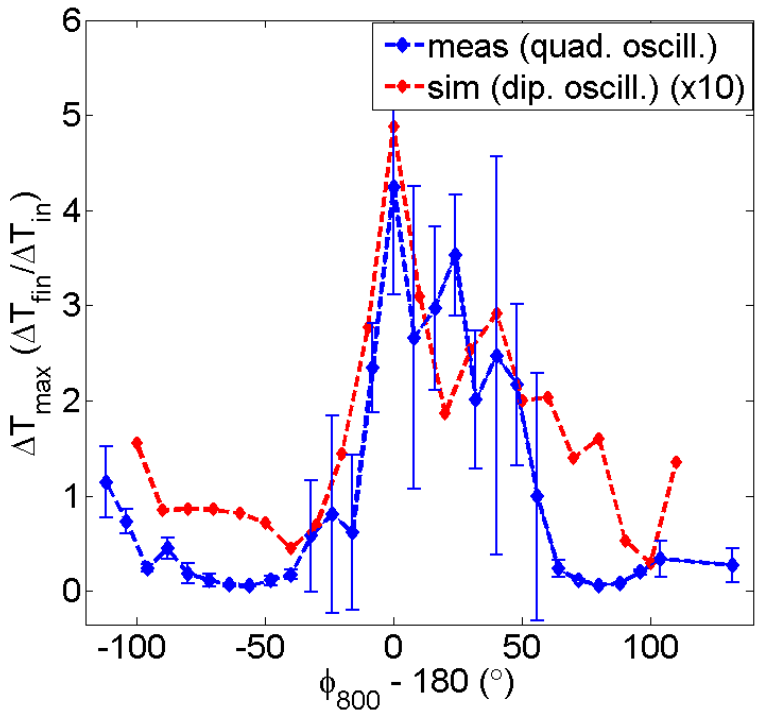

Figure 4.10: Ratio of final to initial quadrupole (measurements) and dipole (simulations) oscillation amplitude, multiplied by its maximum value ($\Delta T_{\max}$), as a function of ϕ_{800} in the SPS double RF system with $V_r = 0.25$. Bunch with intensity $\sim 1 \times 10^{11}$ and $\varepsilon_\ell \simeq 0.25$ eVs.

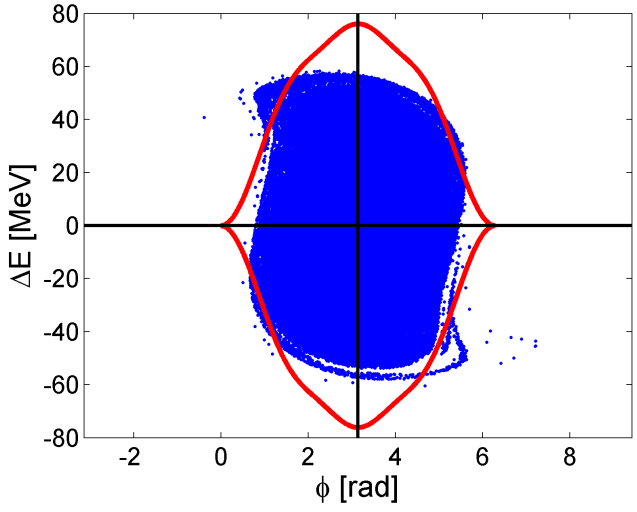

Figure 4.11: Initial particle distribution used in simulations for the SPS (blue points). The red line corresponds to the SPS RF bucket for double RF in BSM with $V_{200} = 1$ MV and $V_{800} = 0.25$ MV.

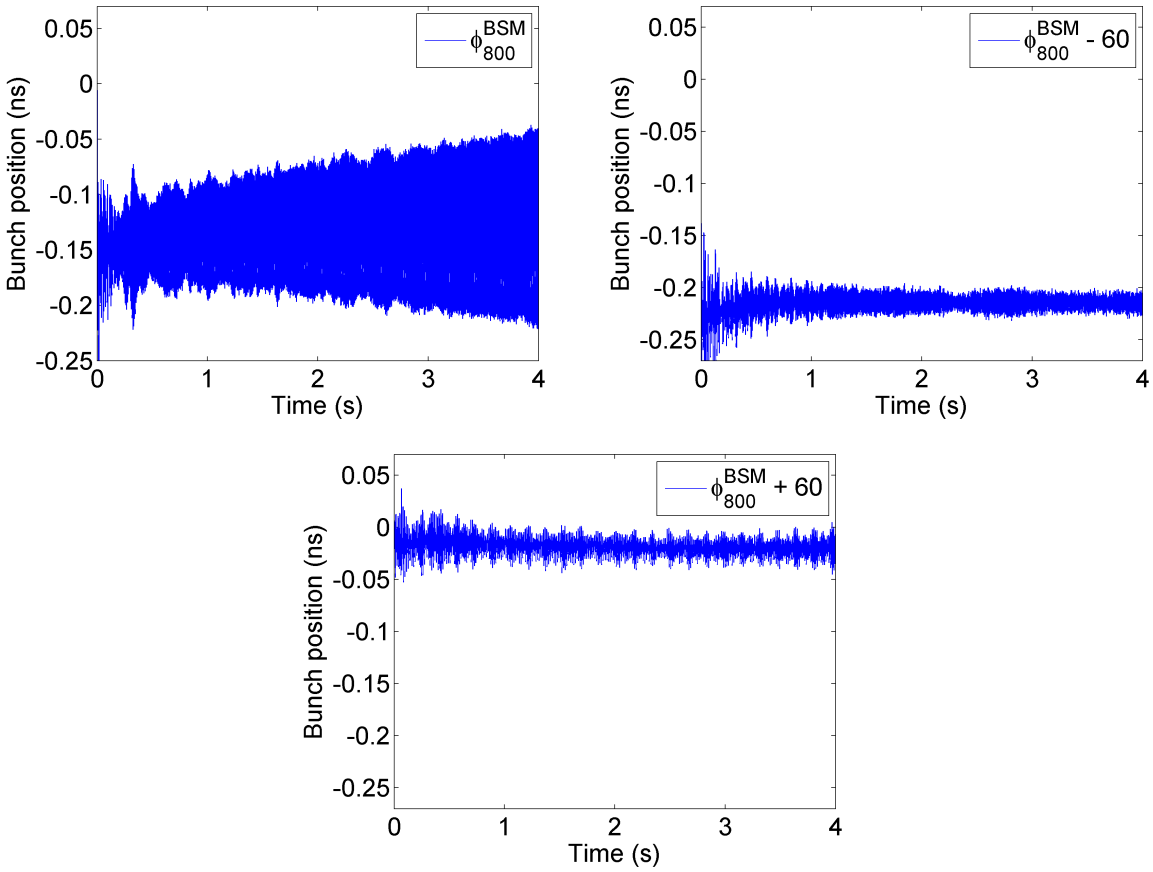

Figure 4.12: Evolution of the rms bunch position along the flat bottom for different values of ϕ_{800} obtained from simulations. $V_{200} = 1$ MV and $V_{800} = 0.25$ MV.

as well to characterize the instability in a double RF system. Their amplitude is shown in Fig. 4.10 as a function of the phase shift ϕ_{800} together with the measured quadrupole oscillation amplitude. In measurements phase loop was on and thus the dipole oscillations were damped. For the SPS impedance model used, the instability threshold is expected to be lower for the $m = 1$ (dipole) mode than for $m = 2$ (quadrupole) mode (see section 2.5) [44] and this is in fact what was observed in the simulations.

4.5 Effect of the synchrotron frequency distribution

The loss of Landau damping is a possible explanation of the unstable cases appearing for certain phase shifts between the two RF systems, when any resistive wake would drive instability for the modes that are not anymore damped. This argument is supported by the synchrotron frequency distributions (no intensity effects) shown in Fig. 4.13 for a single RF and for different values of ϕ_{800} and V_r in a double RF system.

Indeed, in the BSM with $V_r = 0.25$ (blue curve), particles in the tails of the measured bunches (their 2σ emittance is shown with a vertical line) may lose Landau damping, since the derivative

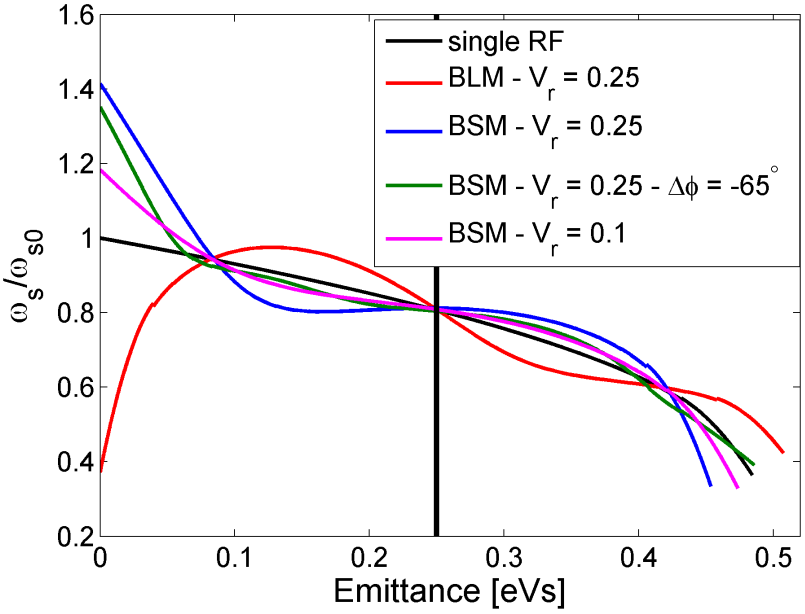

Figure 4.13: Synchrotron frequency distribution (no intensity effects) as a function of longitudinal emittance for different RF parameters. The bunch size in measurements is shown with a vertical line.

of the synchrotron frequency distribution as a function of action J (bunch emittance) $\omega_s^{'}(J)$ is zero at this point [10]. This behavior was in fact expected from the results of the previous Chapter (see section 3.5), where it was proven by simulations that for inductive impedance the regions of $\omega_s^{'}(J)$ cause a significant decrease in the loss of Landau damping threshold. Note that similar results were obtained in [12] for resistive impedance. On the other hand, the dependence of synchrotron frequency on bunch emittance is monotonic for the other cases shown in the plot, including the operational BSM with $V_r = 0.1$. Therefore, the threshold is expected to be higher and that is, in fact, the reason why the bunches were stable in the measurements and simulations for those cases. In the BLM (red curve) the bunch size in measurements is much bigger than the one that corresponds to the maximum of $\omega_s(J)$, which explains why the beam was also not stable.

It is interesting to note that the measured and simulated single bunch instabilities were explained in terms of the zero current synchrotron frequency distribution and not the one corresponding to the steady state situation (after the bunch filamentation). The reason for that is possibly the particular bunch distribution at the moment of injection (see Fig. 4.11), which, as was mentioned before, is not matched (see Fig. 4.14).

Consequently, the system is far from being in a steady state and the synchrotron frequencies of the particles are mainly determined by the external RF voltage applied through the RF cavities. Moreover, this modulation of the bunch profile can be a possible explanation of the relatively low single bunch threshold observed at the SPS flat bottom [41].

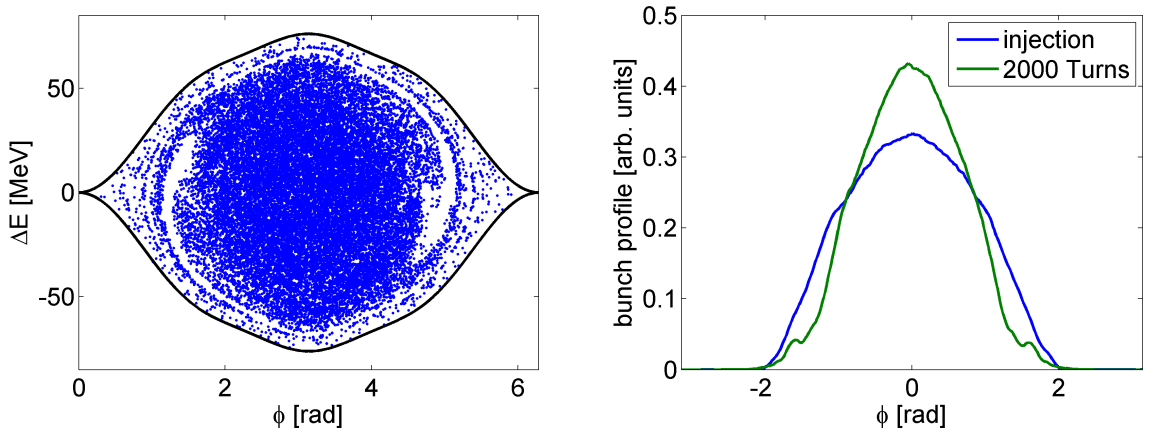

Figure 4.14: Particle distribution in the SPS longitudinal phase space (left) and its line density (right) after 2000 turns. The initial distribution is shown in Fig. 4.11. Note the high frequency pattern in the tails of the bunch. Here it is not very strong (compared to operation conditions) because of the low voltages, $V_{200} = 1$ MV and $V_{800} = 0.25$ MV. No intensity effects are included.

4.6 Conclusions

Thresholds of longitudinal single bunch instability versus the relative phase between the two RF systems were measured in the SPS for a voltage ratio of 0.25 and constant intensity of $\sim 1 \times 10^{11}$. They show that a phase shift between 50° and 100° (at 800 MHz) in both directions (relative to the BSM phase) stabilizes the otherwise unstable bunch. Particle simulations using the SPS impedance model show a good agreement with these measurements. This dependence on phase shift, in addition to the sensitivity to the voltage ratio V_r (also observed in measurements), indicates that the loss of Landau damping in the flat region of the synchrotron frequency distribution inside the bunch can be a possible explanation for the observed undamped oscillations. This gives both a justification and the limitation to the 800 MHz voltage amplitude used in operation for the LHC beams in the SPS ($V_{800} \approx V_{200}/10$).

Chapter 5

Beam loading and its effect on the controlled longitudinal emittance blow-up in the SPS double RF system

Presently, the use of a double RF system in the SPS operation (with a voltage ratio of $V_r = 0.1$, for reasons presented in the previous Chapter), is essential for the beam stability all along the cycle. However, for the LHC beams this is still not sufficient and instability is observed at the end of the ramp for intensity above the nominal. For that reason a controlled longitudinal emittance blow-up is applied to further increase the spread in the synchrotron frequencies inside the bunch and thus to enhance the effect of Landau damping. The emittance blow-up can be achieved by introducing a band-limited phase noise at some moment during acceleration. Measured variation of the final emittance along the batch can be explained by the effect of beam loading in a double harmonic RF system, leading to the modification of the synchrotron frequency distribution in each bunch.

5.1 Introduction

The nominal LHC beam in the SPS consists of four batches separated by gaps of 225 ns. Each batch contains 72 bunches spaced by 25 ns with $1.15{\times}10^{11}$ protons per bunch. This beam is accelerated by four 200 MHz traveling wave cavities, equipped with feed-forward and feed-back systems. However, a longitudinal coupled bunch instability observed at high energies appeared to be a limiting factor for the beam performance because of its low threshold of 2×10^{10} p/b. The nominal beam is finally stabilized by increased synchrotron frequency spread using a fourth harmonic RF system [10] and controlled longitudinal emittance blow-up. The latter is applied during the ramp by introducing band limited noise through the phase loop of the main RF system [71].

Since the controlled emittance blow-up is necessary to stabilize the nominal intensity beam, the final bunch length at flat top (and therefore emittance) is limited due to the injection into the 400 MHz buckets of the LHC. For that reason, bunch-to-bunch emittance variations along the batch can lead to particle losses in the LHC. Non-uniform emittance blow-up of high intensity beam in the SPS had been observed for the first time at the end of 2004 and previous studies [20, 32] suggested that this effect can be attributed to the bunch-to-bunch variation of the incoherent synchrotron frequency due to the residual beam loading. This analysis showed

that for the bunches at the edges of the batch the zero amplitude synchrotron frequency is lower than for those in the middle. Therefore, for a constant noise band along the batch one would expect the blow-up to be more effective for the bunches in the middle of the batch (optimum phasing). However, the experimental results show that bunches at the edges of the batch are blown-up more than those in the middle.

The present work extends the previous analysis by considering how the whole synchrotron frequency distribution is modified for the different bunches in the batch, defined mainly by the residual beam loading in the 200 MHz RF system. It will be shown that for the bunches at the edges of the batch, where the bigger synchronous phase variations due to beam loading occur, a significant change in the synchrotron frequency distribution appears, making larger blow-up possible.

5.2 Non-uniform emittance blow-up of the LHC beam

A stable beam with nominal intensity and emittance up to ∼0.6 eVs, obtained by controlled emittance blow-up, can be delivered to the LHC. The measurements presented here were done for a single batch with nominal intensity with aim to obtain maximum emittance (∼0.9 eVs) which might be requested for stability of higher intensity beams. The synchronous momentum and applied RF voltages (200 MHz and 800 MHz) for the SPS cycle during these measurements are shown in Fig. 5.1.

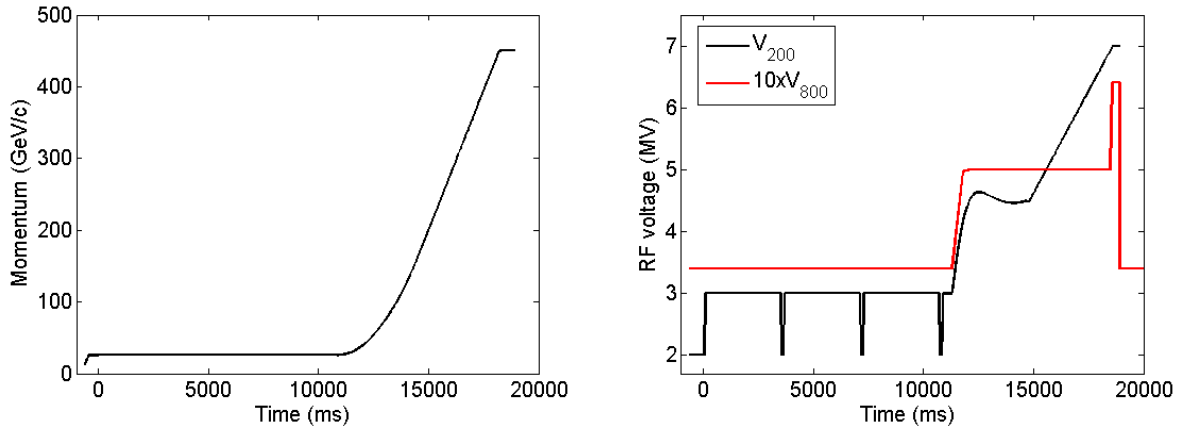

Figure 5.1: Particle momentum (left) and the 200 MHz and 800 MHz (×10) voltage programs along the cycle.

The band-limited noise [71] was introduced through the phase loop of the 200 MHz RF system at 185 GeV (14.8 s along the cycle) and lasted for 3 s. Figure 5.2 depicts the noise band and the synchrotron frequency spread (calculated for low intensity) during the cycle where the noise is applied. For nominal intensity beam the low intensity settings should be shifted down by ∼10 Hz due to an incoherent frequency shift (see section 2.4) produced by the SPS inductive impedance ImZ/n≃5 Ohm (before the serigraphy of the kickers [72]).

The bunch lengths were deduced from the acquired bunch profiles after correcting for the

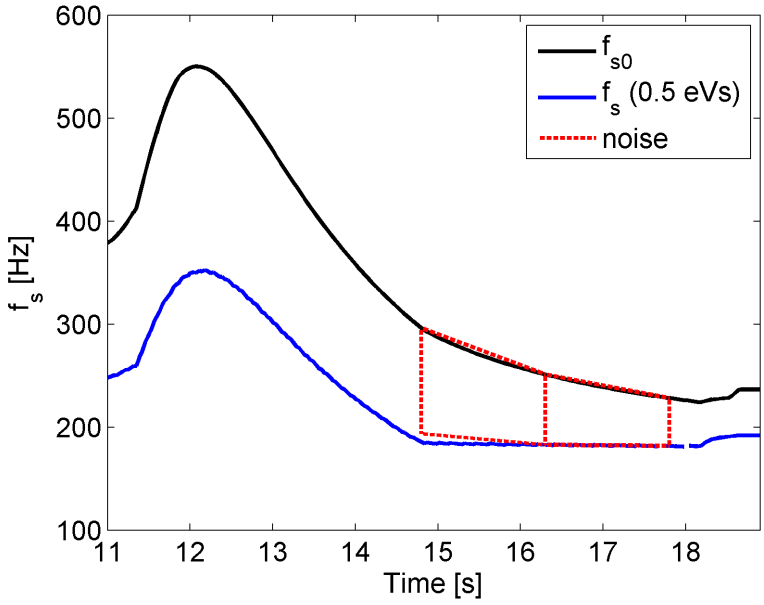

Figure 5.2: Noise excitation (red dashed lines) and synchrotron frequency spread at the end of the cycle, calculated for low intensities and for a bunch of 0.5 eVs.

pick-up and cable transfer function [68]. Figure 5.3 shows the results for two cycles where different noise bands were used. In both cases a single batch of 72 bunches spaced by 25 ns with 1.15×10^{11} particles per bunch was injected. The plots present the bunch lengths at different moments in the cycle. Both cases correspond to a successful blow-up in the sense that bunches were stable at the flat top. However, it is apparent that bigger blow-up occurs for the bunches at the beginning and the end of the batch. Furthermore, we can clearly see from the right plot, where the noise band was lifted up by 10 Hz compared to the left one, that the relative excitation of the bunches in the edges of the batch was less compared to those in the middle.

The bunch position variation along the batch Δt_n (found from the bunch profiles after a Gaussian fit), which corresponds in the stable situation to the synchronous phase displacement $\Delta\phi_s = \omega_{\rm rf}\Delta t$ ($\omega_{\rm rf} = 2\pi f_{\rm rf}$, $f_{\rm rf} = 200$ MHz), is shown in Fig. 5.4 for the same data as presented in Fig. 5.3. The antisymmetric pattern before the noise excitation (green line) indicates that the bunch positions are mainly defined by the beam loading in the main 200 MHz RF system, compensated by the feed-back and feed-forward systems. Indeed, the net effect of beam loading is expected to modify the stable phase ϕ_s along the batch, but in a different way; small displacement of the bunches at the head of the batch are increasing as more bunches entering the cavity until they reach a steady value. At flat top (blue line), where the bunch lengths become smaller, the effect of the 800 MHz beam loading (without feed-back and feed-forward systems) also becomes non-negligible and it modifies the previous pattern. The effects of beam loading are considered in more details in the next section.

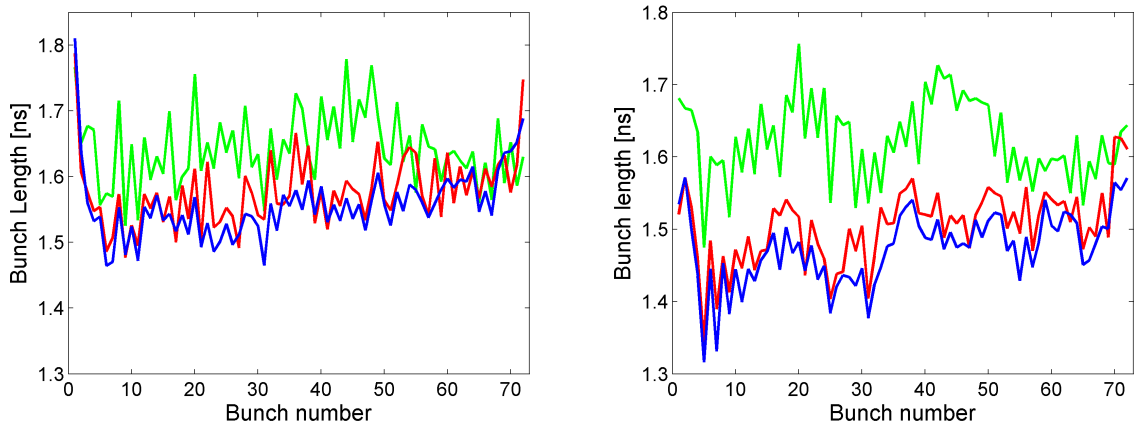

Figure 5.3: Measured bunch lengths before the controlled blow-up (green), just after (red) and at the SPS flat top (blue). The noise frequency band was shifted down ∼20 Hz (275-175 Hz) at the left plot and ∼10 Hz (285-185 Hz) at the right one with respect to the calculated values (low intensity).

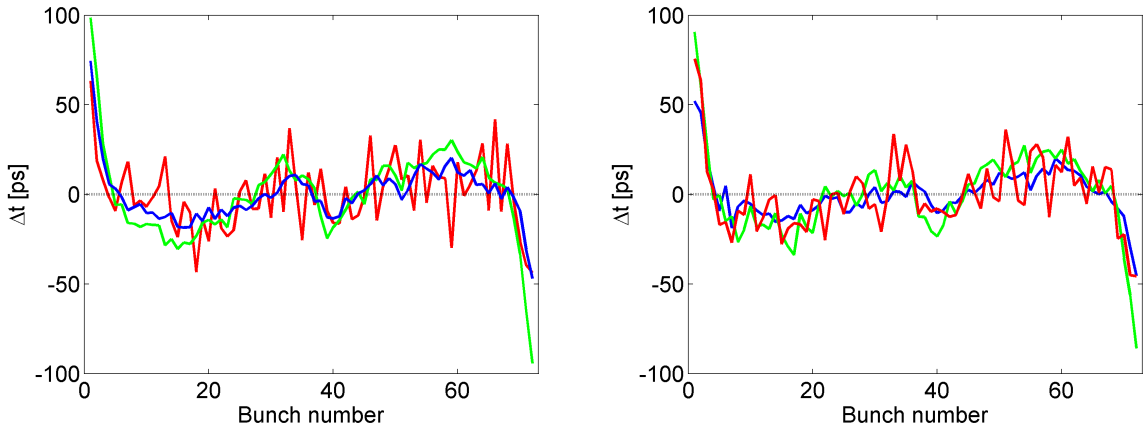

Figure 5.4: Longitudinal bunch position shift with respect to the equidistant positions along the batch. The data correspond to those of Fig. 5.3.

5.3 Beam loading in the traveling wave cavities

In accelerators, beam loading usually refers to the effects induced by the passage of the beam in the RF cavities. As such, it could be considered as one particular example of the more general problem of beam interaction with its surroundings, in this case the cavity fundamental impedance. The reason that beam loading needs a special treatment is that very often the RF cavities are the largest contributor to the total impedance of the ring (to have high voltage high impedance is needed), and consequently its effect leads to a significant power loss during the beam passage. Dedicated correction techniques are usually used to minimize these losses.

When a single particle is passing through a resonant cavity (considering only the fundamental

resonance) it will excite an additional field, which (see section 2.2) is proportional to the inverse Fourier transform of the impedance given by Eq. (2.86). For reasonably high Q value ($Q > 10$)

$$W(t) = \frac{\omega_{\mathrm{r}} R_{\mathrm{sh}}}{Q} e^{-\frac{\omega_{\mathrm{r}} t}{2Q}} \cos\left(\omega_{\mathrm{r}} t\right), \tag{5.1}$$

where R_{sh}, ω_{r} and Q are the shunt impedance, the resonance angular frequency and the quality factor of the cavity and t is the distance (in time) from the particle. Due to causality we have in Eq. (5.1) that $W(t) = 0$ for $t < 0$. The exponentially decaying induced field is plotted in Fig. 5.5. By superposition, the total field that a trailing particle will see is given by the combination of the latter with the generator driven waveform V_{rf} (see Fig. 5.5). Using linearity and superposition it can be proven that the initial particle itself "sees" one half of its own induced field [73]. This result is called *the fundamental theorem of beam loading.*

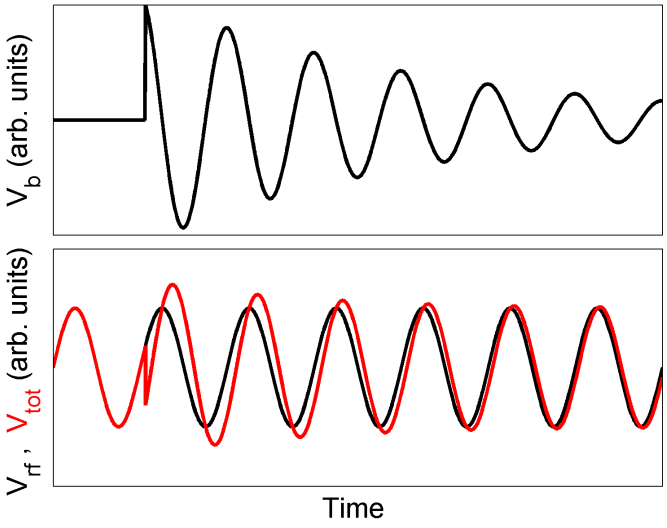

Figure 5.5: Induced (top), external (bottom, black curve) and total (bottom, red curve) voltages after single particle passage through a resonant cavity.

In the case of a single bunch with line density $\lambda(t)$, given for example from Eq. (2.107), the total induced voltage in the cavity V_b is given by the convolution of $\lambda(t)$ with $W(t)$, see Eq. (2.83). This voltage is illustrated in Fig. 5.6.

In vector representation the induced, external and total voltages are presented in Fig. 5.7, where the fundamental component of the beam current I_b defines the reference phase. The total voltage seen by the bunch is $\vec{V}_t = \vec{V}_{\mathrm{rf}} + \vec{V}_b/2$. In order to have a certain effective accelerating voltage ($V_t = |\vec{V}_t| \sin\phi_s$) applied to the bunch, the voltage delivered by the generator V_{rf} should be higher.

Whether the impact from one bunch to the following bunch is important, depends on the cavity time constant $T_f = 2Q/\omega_r$. Thus, if T_b is the distance between the two bunches, by the time the second bunch enters the cavity, the induced voltage V_b is reduced by a factor e^{-T_b/T_f}, see Eq. (5.1). The corresponding phase shift is $\psi = \omega_r T_b - 2\pi h_b$, where h_b is an integer indicating

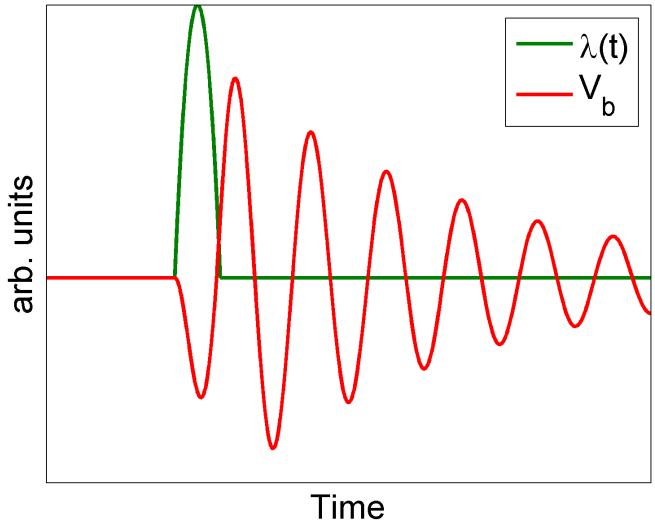

Figure 5.6: Single bunch passage through a resonant cavity. The line density $\lambda(t)$ is given by Eq. (2.107).

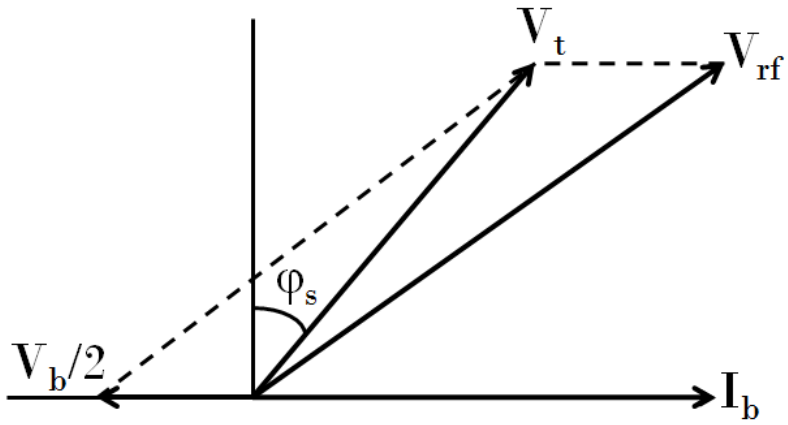

Figure 5.7: Vector diagram of a single-bunch passage through a resonant cavity.

the number of RF periods between the bunches. Finally, the total voltage V_t that the trailing bunch sees is

$$\vec{V}_t = \vec{V}_{\rm rf} + \vec{V}_b e^{-T_b/T_f} e^{i\psi} + \vec{V}_b/2. \tag{5.2}$$

Following ref. [31], the previous analysis can be extended to a multiple-bunch passage through the cavity.

In the case of a traveling wave (TW) cavity and for a repetitive train of many bunches, the fields excited by the previous bunch passages also propagate along the structure. If the incoming bunches (with velocity v_p) are synchronized with the traveling wave, i.e. $v_p = v_\varphi$ (v_φ

is the phase velocity of the wave) then the induced field is simply proportional to the distance along the cavity. However, if synchronization is not perfect an additional phase slippage occurs, $\theta = \omega t - k_z z$, where $z = v_p t$ and k_z is the wave propagation constant. Expanding θ to a first order around the synchronous point ($\omega = \omega_r, k_z = k_{z0}$), for which $\theta_0 = \omega_r t - k_{z0} z = 0$, one obtains

$$\theta = \omega t - k_z z = (\omega_r + \Delta\omega)\frac{z}{v_p} - (k_{z0} + \Delta k_z)z = \frac{\Delta\omega}{v_g}\left(\frac{v_g}{v_p} - 1\right)z, \tag{5.3}$$

where the group velocity $v_g = \Delta\omega/\Delta k_z$ was introduced. Since in the traveling wave cavities the energy transfer from cell to cell is much slower than the bunch velocity, i.e. $v_g \ll v_p$ the previous equation can be written as

$$\theta = -\frac{\Delta\omega}{v_g}z = -\frac{\omega - \omega_r}{v_g}z. \tag{5.4}$$

Defining also the angle τ_b as the total phase slip between the traveling wave and the bunch along the cavity

$$\tau_b = \frac{L}{v_g}(\omega - \omega_r), \tag{5.5}$$

one finally has

$$\theta = -\frac{\tau_b}{L}z, \tag{5.6}$$

where L is the total length of the structure.

Due to superposition the decelerating electric field E_z (induced by the beam passage) at distance z from the cavity entrance is proportional to the integral [28]:

$$E_z \propto \int_0^z e^{i\theta}dz = \frac{1 - e^{-i\frac{\tau_b}{L}z}}{i\tau_b/L}. \tag{5.7}$$

The total induced voltage seen by the beam is obtained by integrating E_z along the structure:

$$V_b = \int_0^L E_z dz \propto \int_0^L \frac{1 - e^{-i\frac{\tau_b}{L}z}}{i\tau_b/L}dz, \tag{5.8}$$

which finally gives [28]:

$$V_b = -I_b R_2 \frac{L^2}{8}\left[\left(\frac{\sin\frac{\tau_b}{2}}{\frac{\tau_b}{2}}\right)^2 - i2\frac{\tau_b - \sin\tau_b}{\tau_b^2}\right], \tag{5.9}$$

where the proportionality factor R_2 is the series impedance of the traveling wave cavity in Ω/m^2 defined in [28] as a characteristic of the structure.

Based on the last equation, the beam loading impedance can be defined as

$$Z_b = \frac{V_b}{I_b} = -\frac{L^2 R_2}{8}\left[\left(\frac{\sin\frac{\tau_b}{2}}{\frac{\tau_b}{2}}\right)^2 - i2\frac{\tau_b - \sin\tau_b}{\tau_b^2}\right]. \tag{5.10}$$

The real and imaginary part of Z_b for the SPS 200 MHz TW cavity with 4 sections (short, see Table 5.1) are plotted in Fig. 5.8.

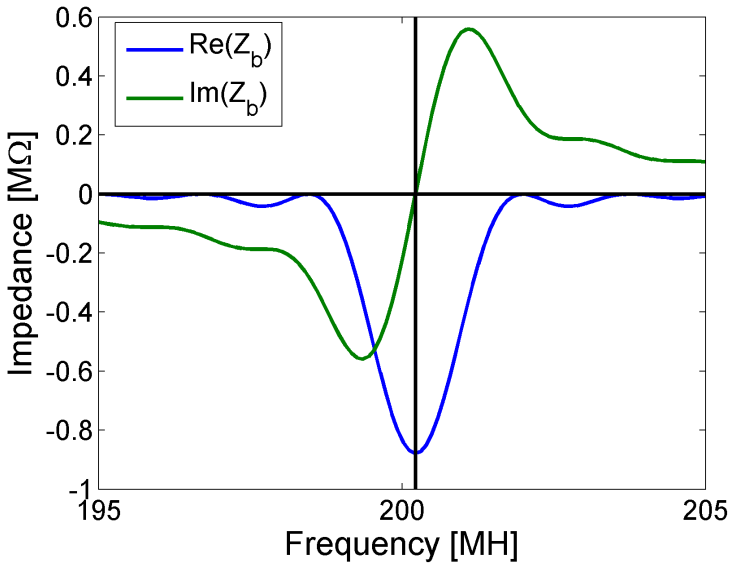

Figure 5.8: Beam loading impedance as a function of frequency for an SPS 200 MHz RF TW cavity of 4 sections (short) and parameters presented in Table 5.1.

Table 5.1: Parameters of the TW cavities (2 of each type)

	200 MHz Long	**200 MHz Short**	**800 MHz**
Centre frequency f_r	200.222 MHz	200.222 MHz	800.888 MHz
Interaction length L	20.196 m	16.11 m	3.46 m
Series impedance R_2	27.1 kΩ/m^2	27.1 kΩ/m^2	647 kΩ/m^2
Filling time L/v_g	0.712 μs	0.568 μs	0.330 μs
Beam loading impedance $L^2R_2/8$	1.38 MΩ	0.879 MΩ	0.968 MΩ

From the last equation it is also possible to find the phase ϕ of the induced voltage V_b with respect to the beam current I_b, known as beam loading angle.

$$\tan\phi = \frac{\mathrm{Im}(Z_b)}{\mathrm{Re}(Z_b)} = \frac{-2(\tau_b - \sin\tau_b)/\tau_b^2}{\left(\frac{\sin\tau_b/2}{\tau_b/2}\right)^2} = \frac{(\tau_b - \sin\tau_b)}{2\sin^2\frac{\tau_b}{2}}, \tag{5.11}$$

which for small values of τ_b ($\tau_b < 20°$) can be approximated with

$$\tan\phi \approx \frac{(\tau_b - \tau_b + \tau_b^3/3!)}{2(\tau_b/2)^2} = -\tau_b/3 \Longleftrightarrow \phi \approx -\tau_b/3. \tag{5.12}$$

Therefore, the vector diagram in the case of a TW RF cavity has to be modified with respect to the one presented in Fig. 5.7 by introducing the beam loading angle as shown in Fig. 5.9. Note that from there on V_b indicates the total induced voltage in the cavity.

This impedance can now be used to calculate the total voltage induced in a TW cavity after the passage of a bunch train by multiplying Z_b with the beam spectrum and taking the inverse Fourier transform. The case of a single batch of the nominal LHC beam passing through the

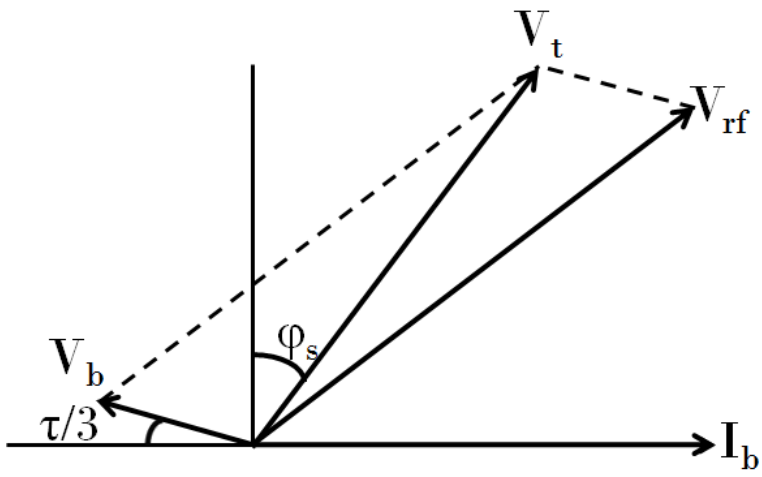

Figure 5.9: Vector diagram of a single bunch passage in a TW cavity.

200 MHz TW RF system is presented in Fig. 5.10. This batch consists of 72 Gaussian bunches with length of 1.7 ns and intensity 1.15×10^{11} p/b. The impedance of the 200 MHz RF system was calculated from the parameters presented in Table 5.1.

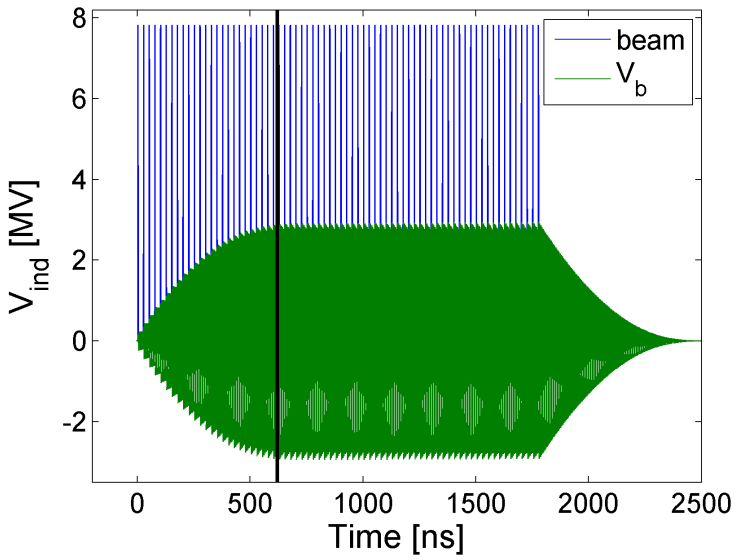

Figure 5.10: Induced voltage (green) in the 200 MHz TW RF system by a single LHC batch of 25 ns beam (blue). Gaussian bunches with 1.15×10^{11} p were assumed. The zero on the horizontal axis shows the first bunch of the batch. The vertical line indicates the filling time τ_f of the RF system.

When the head of the batch enters the cavity, the beam loading voltage rises during the filling time $\tau_f \approx 620$ ns (transient beam loading state) until it reaches its steady state value

$V_b \approx 3$ MV. The vector sum of the latter with the voltage applied by the RF generator V_{rf} gives the total voltage seen by the beam. Currently, for the intensity of 1.15×10^{11} p/b, the maximum available RF voltage is around 7.5 MV. Therefore, it is necessary to apply dedicated techniques in order to minimize the effect of beam loading.

At this point it is useful to introduce also the forward impedance [28]

$$Z_{\mathrm{rf}} = \frac{V_{\mathrm{rf}}}{I_g} = L\sqrt{\frac{Z_0 R_2}{2}}\left(\frac{\sin \tau_b/2}{\tau_b/2}\right), \tag{5.13}$$

where I_g is the generator current and Z_0 is the characteristic impedance of the RF chain (50 Ω). This impedance is plotted in Fig. 5.11 for the same cavity parameters as in Fig. 5.8.

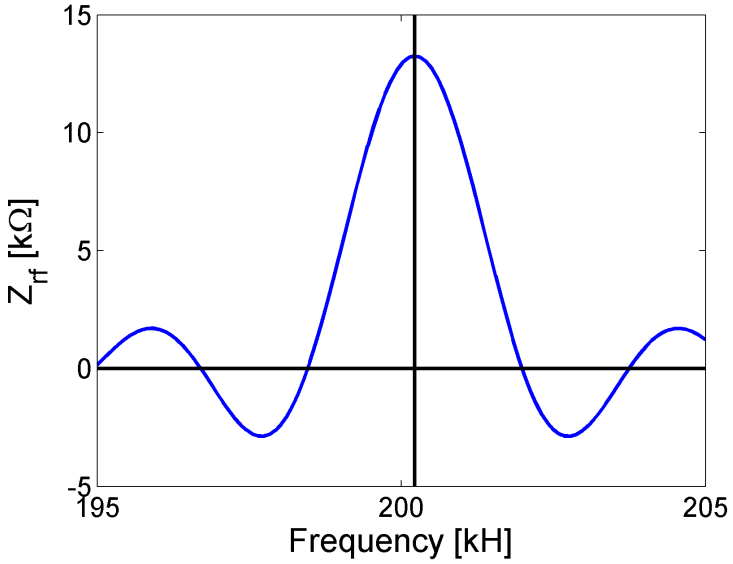

Figure 5.11: Forward impedance as a function of frequency for an SPS 200 MHz RF TW cavity of 4 sections (short) and parameters presented in Table 5.1.

Comparing Z_b and Z_{rf} from Eqs. (5.10) and (5.13) one can see that, up to a scaling factor, their real parts are the same. However, since Z_{rf} is real, the imaginary parts are completely different. This makes the compensation of beam loading with feed-back and feed-forward systems more difficult as compared to the case of standing wave cavities, where Z_b and Z_{rf} are identical.

5.4 Beam loading compensation

In order to reduce the beam loading impedance Z_b, each SPS 200 MHz TW cavity is equipped with a dedicated feed-forward (FF) system [74]. The beam current I_b is measured with a pick-up and then is filtered by the transfer function H_{fwd}. Finally, the output is subtracted from the generator current to compensate for the beam loading in the cavity.

Further compensation is achieved by the RF feed-back (FB), which is again installed in each cavity since 1983 [75]. In that case, the voltage sensed by the beam in each cell of the cavity

is measured with a loop. After addition of these signals (delayed by the corresponding time of flight of the particle i.e. different delay for each loop) we get the total voltage seen by the beam. This signal is filtered by the feed-back transfer function H_{back} and re-injected into the cavity with the proper phase via the power generator.

Finally, the achieved impedance reduction is obtained as the product of the reductions obtained separately by the FF and FB. Therefore, according to [74], the beam loading impedance after compensation Z_{bc} becomes

$$Z_{\text{bc}} = \frac{Z_b - H_{\text{FF}} Z_{\text{rf}}}{1 + H_{\text{FB}} Z_{\text{rf}}}. \tag{5.14}$$

The above formula was used to calculate the remaining (with FF and FB in operation) induced voltage in the 200 MHz RF system and an example for the same beam parameters as before is shown in Fig. 5.12.

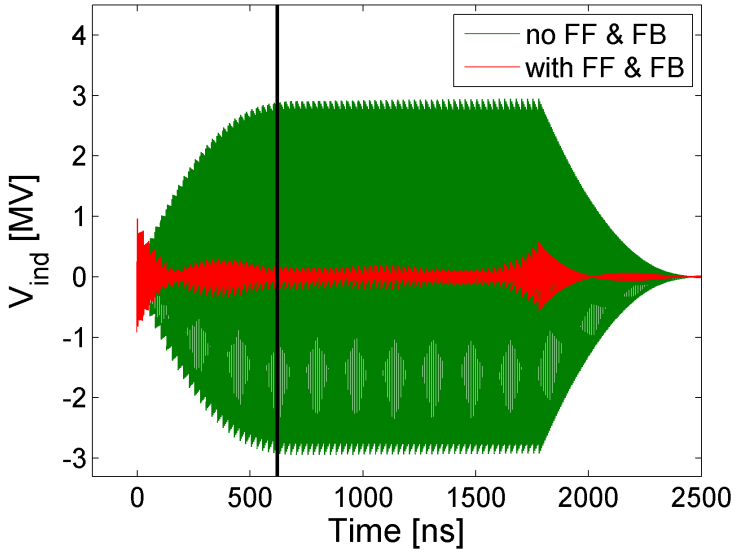

Figure 5.12: Induced voltage in the 200 MHz TW RF system with and without beam loading compensation by FF and FB. The beam parameters are the same as in Fig. 5.10.

In Fig. 5.12 one can see a significant decrease in V_b which is essential for acceleration of a stable beam in the SPS without losses. However, the remaining effect of the stable phase variation along the batch is still important and especially for a double RF system operation the controlled longitudinal emittance blow-up is analyzed below.

5.5 Beam loading in the SPS 200 MHz RF system

In section 5.3 the voltage V_b induced due to beam loading in a TW RF system was calculated. Based on these calculations, and the fact that the beam loading angle $\tau_b/3$ is defined only by Z_b, one can also calculate the variation of the synchronous phase $\Delta\phi_s$ along the batch. This can be illustrated schematically in the vector diagram of Fig. 5.13, where the black arrows present the steady state while the red ones show the transient beam loading case.

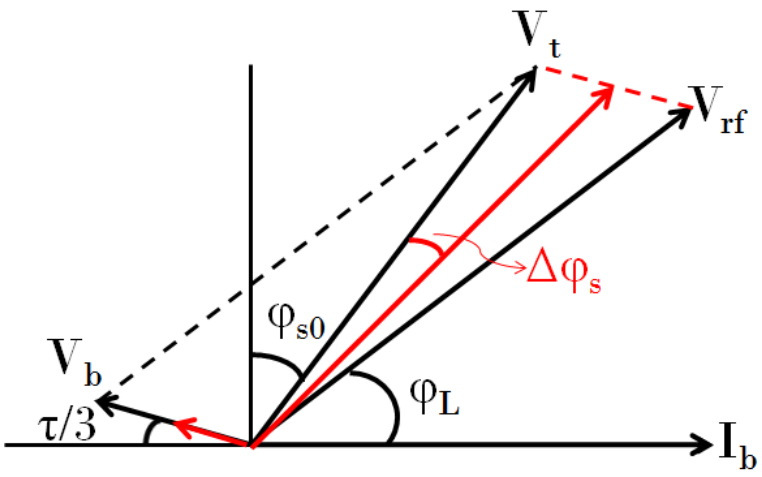

Figure 5.13: Vector diagram of the transient beam loading (red vectors). The black vectors present the steady state.

Before the beam enters the cavity, $V_b = 0$ and so $\vec{V}_t = \vec{V}_{\rm rf}$. While more and more bunches enter the cavity, the amplitude of V_b is increasing and so $\vec{V}_t$ moves along the red dashed line in Fig. 5.13 until ϕ_s reaches its steady state value, ϕ_{s0}. Assuming a constant $\vec{V}_{\rm rf}$ provided by the RF generator, with amplitude and phase shown in the diagram, one can obtain

$$\tan(\phi_{s0} + \Delta\phi_s) = \frac{V_{\rm rf}\cos\phi_L - V_b\cos\tau_b/3}{V_{\rm rf}\sin\phi_L + V_b\sin\tau_b/3}. \tag{5.15}$$

The phase shift $\Delta\phi_s$ calculated for the SPS 200 MHz RF system (all 4 cavities), with parameters presented in Table 5.1 are shown in Fig. 5.14. For all the calculations below, the same beam and machine parameters as those in Fig.5.10 were assumed, to be comparable with the measurements before the controlled emittance blow-up (see section 5.2). For this beam the DC beam current is 0.74 A, while the 200 MHz Fourier component (Gaussian line density) would be around 1.30 A. Note that the convention of $\Delta\phi_s > 0$ (from Fig. 5.13) for clockwise rotations is assumed below.

Once $\Delta\phi_s$ is known, the total voltage V_t can be found from

$$V_t = \frac{V_{\rm rf}\cos\phi_L - V_b\cos\tau_b/3}{\sin(\phi_{s0} + \Delta\phi_s)}. \tag{5.16}$$

However, as was mentioned in the previous section, in the 200 MHz RF system the 4 TW cavities (2 short and 2 long) are equipped with a FF and a one turn FB systems which compensate the beam loading effect [74] by modifying the impedance Z_b, see Eq. (5.14). Therefore, V_b will be significantly reduced as shown in Fig. 5.12. The beam loading angle τ_b^* will be slightly different from the previous τ_b, since now it is defined by $Z_{\rm bc}$. Here we assume that FF and FB are perfectly adjusted for the bunches in the middle of the batch and this corresponds to the steady state (black vectors in the diagram in Fig. 5.13). For those bunches in the middle the following relation can be written

$$V_t^{\rm ss}\sin\phi_{s0} = \frac{dp_s}{dt}T_{\rm rev}, \tag{5.17}$$

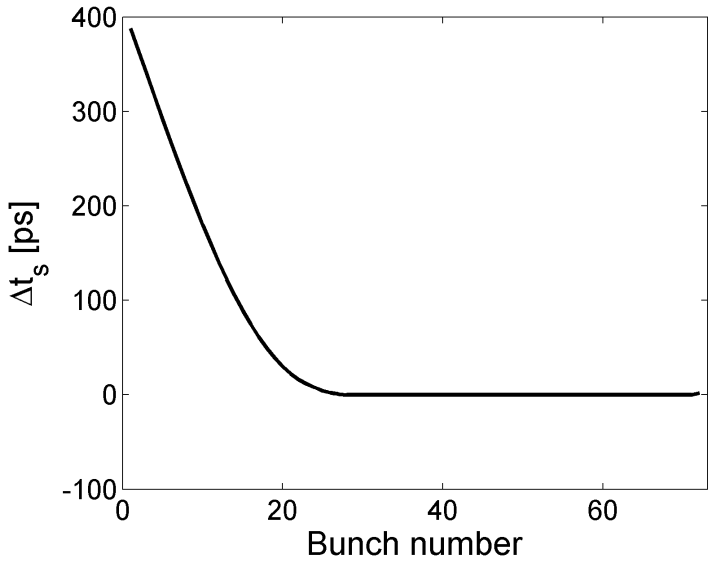

Figure 5.14: Synchronous phase variation (in ps) along one batch due to beam loading in the 200 MHz TW RF system. The beam parameters are the same as in Fig. 5.10.

where p_s and V_t^{ss} are the synchronous momentum and the RF voltage amplitude, programed along the cycle. Therefore, at the moment before the controlled emittance blow-up is applied (green traces in Figs. 5.3 and 5.4) one has

$$\sin\phi_{s0} = \frac{1.79}{4.5} \Leftrightarrow \phi_{s0} = 23.4^{\circ}. \tag{5.18}$$

Furthermore, from the calculated V_b after the beam loading compensation by FF and FB, one can find the induced voltage at the center of each bunch, see Fig. 5.15.

It is straight forward to calculate $\vec{V}_{\mathrm{rf}}$ from the vector diagram in Fig. 5.13 for the bunches in the middle of the batch

$$\tan\phi_L = \frac{V_t^{\mathrm{ss}}\cos\phi_{s0} - V_b^{\mathrm{ss}}\sin\tau_b^*}{V_t^{\mathrm{ss}}\sin\phi_{s0} + V_b^{\mathrm{ss}}\cos\tau_b^*} \tag{5.19}$$

$$V_{\mathrm{rf}} = \frac{V_t^{\mathrm{ss}}\sin\phi_{s0} + V_b^{\mathrm{ss}}\cos\tau_b^*}{\cos\phi_L}, \tag{5.20}$$

where V_b^{ss} is used to denote the induced voltage at the steady state (bunches in the middle of the batch). Since the constant $\vec{V}_{\mathrm{rf}}$ is known, the bunch position variations $\Delta\phi_s$ along the batch in the presence of FF and FB systems can be calculated from Eq. (5.15) and the results are presented in Fig. 5.16.

5.6 Beam loading in the SPS 800 MHz RF system

In addition, in order to calculate the expected total shift of ϕ_s along the batch in operation, one needs to take into account also the beam loading in the 800 MHz RF system. In the SPS two

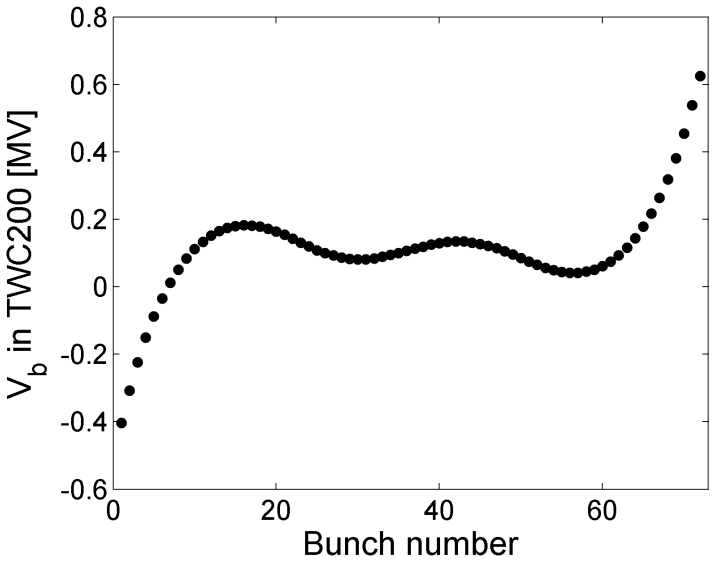

Figure 5.15: Calculated beam induced voltage in the 200 MHz RF system at the center of each bunch, just before the controlled emittance blow-up. The beam parameters are the same as those in Fig. 5.10.

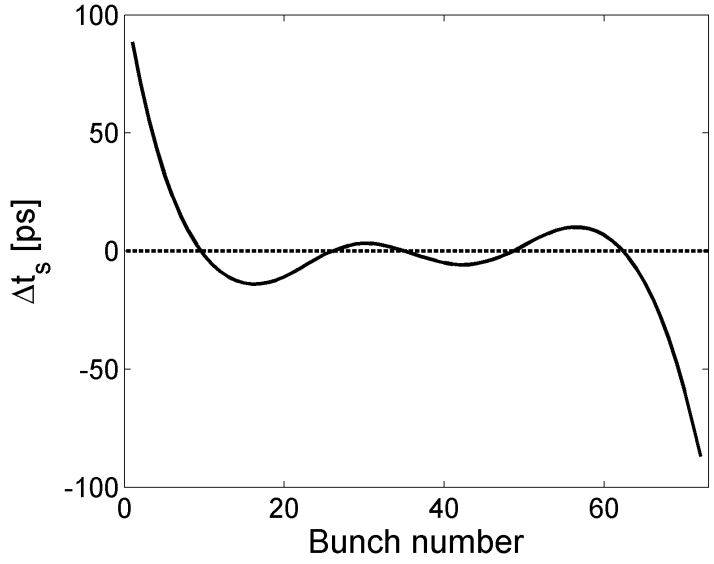

Figure 5.16: Residual Synchronous phase variation (in ps) along the batch after the beam loading compensation in the 200 MHz TW RF system by the FF and FB systems. The beam parameters are the same as in Fig.5.10.

800 MHz TW cavities are installed but until now only one was used in operation but without FF or FB systems (to be implemented in 2015). Figure 5.17 presents the calculated values of the induced voltage in the 800 MHz RF system (both cavities included) at the center of each bunch

(without taking into account the beam loading effect in the 200 MHz RF system), during ramp and just before the phase noise application. At this moment, the 800 MHz Fourier component of the beam current would be around 0.15 A (for the same beam parameters as in Fig 5.10)). The parameters of the cavities used in calculations are also presented in Table 5.1.

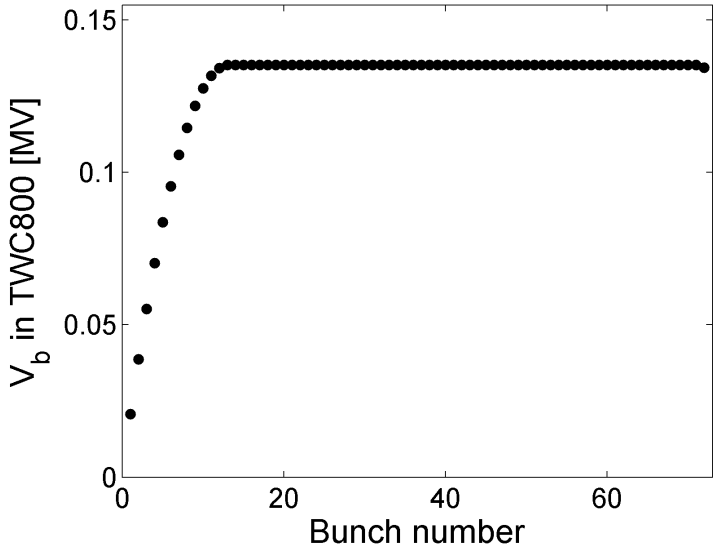

Figure 5.17: Calculated beam induced voltage in the 800 MHz RF system at the center of each bunch (without taking into account the beam loading effect in the 200 MHz RF system), during the ramp and just before the controlled emittance blow-up. The beam parameters are the same as those in Fig. 5.10.

The formalism described above (see the vector diagram of Fig. 5.13) can be also used to calculate the phase shift ($\Delta\phi_s^{800}$) along the batch due to the 800 MHz RF system. However, we need to take into account tha in operation the phase between the two RF systems is programmed in such way that no energy should be given to the synchronous particles from the 800 MHz RF component ($\phi_s = \phi_{s0}$). Note that here we consider the case when the phase between the two RF systems is established using measurements in the middle of the batch, i.e. V_t^{800} is aligned with respect to V_t^{200}. Finally, using Eqs. (5.15), (5.19) and (5.20) one can calculate $\Delta\phi_s^{800}$ for all the bunches inside the batch and the results cn be seen in Fig. 5.18.

The situation for $\Delta\phi_s^{800}$ is reversed when V_{rf}^{800}, and not V_{t}^{800}, is aligned with respect to V_t^{200}. That means that initially, when the first bunch enters the cavity, $\Delta\phi_s^{800} = 0$. While more bunches are passing through the cavity $\Delta\phi_s^{800}$ decreases ($\Delta\phi_s^{800} < 0$) until it reaches its steady state value ($\Delta\phi_s^{800} \approx -35$ ps, see Fig. 5.18). This is illustrated in the vector diagram in Fig. 5.19.

In that case, the phase and amplitude of the generator voltage $\vec{V}_{\mathrm{rf}}$ are known and thus $\vec{V}_t$ can be found from the following equations

$$\tan\Delta\phi_s^{800} = \frac{-V_b\cos\tau_b}{V_{\mathrm{rf}} + V_b\sin\tau_b} \qquad \textit{and} \qquad V_t = \frac{-V_b\cos\tau_b}{\sin\Delta\phi_s^{800}}. \tag{5.21}$$

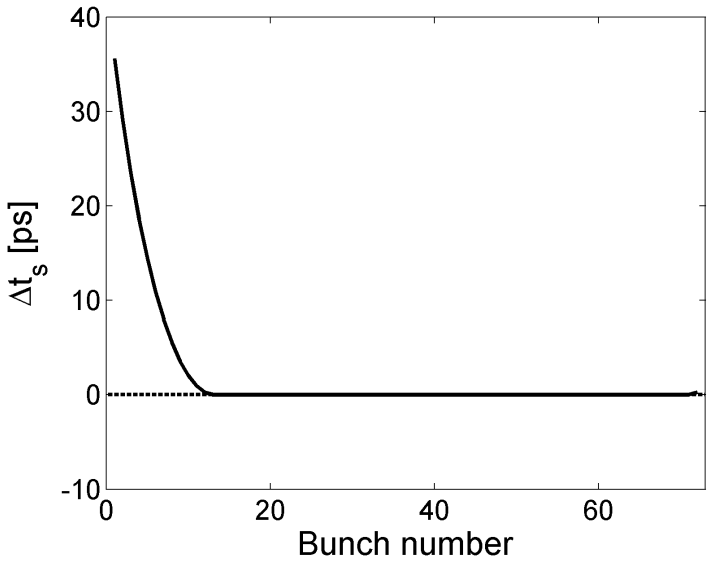

Figure 5.18: Synchronous phase variation (in ps) due to the beam loading in the 800 MHz TW RF system. The beam parameters are the same as in Fig.5.10.

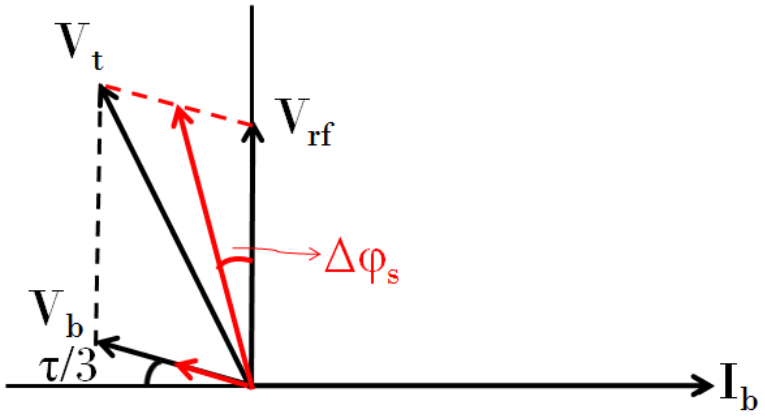

Figure 5.19: Vector diagram showing the beam loading voltage for the 800 MHz RF system when V_{rf}^{800} is aligned with respect to V_t^{200}. The steady state is presented with the black vectors while the transients are shown in red.

5.7 Beam loading effects on the synchronous phase

The phase shift variations $\Delta\phi_s^{200}$ and $\Delta\phi_s^{800}$ along the batch due to the 200 MHz and 800 MHz RF systems, respectively can be used to find the total phase shift, by taking into account that the vectors V_t^{200} and V_t^{800} (or V_{rf}^{800} in the other case) have a phase angle ϕ_{s0} for the steady state

(black vectors in Fig. 5.20). According to that the total phase shift $\Delta\phi_s$ can be derived from

$$\tan\Phi_s = \frac{V_t^{200}\sin\Phi^{200} + V^{800}\sin\Delta\phi^{800}}{V_t^{200}\cos\Phi^{200} + V_t^{800}\cos\Delta\phi^{800}} \tag{5.22}$$

where $\Phi_s = \phi_s + \Delta\phi_s$, ϕ_s is the synchronous phase of the total voltage for the steady state and $\Phi^{200} = \phi_{s0} + \Delta\phi_s^{200}$.

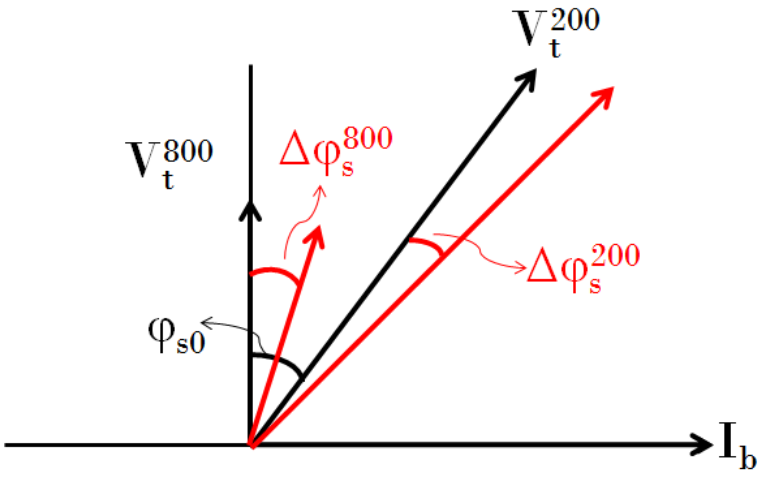

Figure 5.20: Vector diagram showing the beam loading voltage for both the 200 MHz and 800 MHz RF systems when V_t^{800} is aligned with respect to V_t^{200}. The steady state is presented with the black vectors while the transients are shown in red.

Using Eq. (5.22) we can calculate the variation of the synchronous phase $\Delta\phi_s$ which corresponds to the bunch position variation along the batch, just before the noise excitation (green trace in the plots of Fig. 5.4)). The results for both 200 MHz and 800 MHz RF systems are plotted in Fig. 5.21 (solid line). An example of measured bunch positions is also presented for comparison (dashed line).

One can see that this model can closely reproduce the measurements, indicating that the main cause of the bunch position variation is the induced voltage in the RF systems and in particular in the 200 MHz RF cavities. Note that similar results were obtained for the two different cases of the phasing between the RF systems. However, the remaining difference shows that there are other parameters that have not been taken into account in the model. On the one hand, a more realistic model of the impedance Z_{bc}, see Eq. (5.14), could be implemented, since above only real values of the transfer functions H_{FF} and H_{FB} were considered. On the other hand, additional sources of the longitudinal impedance in the ring should be included in the calculations, with the kickers impedance being the most significant. However, its broad-band nature will contribute more to the inductive part of the total impedance seen by the beam and less to the resistive part. Thus, Fig. 5.20 is expected to be similar, while the effect of this additional impedance will be apparent through the shift of the synchrotron frequency distribution inside the bunch.

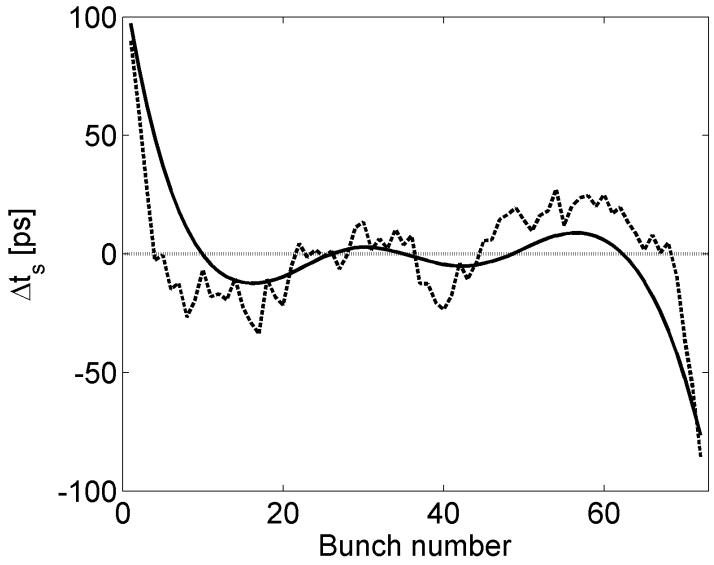

Figure 5.21: Bunch position variation (in ps) along the batch at the time in the cycle before the noise excitation. $V_{200} = 4.5$ MV and $V_{800} = 0.5$ MV. The beam parameters are the same as in Fig.5.10.

5.8 Effect of beam loading on the synchrotron frequency distribution

From the measured bunch position variations along the bunch, resulting from the effect of beam loading in SPS RF systems, we need to identify what is the actual phase between the two RF systems. The total external voltage seen by the synchronous particles of the bunches in the middle of the batch, considering both RF systems is

$$V_t = V_t^{200} \sin \phi_{s0} + V_t^{800} \sin(4\phi_{s0} + \Phi_2), \tag{5.23}$$

where Φ_2 is programmed during the cycle to $\Phi_2 = -4\phi_{s0} + \pi$ for the bunch shortening mode above transition and ϕ_{s0} is given by Eq. (5.17). A graphical representation of this situation, at the moment before the controlled emittance blow-up is applied, can be seen in Fig. 5.22. Note that at this moment the value of ϕ_{s0} is 23.4° (see Eq. (5.18)).

The induced voltage at the 200 MHz RF system is changing the synchronous phase by $\Delta\phi_s$. Equivalently, $\Delta\phi_s$ can be introduced as an additional phase shift between the two RF systems

$$V_t = V_t^{200} \sin \phi + V_t^{800} \sin(4\phi + \Phi_2 + \Delta\phi_2), \tag{5.24}$$

where $\Delta\phi_2 = 4\Delta\phi_s$. Due to the presence of the second RF system the synchronous phase changes by $\delta\phi_s$. Considering that for the bunches in the middle of the batch $V_t = V_t^{200} \sin \phi_{s0}$, one can write

$$V_t^{200} \sin \phi_{s0} = V_t^{200} \sin(\phi_{s0} + \delta\phi_s) + V_t^{800} \sin(4\phi_{s0} + 4\delta\phi_s - 4\phi_{s0} + \pi + 4\Delta\phi_s), \tag{5.25}$$

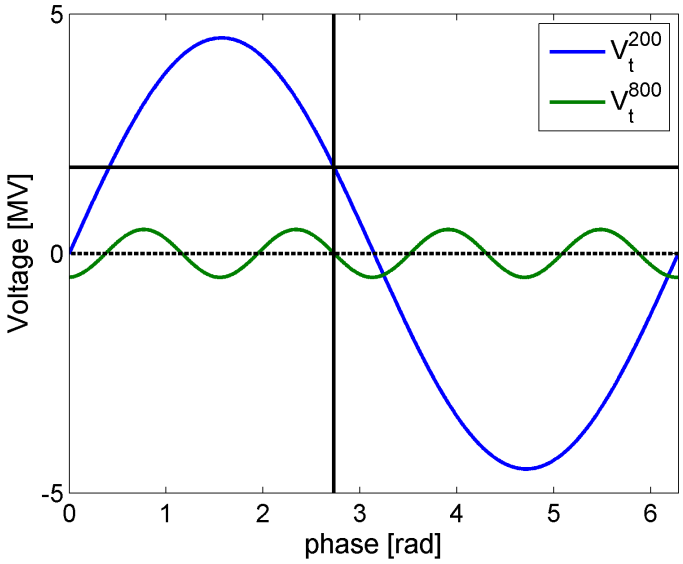

Figure 5.22: Voltage waveforms at the steady state (middle of the batch) just before the controlled emittance blow-up is applied. The vertical solid line shows the synchronous phase $\phi_{s0} = 23.4°$. Note that no energy gain is provided by the V_t^{800} since $\Phi_2 = -4\phi_{s0} + \pi$.

where the substitution $\Phi_2 = -4\phi_{s0} + \pi$ was also made. Assuming now small values for $\delta\phi_s$ and that the measured shift of the bunch positions $\Delta\phi_s^{\text{meas}}$ is given by the sum

$$\Delta\phi_s^{\text{meas}} = \Delta\phi_s + \delta\phi_s, \tag{5.26}$$

one has

$$0 = V_t^{200}\delta\phi_s \cos\phi_{s0} - V_t^{800}\sin(4\Delta\phi_s^{\text{meas}}). \tag{5.27}$$

Therefore,

$$\delta\phi_s = \frac{V_t^{800}\sin(4\Delta\phi_s^{\text{meas}})}{V_t^{200}\cos\phi_s}. \tag{5.28}$$

From Eqs. (5.26) and (5.28) we have

$$\Delta\phi_2 = 4\left(\Delta\phi_s^{\text{meas}} - \frac{V_t^{800}\sin(4\Delta\phi_s^{\text{meas}})}{V_t^{200}\cos\phi_s}\right), \tag{5.29}$$

which for small values of $\Delta\phi_s^{\text{meas}}$ can be simplified to

$$\Delta\phi_2 = 4\Delta\phi_s^{\text{meas}}\left(1 + 4\frac{V_t^{800}}{V_t^{200}(-\cos\phi_s)}\right) \tag{5.30}$$

This means that for the batch edges, where $\Delta t_{\text{meas}} \simeq 100$ ps (see plots in Fig. 5.4) we have $\Delta\phi_2 \simeq 40°$. Inserting this value into (5.24) we can calculate the synchrotron frequency distribution inside the bunch using for Φ_2 the programmed value. The results are plotted in Fig. 5.23 for $\Delta\phi_2 = 0, \pm 40°$. In the plot, the noise frequency bands were lifted up by 10 Hz

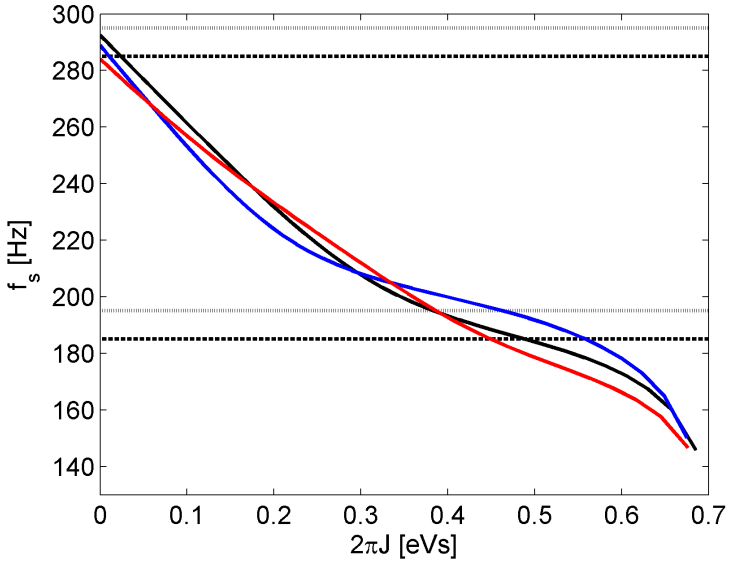

Figure 5.23: Synchrotron frequency as a function of action, normalized to emittance calculated for the voltage of Eq. (5.24) with $\Phi_2 = -4\phi_{s0} + \pi$ and $\Delta\phi_2 = 0, \pm 40°$, just before the controlled emittance blow-up is applied. The black curve corresponds to the bunch in the center of the batch (k=36), the blue to the first bunch (k=1) and the red to the last one (k=72). The dotted and dashed lines present the phase noise bands that were used for the controlled emittance blow-up.

(195-295 Hz and 185-285 Hz) compared to those used in operation (185-285 Hz and 175-275 Hz), since in these calculations the synchrotron frequency shift due to the SPS inductive impedance was not taken into account .

The blue curve in Fig. 5.23 shows that for the bunch in the head of the batch (with k=1), a flat region with $\omega'(J) \sim 0$ appears in the synchrotron frequency distribution, indicating that for fixed noise band the bunches in the head of the batch can be blown-up more (0.57 eVs, 0.59 eVs) than those at the center of the batch (k=36, 0.49 eVs, black curve). This explaines why in Fig. 5.3 the length of the first bunches in the batch is much higher than for those in the middle. On the other hand, the synchrotron frequency distribution is different for the end of the batch (k=72, red curve), which shows that this bunch is blown-up less (0.45 eVs, 0.465 eVs). The system is very sensitive to the calibration of the phase shift Φ_2 between the two RF systems, which is based on beam measurements (bunch shape or beam stability) [32] and we always have an offset which in general is not known. For that reason the synchrotron frequency distribution can vary significantly. Moreover, the the noise excitation is applied during the cycle for 3 s where the bunch parameters are changing. For a more accurate model we need to implement also the potential well distortion that occurs from other impedances and in particular the kickers. This impedance does not introduce a difference from bunch to bunch but still modifies the synchrotron frequency distribution. Furthermore, locking the phase of the voltage in the two RF systems by a measurement outside the batch can also affect significantly the results, while different moments during the acceleration when the controlled emittance blow-up is applied should be also studied.

5.9 Conclusions

Controlled longitudinal emittance blow-up together with the operation of a high harmonic RF system are essential for the LHC beam stabilization in the SPS. Measurements of bunch lengths at the flat top show that after the noise excitation a non-uniform emittance blow-up occurs. Taking into account the residual beam loading in the 200 MHz RF system (with FF and FB in operation) and the beam induced voltage in the 800 MHz RF system the observed variation of the bunch position along the batch can be closely reproduced. The bunch positions are mainly determined by the residual beam loading in the 200 MHz RF system. As a consequence, the synchrotron frequency distribution variation for bunches at different positions in the batch can explain the large variation in emittance along the batch for the applied phase noise band during the controlled emittance blow-up.

Chapter 6

Conclusions

Operation with a double RF system is essential for many accelerators in our days in order to increase beam stability, to change the bunch shape and perform various RF manipulations. In particular, regarding the beam stability, the bunch-lengthening (BL) mode is used more often (compared to the bunch-shortening (BS) mode) since in addition to the increased synchrotron frequency spread inside the bunch (more effective Landau damping) it reduces the peak line density and therefore reduces the local intensity effects. However, there are some cases in the hadron accelerators where the BL mode can not be used since it reduced the threshold of longitudinal beam instabilities, in comparison with the single RF system. This is also the situation in the operation of the CERN SPS as the LHC proton injector, where the fourth harmonic RF system is used in BS mode in addition to the main RF system. In fact the double RF system operation in the SPS is one of the essential means, together with the controlled longitudinal emittance blow-up, and the new Q20 optics, to significantly increase the longitudinal instability thresholds (single and multi-bunch) and deliver a good quality beam for the LHC. However, for the HL-LHC and LIU projects higher beam intensities are required. After commissioning the LINAC4 and upgrading the PSB and the PS, the main performance limitations of the LHC injector complex are beam instabilities and high intensity effects in the SPS.

Motivated by the longitudinal stability issues in the CERN SPS, the aim of this dissertation has been to fully exploit the benefits and the limitations of a double harmonic RF system. Consequently, it is based primarily on the beam and machine parameters of the SPS during its operation as the injector of the LHC, although most of the results can be used in other proton accelerators as well.

The main achievement of this work is the explanation, either by analytical methods or macroparticle simulations, of the following important experimental facts, which are limiting the present and the future operation of the SPS

- The low intensity threshold of the longitudinal single bunch instability in a double RF system operating in the BL mode.
- The low intensity threshold of the longitudinal single bunch instability in the BS mode for a high voltage ratio between the two RF systems ($V_2/V_1 \geq 1/4$ for the SPS).
- The dependence of the single bunch instability threshold on the relative phase Φ_2 between the two RF systems.
- The non-uniform controlled longitudinal emittance blow-up at high intensities in a double RF system, resulting to a bunch to bunch variation along the batch.

Initially the single bunch longitudinal stability with respect to the synchrotron frequency distribution inside the bunch $\omega_s(J)$ was addressed for a second harmonic RF system ($h_2/h_1 = 2$)

in the presence of reactive impedance. The study was restrained to a stationary case since no acceleration was assumed. In particular, the loss of Landau damping threshold was found both from simulations and calculations after taking into account the potential-well distortion. The semi-analytical approach was based on finding the discrete Van Kampen mode (coherent mode without Landau damping) by solving numerically the linearized Vlasov equation [12, 13]. The particle simulations were performed using a numerical tracking code written in Matlab for the purpose of this study.

Both approaches showed that for the BL mode and an inductive impedance there is a critical value of the longitudinal emittance (or action J), above which the Landau damping threshold decreases rapidly to zero. This critical value corresponds to the region where $\omega_s^{'}(J) = 0$. A phase shift between the two RF components of more than 15° can help to increase the threshold but the flatness of the bunches is lost. These results are able to explain observations during the $p\bar{p}$ operation of the SPS [14, 15] and to verify the beam transfer function (BTF) measurements in BL mode in the SPS, where large amplitude coherent response was observed at frequencies corresponding to that critical region [60].

For a capacitive impedance (or space charge) the thresholds are either dramatically increasing or can not be found analytically. This is in agreement with the theoretical prediction in [16], where it was proved that for the space charge impedance above transition, a bunch in a steady state is always stable.

The analysis was applied to different harmonic ratios $h_2/h_1 = n$ between the two RF systems, by keeping the same voltage ratio $V_1/V_2 = n$. It has been shown that although higher n provides larger synchrotron frequency spread, the critical region moves closer to the bunch center, and this is limiting the bunch size that can be used in stable operation. It was also shown that, in the BS mode with $n \geq 3$ the regions where $\omega_s^{'}(J) = 0$ are also appearing as local extrema. Consequently, for emittances larger than those values, the threshold of the loss of Landau damping is significantly decreased.

These results agree very well with the observations from the SPS operation with the 4^{th} harmonic RF system ($n = 4$). Measurements of the longitudinal single bunch instability threshold versus the relative phase between the two RF systems, performed in the SPS flat bottom during one machine development (MD) session, have been presented. The voltage ratio of $V_2/V_1 = 1/4$ and a constant intensity per bunch of $\sim 1 \times 10^{11}$ was used. The analysis of the measurements showed that the bunch is longitudinally unstable both in the BS and the BL modes. Note that these phases are defined in the machine by a beam based calibration method, performed at the beginning of each operational run. By scanning the phase shift between the two RF systems a region where the bunches are stabilized was identified. This phase region is found to be between 50° and 100° (at 800 MHz) with respect to the BS mode. Particle simulations using the longitudinal beam dynamics simulation program ESME (version es2009_4) [17] were performed to verify the measured results. The current SPS impedance model consisting of the 200 MHz (long and short types) and 800 MHz traveling wave RF systems, one higher order mode (HOM) of the 200 MHz RF system [69] and the impedance of 16 kickers (the latter approximated by a broad-band resonator with Q=1) was included in the simulations. A very good agreement with the measurements was obtained since the same stable phase region was reproduced. Decreasing the voltage ratio to $V_2/V_1 = 1/10$ (the value that is currently used in operation) resulted in

stabilizing the bunch in the BS mode, a result that was again verified from simulations.

The dependence on the phase between the two RF systems, in addition to the sensitivity on the voltage ratio, indicates that the loss of Landau damping in the flat region of the synchrotron frequency distribution inside the bunch can be a possible explanation for the undamped oscillations observed in the measurements. For example, in the BS mode with $V_2/V_1 = 1/4$, the size of the bunches used in the measurements (and the simulations) is such that many particles are in the region where $\omega_s^{'}(J) = 0$ and Landau damping is lost. By decreasing the ratio to $V_2/V_1 = 1/10$ the synchrotron frequency distribution becomes monotonic for the BS mode and therefore the bunch is stable. This fact gives both a justification and the limitation to the 800 MHz voltage amplitude used in operation for the LHC beams in the SPS.

Even using the fourth harmonic RF system in the BS mode with a voltage ratio of $V_2/V_1 = 1/10$, proton beams of the LHC type in the SPS are still unstable at the end of the acceleration ramp. For that reason a controlled longitudinal emittance blow-up is also applied in routine operation, during the second part of the ramp, to increase further the spread in the synchrotron frequencies inside the bunch and thus to enhance the effect of Landau damping. This is achieved by introducing a band-limited phase noise in the 200 MHz RF system. However, the controlled emittance blow-up has its own limitations. Indeed, analysis of measured bunch profiles shows that after the noise excitation the bunch length distribution along each batch at the flat top has a non-uniform structure. This effect becomes more pronounced by increasing the amplitude of the phase noise (to obtain larger emittances) and might prove to be a limitation for injection into the LHC 400 MHz RF buckets, when for stability at higher beam intensities a larger emittance will be requested.

It has been proved during this thesis, that the measured variations of the final emittance along the batch can be explained by the modification of the synchrotron frequency distribution due to the effect of beam loading in the SPS double harmonic RF system. In particular, by taking into account the residual beam loading in the 200 MHz traveling wave RF cavities (equipped with feed-back and feed-forward systems) and the beam loading voltage in the 800 MHz traveling wave RF cavities, the observed variation of the bunch position along the batch was closely reproduced. The synchrotron frequency distribution calculated for bunches at different positions in the batch using the total voltage derived from this model can explain the large variation in emittance along the batch for the applied phase noise band.

The effect of the residual beam loading in the 200 MHz RF system resulting in a non-uniform emittance blow-up will be significantly reduced after the redesign of the existing beam control around the 200 MHz cavities (including longitudinal damper and feedback coupled on cavities of different length). This is a part of the approved LIU project at CERN and will be available in operation in 2018 [76]. In addition, a feed-back system around the 800 MHz RF system is also going to be installed and become operational during the 2015 run [77]. Thus, the effect of beam loading in this RF system will be also reduced and a better control of the phase Φ_2 between the two RF systems will be possible, allowing for a better beam stability of the short bunches at the SPS flat top.

Bibliography

[1] L. Palumbo and V. G. Vaccaro. Wake fields, impedances and Green's function. (CERN Accelerator School), Sep 1985.

[2] A. W. Chao. *Physics of collective beam instabilities in high energy accelerators*. Wiley, New York, NY, 1993.

[3] K. Y. Ng. *Physics of intensity dependent beam instabilities*. World Scientific, Hoboken, NJ, 2006.

[4] J. L. Laclare. Bunched beam coherent instabilities. (CERN Accelerator School), Sep 1985.

[5] T. Bohl, T. P. R. Linnecar, and E. N. Shaposhnikova. Measurements of the microwave instabilities in the SPS. Technical Report SL-MD-Note-164, CERN, Geneva, Jan 1995.

[6] T. Bohl, T. P. R. Linnecar, and E. Shaposhnikova. Impedance Reduction in the CERN SPS as seen from Longitudinal Beam Measurements. (CERN-SL-2002-023-HRF), May 2002.

[7] F. J. Sacherer. Methods for computing bunched-beam instabilities. Technical Report CERN-SI-BR-72-5, CERN, Geneva, Sep 1972.

[8] L.D. Landau. On the vibrations of the electronic plasma. *J.Phys.(USSR)*, 10:25–34, 1946.

[9] H. G. Hereward. *The elementary theory of Landau damping*. CERN, Geneva, 1965.

[10] T. Bohl, T. P. R. Linnecar, E. Shaposhnikova, and J. Tückmantel. Study of Different Operating Modes of the 4th RF Harmonic Landau Damping System in the CERN SPS. (CERN-SL-98-026-RF EPAC98), Jun 1998.

[11]

[12] A. Burov. Van Kampen modes for bunch longitudinal motion. Technical Report arXiv:1207.5826. FERMILAB-CONF-10-376-AD, Jul 2012. Comments: 5 pp. 46th ICFA Advanced Beam Dynamics Workshop on High-Intensity and High-Brightness Hadron Beams HB2010, Sep 27 - Oct 1 2010. Morschach, Switzerland.

[13] A. Burov. Dancing bunches as Van Kampen modes. Technical Report arXiv:1208.4338. FERMILAB-CONF-11-121-AD, Aug 2012. Comments: 4 pp. Particle Accelerator, 24th Conference (PAC'11) 2011. 28 Mar - 1 Apr 2011. New York, USA.

[14] T. P. R. Linnecar and E. N. Shaposhnikova. Analysis of the voltage programs for the Sp$\overline{\text{p}}$S double frequency RF system. Technical Report SL-Note-92-44-RFS, CERN, Geneva, Feb 1992.

[15] T. Linnecar. private communication.

[16] A. N. Lebedev. Coherent synchrotron oscillations in the presence of a space charge. *Atomnaya Energiya*, 25 (2):100–104, 1968.

[17] The esme code was developed at fermilab by james maclachlan and co-workers. http://www-ap.fnal.gov/ESME/. Accessed: 2014-01-21.

[18] B. W. Zotter and S. A. Kheifets. *Impedances and wakes in high-energy particle accelerators*. World Scientific, Singapore, 1998.

[19] R. Garoby. Bunch merging and splitting techniques in the injectors for high energy hadron colliders. (CERN-PS-98-048-RF, Proc. of HEACC'98), Oct 1998.

[20] E. Shaposhnikova. Cures for beam instabilities in the CERN SPS and their limitations. *39th ICFA Advanced Beam Dynamics Workshop on High Intensity High Bightness Hadron Beams HB2006*, May 2006.

[21] M. Benedikt, P. Collier, V. Mertens, J. Poole, and K. Schindl. *LHC Design Report Vol. III: The LHC Injector Chain*. Number CERN-2004-003-V-3. CERN, Geneva, Switzerland, 2004.

[22] CERN. *About CERN*. http://www.cern.ch/about.

[23] O. S. Brüning, P. Collier, P. Lebrun, S. Myers, R. Ostojic, J. Poole, and P. Proudlock. *LHC Design Report Vol. I: The LHC Main Ring*. Number CERN-2004-003-V-1. CERN, Geneva, 2004.

[24] ATLAS Collaboration. Observation of a new particle in the search for the Standard Model Higgs boson with the ATLAS detector at the LHC. *Physics Letters B*, 716:1–29, Sep 2012.

[25] CMS Collaboration. Observation of a new boson at a mass of 125 GeV with the CMS experiment at the LHC. *Physics Letters B*, 716:30–61, Sep 2012.

[26] R. Garoby. Multiple bunch-splitting in the PS: results and plans. Technical Report CERN-PS-2001-004-RF, CERN, Geneva, Feb 2001. Not published in the proceedings.

[27] H. Damerau. *Multi-bunch beam for LHC in the PS*. BE/OP Shutdown Courses, 2011.

[28] G. Dôme. The SPS acceleration system travelling wave drift-tube structure for the CERN SPS. (CERN-SPS-ARF-77-11):26 p, May 1977.

[29] E. Shaposhnikova. Longitudinal stability of the LHC beam in the SPS. Technical Report SL-Note-2001-031-HRF, CERN, Geneva, Aug 2001.

[30] H. Timko, T. Argyropoulos, T. Bohl, H. Damerau, J. F. Esteban Müller, S. Hancock, and E. Shaposhnikova. Longitudinal transfer of rotated bunches in the cern injectors. *Phys. Rev. ST Accel. Beams*, 16:051004, May 2013.

[31] D. Boussard. Beam loading. (CERN Accelerator School), Sep 1985.

[32] G. Papotti, T. Bohl, T. Linnecar, E. Shaposhnikova, and J. Tückmantel. Study of Controlled Longitudinal Emittance Blow-Up for High Intensity LHC Beams in the CERN SPS. (11th European Particle Accelerator Conference), Jun 2008.

[33] H. Bartosik, G. Arduini, and Y. Papaphilippou. Optics considerations for lowering transition energy in the SPS. (CERN-ATS-2011-088):3 p, Sep 2011.

[34] H. Bartosik. *Beam dynamics and optics studies for the LHC injectors upgrade*. PhD thesis, TU Vienna, Oct 2013. Presented 13 Nov 2013.

[35] E. Shaposhnikova. Lessons from SPS studies in 2010. *in Proceedings of the Chamonix 2011 LHC Performance Workshop*, 2011.

[36] H. Bartosik et al. Low gamma transition optics for the SPS: simulation and experimental results for high brightness beams. (HB2012), Sep 2012.

[37] E. N. Shaposhnikova, E. Ciapala, and E. Montesinos. Upgrade of the 200 MHZ RF System in the CERN SPS. (CERN-ATS-2011-042):3 p, Aug 2011.

[38] L. Rossi. LHC Upgrade Plans: Options and Strategy. (CERN-ATS-2011-257):6 p, Dec 2011.

[39] R. Garoby, S. Gilardoni, B. Goddard, K. Hanke, M. Meddahi, and M. Vretenar. Plans for the upgrade of the LHC injectors. (CERN-ATS-2011-185):3 p, Sep 2011.

[40] O. Bruning and F. Zimmermann. Parameter Space for the LHC High-Luminosity Upgrade. *Conf. Proc.*, C1205201(CERN-ATS-2012-070):MOPPC005. 3 p, May 2012.

[41] E. Shaposhnikova, T. Argyropoulos, T. Bohl, J. E. Müller, and H. Timko. Longitudinal instabilities in the SPS and beam dynamics issues with high harmonic RF systems. *52nd ICFA Advanced Beam Dynamics Workshop on High-Intensity and High-Brightness Hadron Beams HB2012*, Sep 2012.

[42] T. Argyropoulos, T. Bohl, H. Damerau, J. F. Esteban Müller, E. N. Shaposhnikova, and H. Timko. Identification of the SPS Impedance at 1.4 GHz. *Conf. Proc.*, C130512(CERN-ACC-2013-0202):TUPWA039. 3 p, May 2013.

[43] E. Shaposhnikova, T. Bohl, and T. P. R. Linnecar. Beam transfer functions and beam stabilisation in a double RF system. (CERN-AB-2005-026):4 p, Jun 2005.

[44] F. J. Sacherer. A longitudinal stability criterion for bunched beams. (CERN-MPS-INT-BR-73-3):5 p, Feb 1973.

[45] T. Argyropoulos, T. Bohl, T. P. R. Linnecar, E. Shaposhnikova, and J. Tückmantel. Controlled longitudinal emittance blow-up in double harmonic RF system at CERN SPS. *46th ICFA Advanced Beam Dynamics Workshop on High Intensity High Bightness Hadron Beams HB2010*, Sept.-Oct. 2010.

[46] *LIU-SPS Beam Dynamics Working Group*. http://paf-spsu.web.cern.ch/paf-spsu/.

[47] H. Goldstein, C. Poole, and J. Safko. *Classical Mechanics; 3rd ed.* Addison-Wesley, San Francisco, CA, 2002.

[48] S. Y. Lee. *Accelerator Physics; 2nd ed.* World Scientific, London, 2004.

[49] G. Dome. Theory of RF acceleration. (CERN Accelerator School), Sep 1985.

[50] A. Hofmann and S. Myers. Beam dynamics in a double RF system. (CERN-ISR-TH-RF-80-26), 1980.

[51] E. Shaposhnikova. Bunched beam transfer matrices in single and double rf systems. Technical Report CERN-SL-94-19. CERN-SL-94-19-RF, CERN, Geneva, Aug 1994.

[52] J.Y. Liu, D.D. Caussyn, M. Ellison, S.Y. Lee, D. Li, A. Riabko, and L. Wang. Analytic solution of particle motion in a double RF system. *Part.Accel.*, 49:221–251, 1995.

[53] J. Varela Campelo. *LIU-SPS Beam Dynamics Working Group.* http://paf-spsu.web.cern.ch/paf-spsu/, July 2014.

[54] A. A. Vlasov. On the Kinetic Theory of an Assembly of Particles with Collective Interaction. *J.Phys.(USSR)*, 1:25–45, 1945.

[55] H. Risken. *The Fokker-Planck Equation, 2nd ed.* Springer-Verlag, N.Y., 1989.

[56] V. K. Neil and A. M. Sessler. Longitudinal Resistive Instabilities of Intense Coasting Beams in Particle Accelerators. *Rev. Sci. Instrum.*, 36:429, 1965.

[57] A. Hofmann. Landau damping. (CERN Accelerator School: Intermediate Course on Accelerator Physics,), Sep 2003.

[58] S. V. Ivanov V. I. Balbekov. Methods for suppressing the longitudinal instability of a bunched beam with the help of landau damping. *Atomnaya Energiya*, 62 (2):117–125, 1987.

[59] F. Pedersen A. Blas, S. Koscielniak. Explanation of Sextupole Instability in CERN PS Booster. *Proc. EPAC98*, pages 969–971, Jun 1998.

[60] T. Bohl E. Shaposhnikova and T. Linnecar. Beam transfer functions and beam stabilisation in a double RF system. *Proc. PAC'05*, page 2300, May 2005.

[61] K. Oide and K. Yokoya. Longitudinal single bunch instability in electron storage rings. *Phys.Rev.Lett.*, 1990.

[62] N. G. van Kampen. On the theory of stationary waves in plasma. *Physica*, 21:949–963, 1955.

[63] N. G. van Kampen. The dispersion equation for plasma waves. *Physica*, 23:641–650, 1957.

[64] T. Argyropoulos M. Migliorati, A. Burov. to be published.

[65] G. Papotti, T. Bohl, T. Linnecar, E. Shaposhnikova, and J. Tückmantel. Longitudinal parameters of the LHC beam in the SPS: 25 ns/50 ns/75 ns bunch spacing. (CERN-BE-Note-2009-016), Mar 2009.

[66] T. Argyropoulos, C. Bhat, T. Bohl, H. Damerau, T. Linnecar, G. Papotti, E. Shaposhnikova, and J. Tückmantel. Studies of single bunch instability in a double RF harmonic system of the SPS at 26 GeV/c. (CERN-BE-Note-2010-013), Apr 2010.

[67] T. Argyropoulos, T. Bohl, G. Papotti, and E. Shaposhnikova. Measurements of Single Bunch Instabilities in the SPS at 26 GeV/c for single and double RF system. (CERN-ATS-Note-2011-090 MD), Oct 2011.

[68] T. Bohl. Bunch length measurements with the SPS AEW.31731 wall current monitor. Technical Report CERN-AB-Note-2007-032, CERN, Geneva, Jun 2007.

[69] T. P. R. Linnecar and E. N. Shaposhnikova. Resonant impedances in the SPS. Technical Report SL-Note-96-49-RF, CERN, Geneva, Aug 1996.

[70] S. Hancock. A simple algorithm for longitudinal phase space tomography. Technical Report CERN-PS-RF-NOTE-97-06, CERN, Geneva, May 1997.

[71] J. Tückmantel. Digital Generation of Noise-Signals with Arbitrary Constant or Time-Varying Spectra (A noise generation software package and its application). Technical Report LHC-PROJECT-Report-1055. CERN-LHC-PROJECT-Report-1055, CERN, Geneva, 2008.

[72] C. Zannini and G. Rumolo. Em simulations in beam coupling impedance studies: some examples of application. Aug 2012.

[73] P. B. Wilson. Transient beam loading in electron-positron storage rings; rev. version. Technical Report PEP-276, 1978.

[74] P. Baudrenghien. Control of strong beam loading: Results with beam. In *11th Workshop of the LHC*, Chamonix, France, 2001.

[75] D. Boussard and G. A. Lambert. Reduction of the apparent impedance of wide band accelerating cavities by rf feedback. *IEEE Trans. Nucl. Sci.*, 30(CERN-SPS-83-18-ARF):2239–2241. 4 p, Mar 1983.

[76] P. Baudrenghien, T. Bohl, and P. Hagmann. *LIU-SPS LLRF upgrade.* LIU Technical Design Report, CERN, to be published.

[77] G. Hagmann and P. Baudrenghien. *LLRF and commissioning.* https://indico.cern.ch/event/277739/, LIU-SPS Coordination meeting, CERN, Dec 12th 2013.